

INVESTIGATION OF A SPATIAL OPTICAL PULSE COLLECTION SYSTEM IN
THE ALL-OPTICAL ANALOG-TO-DIGITAL CONVERTER

A Dissertation
Presented to
The Faculty of the Graduate School
University of Missouri-Columbia

In Partial Fulfillment
of the Requirements for the Degree

Doctor of Philosophy

by
WEN-REN YANG

Dr. William C. Nunnally, Dissertation Supervisor

DECEMBER 2005

The undersigned, appointed by the Dean of the Graduate School,
have examined the dissertation entitled.

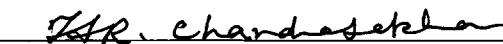
INVESTIGATION OF A SPATIAL OPTICAL PULSE COLLECTION
SYSTEM IN THE ALL-OPTICAL ANALOG-TO-DIGITAL
CONVERTER

Presented by Wen-Ren Yang

A candidate for the degree of Doctor of Philosophy, Electrical Engineering

And hereby certify that in their opinion it is worthy of acceptance.


_____ Dr. William C. Nunnally


_____ Dr. H.R. Chandrasekhar


_____ Dr. John Gahl


_____ Dr. Robert M. O'Connell


_____ Dr. T. Greg Engel

ACKNOWLEDGEMENTS

I would like to express my appreciation to Dr. Nunnally for his support through all the efforts toward the Ph.D. “inch by inch”; the invisible effects for life and research methodologies that are not delivered by the lecture or written materials from the advisor.

I would like to also thank Drs. O’Connell, Gahl, H.R. Chandrasekhar, and Engel for serving on my committees; especially Dr. O’Connell for the first stage in the graduate career, Dr. Gahl for the initial Electromagnetic adventure, and Dr. Chandrasekhar for the Optical basics.

Wen-Ren Yang also appreciates the support from the family at Taiwan, for everything towards this degree in his life.

**INVESTIGATION OF A SPATIAL OPTICAL PULSE COLLECTION SYSTEM
IN THE ALL-OPTICAL ANALOG-TO-DIGITAL CONVERTER**

Wen-Ren Yang

Dr. William C. Nunnally, Dissertation Supervisor

ABSTRACT

In this research, I conducted a systematic integration of specific calculations for the analysis of the spatial filter that is a critical component of an all-optical analog-to-digital converter. The designed all-optical analog-to-digital converter has special relevance for high-resolution \times bandwidth applications such as radar image processing. The design of the spatial filter array is based on the silicon-on-insulator process, a design that fulfills requirements of both lower power consumption and smaller integrated circuit chip size.

For the developed calculation model, Babinet's principle is used in order to decompose a complicated structure into different simple components. The decomposed structure is analyzed by modifying the existing diffraction calculation methods.

The method of calculating the transmission ratio of the propagating electric field compared to the finite-different-time-domain method is a new approach. The systematic integration is also adaptive to changes in the spatial filter's components. Structural changes do not require changes to the entire calculation model. In addition, the concept applies to a modular design for the hardware implementation.

TABLE OF CONTENTS

ACKONWLEGEMENTS.....	ii
ABSTRACT.....	iii
LIST OF FIGURES.....	vii
LIST OF TABLES.....	xiv
Chapter 1: Introduction	
1.1 Analog-to-Digital Converter and Applications.....	1
1.2 Analog-to-Digital Conversion.....	9
1.3 All-Optical Analog-to-Digital Converter.....	20
Chapter 2: Analog-to-Digital Converter Limitations	
2.1 Analog-to-Digital Converter Architectures.....	24
2.2 Analog-to-Digital Converter Measures.....	29
2.3 Comparisons and Trade-Offs of Analog-to-Digital Converter Architectures.....	34
2.4 Optical ADC.....	36
Chapter 3: Basics of Research Methods	
3.1 Wave Optics.....	39
3.2 Integrated Optical Waveguide.....	45
3.3 Finite Difference Time Domain Method.....	54
Chapter 4: Research Objectives	
4.1 Components of the Spatial Optical Pulse Collection System.....	59

4.2	Limitations.....	66
4.3	Proposed Research.....	72
Chapter 5: Research Results		
5.1	Fundamentals of the Modeling Methods for the Spatial Filter.....	84
5.1.1	Fresnel-Kirchhoff Diffraction.....	84
5.1.2	Edge Diffraction.....	88
5.1.3	Cylindrical Wave Equation and Wedge Diffraction.....	89
5.1.4	Fresnel Equations.....	94
5.1.5	Babinet's Principle.....	95
5.2	Decompositions of the Spatial Filter and Systematic Integration of the Calculations into Transfer Functions.....	97
5.3	Simulations and Calculations	
5.3.1	Basic Setup of the Electro-Optical Deflector and the Spatial Filter Array.....	103
5.3.2	Geometrical Specifications of the Spatial Filter.....	107
5.3.3	Basic Setup of the FDTD Calculations.....	114
5.4	Comparisons, Conclusions, and Future Works.....	118

APPENDIX

A. Diffraction Coefficients Calculations of Electro-Optical Deflector and Surface Plasmons.....125

B. Diffraction Coefficients Calculations of Tilted Aperture.....133

REFERENCE LIST.....137

VITA.....143

LIST OF FIGURES

Figure 1: Distorted signal being detected and regenerated.....	1
Figure 2: Touch-tone phone wave.....	2
Figure 3: $\cos(\omega t), f = 50Hz$	3
Figure 4: $x(n) = \cos(\frac{\pi}{4}) \cdot n, f_d = \frac{1}{8}$	4
Figure 5: $\cos(\frac{\pi}{2}) \cdot n, f_d = \frac{1}{4}$	5
Figure 6: Block Diagram of the 10-Bit Digital Temperature Sensor with ADC.....	6
Figure 7: GPS receiver.....	7
Figure 8: Block diagram of an HDSL transceiver.....	8
Figure 9: 14 bit 250 K samples/sec operated at 2.5 V ADC.....	8
Figure 10: Analog-to-digital conversion steps.....	9
Figure 11: Sampling of the analog signal.....	9
Figure 12: Digital signal sampled by the switching box.....	10
Figure 13: Analog signal in time and frequency domain.....	11
Figure 14: Periodic sampling impulse function.....	11
Figure 15: Sampled signal in the time domain.....	12
Figure 16: Periodic impulse train in the frequency domain.....	12
Figure 17: Sampled data in the frequency domain.....	13
Figure 18: Aliasing in the frequency domain.....	13
Figure 19: Short duration periodic sampling waveform.....	14
Figure 20: Sampled waveform with finite sampling interval.....	14
Figure 21: Fourier series representation of periodic pulse train.....	15
Figure 22: Sampled data in the frequency domain.....	16

Figure 23: Digitized data in the quantization mappings.....	17
Figure 24: All-optical ADC flow diagram.....	18
Figure 25: All-optical ADC data diagram.....	19
Figure 26: All-Optical ADC structure.....	20
Figure 27: Sigma-delta ADC.....	25
Figure 28: 15-bit pipelined ADC.....	26
Figure 29: Flash ADC.....	27
Figure 30: 4-channel time-interleaved ADC.....	28
Figure 31: Signal-to-noise ratio (SNR) illustration.....	29
Figure 32: Spurious Free Dynamic Range (SFDR).....	30
Figure 33: Product of the effective quantization number and sampling rate.....	31
Figure 34: Figure of merit.....	32
Figure 35: Aperture jitter.....	33
Figure 36: Trade-offs of ADC architectures.....	35
Figure 37: Optically assisted ADC.....	36
Figure 38: All-optical ADC.....	37
Figure 39: Optically assisted ADC.....	38
Figure 40: 1-Dimensional wave.....	39
Figure 41: 3-Dimensional linearly polarized wave.....	40
Figure 42: Plane wave transmission and reflection.....	41
Figure 43: Incident angle is larger than the critical angle.....	42
Figure 44: Critical angle.....	43
Figure 45: TE mode.....	43

Figure 46: TM mode.....	44
Figure 47: 1-dimensional waveguide.....	45
Figure 48: Matlab calculations and plots of dispersion curves of Equation 33.....	47
Figure 49: Slab waveguide.....	48
Figure 50: Matlab calculations and plots of TE even mode dispersion curves.....	50
Figure 51: Matlab calculations and plot of TE even mode field distribution in the silica material.....	51
Figure 52: Matlab calculations and plots of TE even mode electric field distributions in the silicon material.....	51
Figure 53: Comparison of fabricated SOI waveguide and other silicon applications.....	53
Figure 54: 3-dimensional FDTD cell.....	54
Figure 55: 2-dimensional FDTD cells in the TE and the TM modes.....	56
Figure 56: Single spatial filter.....	59
Figure 57: Tapered and square spatial filter.....	60
Figure 58: Spatial filter array.....	61
Figure 59: Fabricated near field aperture array.....	62
Figure 60: Tapered waveguide.....	63
Figure 61: Tapered waveguide in application of wavelength multiplexing chip.....	63
Figure 62: Optical waveguide by SOI method.....	64
Figure 63: Silicon waveguide and output coupling exam.....	65
Figure 64: Tapered spatial filter.....	66
Figure 65: FDTD simulation example of tapered spatial filter.....	67
Figure 66: Spatial filter array.....	68

Figure 67: FDTD simulation example of 5-degree deflection angle.....	69
Figure 68: Transmission ratio of tapered spatial filter array by various deflection angles.....	69
Figure 69: Specifications for tapered optical waveguide.....	70
Figure 70: Power ratio (P(B)/P(A)) of different scaling factors.....	71
Figure 71: FDTD simulation example of tapered waveguide.....	71
Figure 72: Illustration of the proposed research.....	72
Figure 73: Diffracting aperture.....	74
Figure 74: Cylindrical waveguide.....	76
Figure 75: Line source being located away from the origin.....	77
Figure 76: 3-D view of wedge scattering.....	79
Figure 77: 2-D view of the wedge.....	80
Figure 78: Special example of Babinet's principle.....	83
Figure 79: Dimensional specifications of the Fresnel-Kirchhoff integral.....	84
Figure 80: Matlab calculations and plot of Fresnel integral.....	86
Figure 81: Matlab calculations and plot of $ D $ versus θ . $r_1 = 5\mu m$, $r_2 = 3\mu m$, $\lambda = 0.633\mu m$, $x_1 = x_2 = 0.5\mu m$	87
Figure 82: Matlab calculations and plot of $ D $ versus v	88
Figure 83: Matlab calculations and plot of $ D $ versus θ . $r_1 = 5\mu m$, $r_2 = 3\mu m$, $\lambda = 0.633\mu m$, $x_1 = 0.5\mu m$	89
Figure 84: Matlab calculations and plot of Bessel and Hankel functions.....	91
Figure 85: Matlab calculations and plot of $G(\rho' = 1000\lambda)$, Equation 94.....	92

Figure 86: Radar plot of Figure 85.....	92
Figure 87: Matlab calculations and plot of $G(\rho' = 10\lambda)$, Equation 93.....	93
Figure 88: Radar plot of Figure 87.....	93
Figure 89: E_t : transmitted electric field, E_r : reflected electric field.....	94
Figure 90: Matlab calculations and plot of TE mode.....	94
Figure 91: Matlab calculations and plot of TM mode.....	95
Figure 92: Illustration of both the spatial filter and the observation point.....	97
Figure 93: First decomposition of the spatial filter.....	98
Figure 94: Top and cross-section views of the spatial filter.....	99
Figure 95: Second decomposition of the spatial filter.....	100
Figure 96: Spatial phase definition of the optical source.....	101
Figure 97: Systematic integration of the transmission calculation.....	102
Figure 98: Electro-optical deflector and spatial optical pulse collection array.....	103
Figure 99: Electro-optical deflector.....	105
Figure 100: Spatial filter array specifications.....	106
Figure 101: Circular scanning contour of θ	107
Figure 102: Expected linear scanning contour of θ	108
Figure 103: Complete specifications of spatial filter calculations.....	109
Figure 104: Geometrical specifications for the center wave calculation.....	109
Figure 105: Matlab calculations and plot of $\theta = 0 \sim 3^\circ$ at observation point 1, Equation 88.....	110
Figure 106: Matlab calculations and plot of $\theta = 0 \sim 3^\circ$ at observation point 1, Equation 90.....	110

Figure 107: Geometrical specifications for the upper wedge calculation.....	111
Figure 108: Geometrical specifications for the lower wedge calculation.....	112
Figure 109: Matlab calculations and plot of $\theta = 0 \sim 3^\circ$ at observation point 1, Equation 93.....	112
Figure 110: Matlab calculations and plot of $\theta = 0 \sim 3^\circ$ at observation point 1, the sum of Equations 93 and 99.....	113
Figure 111: E_y of unit amplitude for the FDTD calculation.....	114
Figure 112: FDTD layout and transmission ratio in λ domain of upper spatial filter.....	115
Figure 113: FDTD layout and transmission ratio in λ domain of upper and lower filters.....	116
Figure 114: Frequency response of the input wave for the FDTD calculation.....	117
Figure 115: Matlab and FDTD calculations for Equation 101 and Fig. 97, observation point 1.....	118
Figure 116: Matlab and FDTD calculations for Equation 101 and Fig. 97, observation point 1.....	119
Figure 117: Matlab and FDTD calculations for Equation 101 and Fig. 97, observation point 2.....	120
Figure 118: Matlab calculation of the optical waveguide transmission, TE mode of Equation 77.....	121
Figure A1: Kirchhoff-Fresnel Diffraction.....	125
Figure A2: Illustration of Kirchhoff-Fresnel diffraction to be applied to the deflector...126	
Figure A3: Riemann sum method to calculate the integral of $f(x)$	129

Figure A4: Calculation results of the edited Matlab code for the case of $n_1 = 1$, $n_2 = 1$	130
Figure A5: Diffraction coefficient of 18~22 degrees for the deflector.....	131
Figure A6: Surface Plasmons design and FDTD simulation of $\theta = 0^\circ, 3^\circ$. $W = 400nm, h = 80nm, t = 20nm$	132
Figure A7: Kirchhoff-Fresnel diffraction of tapered structure.....	133
Figure A8: Calculations of Equation A13.....	136

LIST OF TABLES

Table 1: Comparisons of ADCs.....	34
-----------------------------------	----

Chapter 1. Introduction

1.1 Analog-to-digital converter (ADC) and applications

The digital signal has been used for a long time, regardless of whether wired computing devices or wireless systems are used; furthermore, the digital signal has almost overwhelmingly replaced the analog signal in the high-speed data transmission or signal processing. Figure 1 simply illustrates the digital signal distortion and recovery in three stages [1]. Here, (A) stands for the initial digital signal that exhibits a perfect rectangular waveform, (B) stands for the signal that suffers distortion in the transmission channel (in the circuit or different channels), and (C) is a digital signal that has been detected and regenerated. Complete data transmission is not shown here. Figure 1 describes the “digital advantage,” that is, “0” or “1”; however, “everything” is possible in analog format.

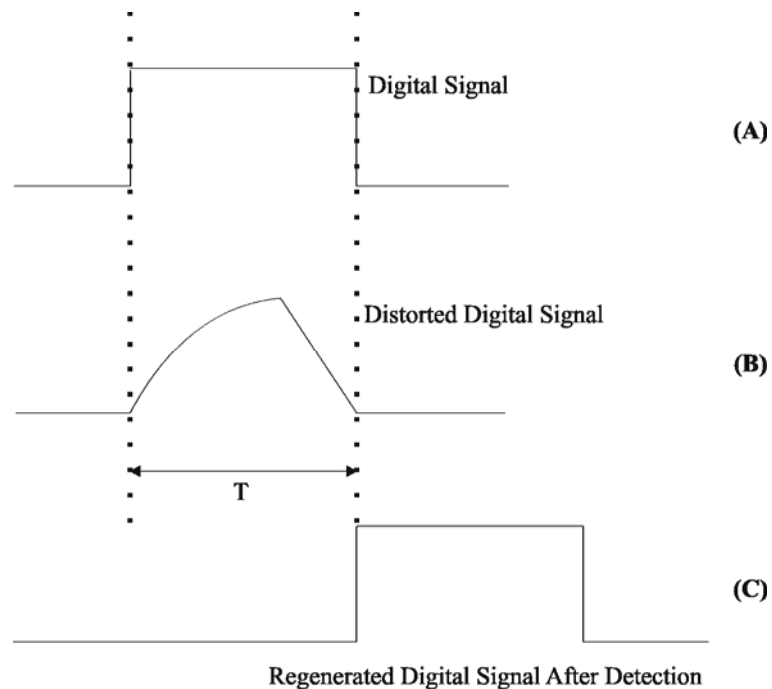


Figure 1. Distorted signal being detected and regenerated. T : Signal time width.

Figure 2 shows, as an example, the analog signal of a touch-tone phone wave. The regeneration of the random analog signal will be more complicated to be regenerated than that of the digital signal.

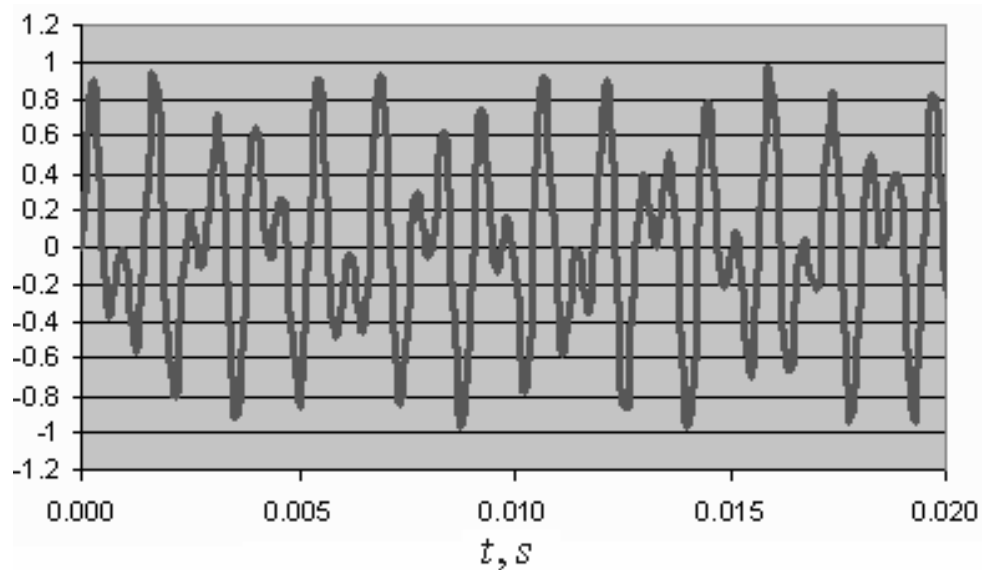


Figure 2. Touch-tone phone wave. [2]

Different binary codes or detection schemes are introduced in the receiver-end to execute the reconfirmation. These techniques reduce the requirements of the transmission channel is performing the reconfirmation. The “0” and “1” of the binary format makes it easier for the receiver to “guess.” We list the following familiar schemes [1]:

Binary Codes:

1. Nonreturn-to-zero (NRZ)
2. Return-to-zero (RZ)
3. Phase encoded
4. Multilevel binary

Binary Detections:

1. Coherent Detection (maximum likelihood detection)
2. Noncoherent Detection (envelope detection)

The basic operation of an Analog-to-Digital Converter (ADC) will be demonstrated in the following example. The waveform shown in Fig. 3 is an analog cosine function defined as [3]

$$x(t) = \cos(\omega t + \theta), -\infty < t < \infty, \omega = 2\pi f \quad (1)$$

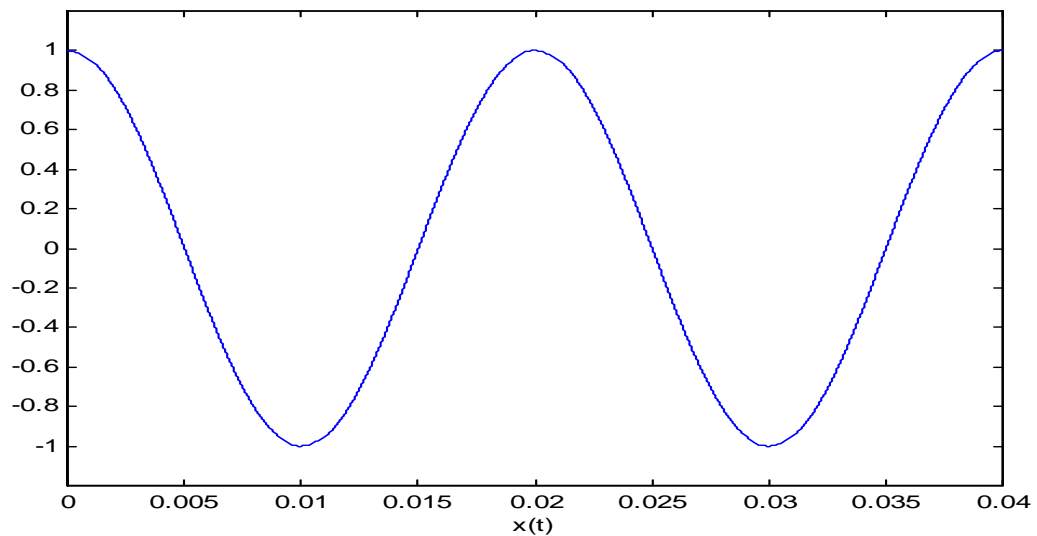


Figure 3. $\cos(\omega t), f = 50\text{Hz}$

Figure 4 is the signal of Fig. 3 processed by an ADC with a 400 Hz sampling frequency and defined as

$$x(n) = \cos(2\pi f_d n + \theta), -\infty < n < \infty, f_d = \frac{f}{F_s} \quad (2)$$

F_s : sampling frequency, $-\frac{1}{2} \leq f_d \leq \frac{1}{2}$

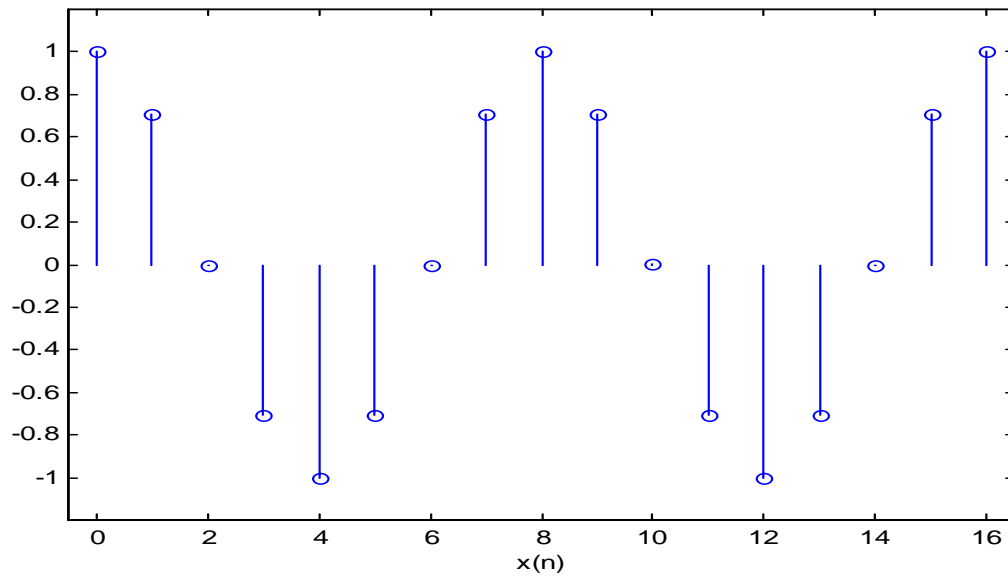


Figure 4. $x(n) = \cos(\frac{\pi}{4}) \cdot n, f_d = \frac{1}{8}$

As illustrated in Fig. 4, $f_d = \frac{1}{8}$; the waveform has 8 discrete points per complete cycle.

One more example of the analog-to-digital conversion that serves as the basic calculation of the sampling frequency.

Assume the analog signal in Fig. 3 is

$$x(t) = \cos 100\pi t = \cos \omega t, \omega = 2\pi f, f = 50\text{Hz}$$

and a sampling frequency of $F_s = 200\text{Hz}$ is used by ADC. The sampling criterion will

be discussed later. The sampled signal is

$$x(n) = \cos(2\pi \cdot \frac{f}{F_s})n = \cos \frac{100\pi}{200} n = \cos \frac{\pi}{2} n$$

The result plotted in Fig. 5, is the general expression of Equation 2 where the waveform has 4 samples ($f_d = \frac{1}{4}$) for a complete cycle.

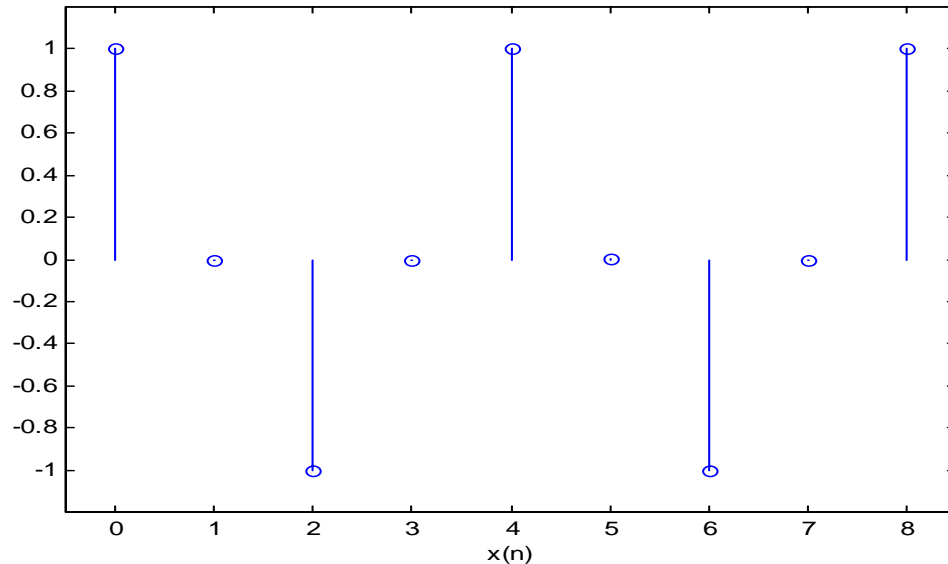


Figure 5. $\cos(\frac{\pi}{2}) \cdot n, f_d = \frac{1}{4}$

A comparison of Figs 4 and 5 indicates the higher number of sampling points redraw the analog signal with better resolution. Thus the number of samples represents resolutions in this introduction. Therefore, a higher sampling frequency is definitely required, and a higher sampling frequency results in more samples. In the next chapter, analog-to-digital conversion will be discussed in the frequency domain in order to present the essential sampling criteria.

The followings are real-life examples to show how to make use of the data transformed by ADC. In these examples, we find that existing manufacturing techniques can be used to integrate the system with ADC in a small-area chip sets.

The system structure of Fig. 6 is an ADC interface for the air-conditioning control. As illustrated in Fig. 6, the ADC delivers the digital signal to the processor. The processor performs special operation based on the given information, for example, the change in the temperature. The signal processor is designed so that the control process does not need a complicated analog signal such as the one in Fig. 2. The digitized example, illustrated in Fig. 4, can accomplish the same task. Therefore, the ADC provides the interface for the information exchange between processor and detector.

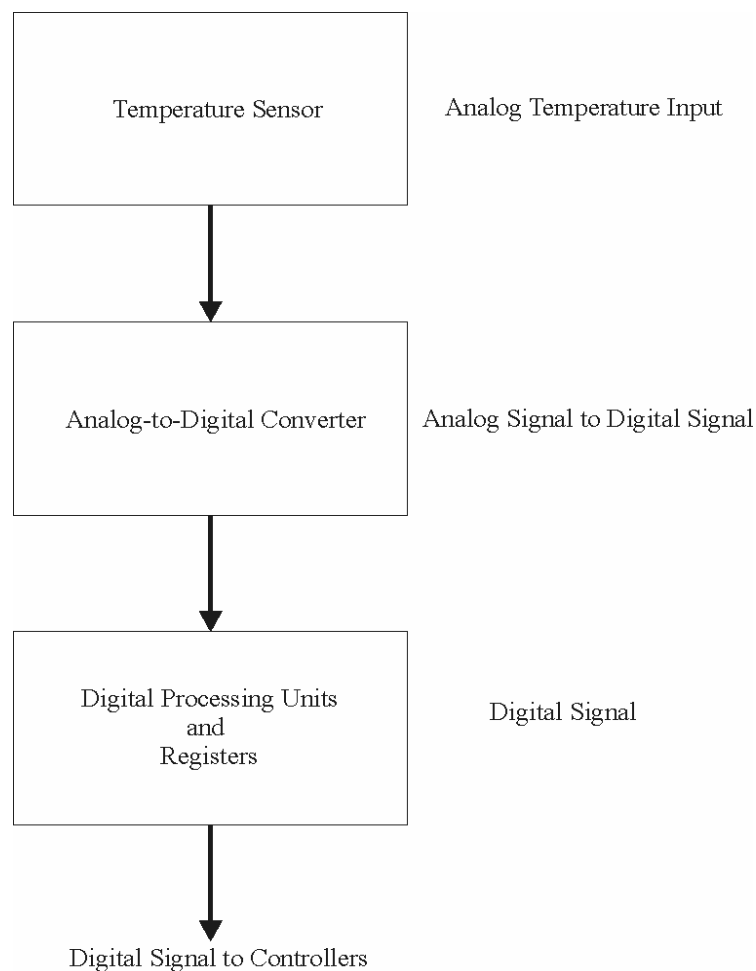


Figure 6. Block Diagram of the 10-Bit Digital Temperature Sensor with ADC [4]

A second example, shown in Fig. 7, the Global Positioning System (GPS) receiver incorporates mixed signal units [5] including radio, intermediate frequency, and baseband frequency subsystems. All these subsystems can construct a data transfer device used in different types of applications such as a Personal Digital Assistant (PDA) and a cellular phone. All systems convert analog signals into digitized signals for processing.

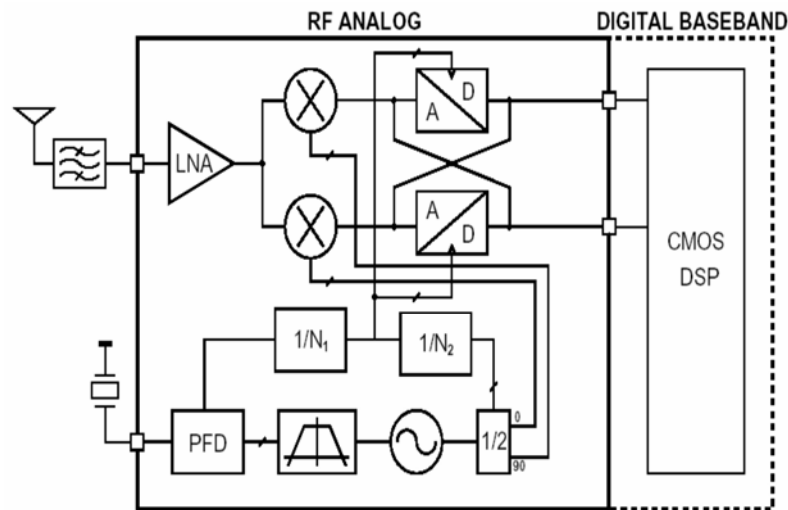


Figure 7. GPS receiver [5]

A third example, illustrated in Fig. 8 describes the data format transfer through the architecture of a High-speed Digital Subscriber Line (HDSL) transmission [6]. The data is converted in the analog-to-digital conversion through the telephone line, that is, through information transformation. For examples, the human voice has to be digitized to be modulated and sent to the wireless channel in the cellular phone.

In these given examples, the advantages of digital components--light-weight, smaller size, and security--over analog implementation are illustrated. These advantages apply to other important special-purpose applications such as security or military affairs.

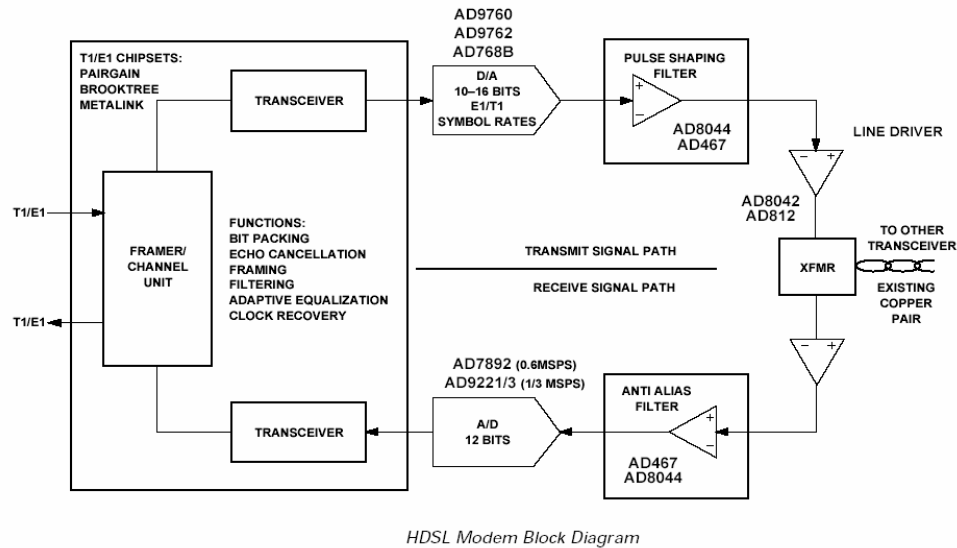


Figure 8. Block diagram of an HDSL transceiver [6]

The second advantage is the device size of the digital processing units. The last digital application to be introduced in this section, shown in Fig. 9, is ADC schematics from an integrated circuit manufacturer [7]. The basic ADC structure is actually based on the capacitive switching and comparator circuit, and is accompanied by a control unit. The size of the ADC chip is $3 \times 3 \text{ mm}^2$.

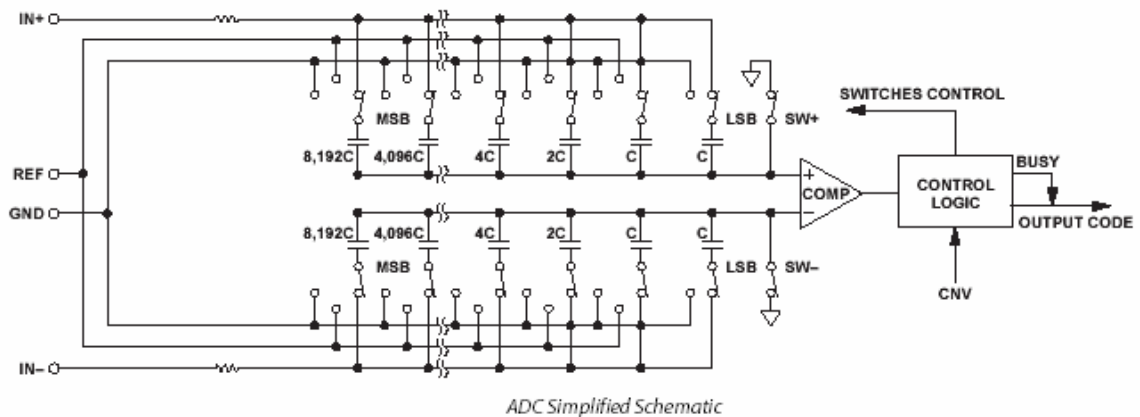


Figure 9. 14 bit 250 K samples/sec operated at 2.5 V ADC [7]

1.2 Analog-to-digital conversion

The analog-to-digital conversion process, illustrated in Fig. 10, is defined as three steps [3]:

1. Sampling
2. Quantization
3. Coding

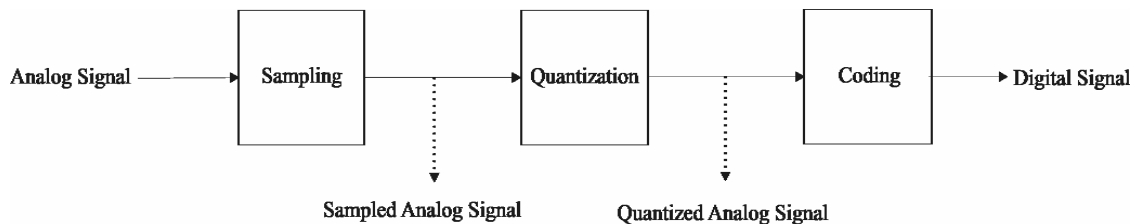


Figure 10. Analog-to-digital conversion steps

The sampling basics [1], illustrated in Fig. 11, are accomplished with a switch box that is sampling the analog signal which represents the sampling function.

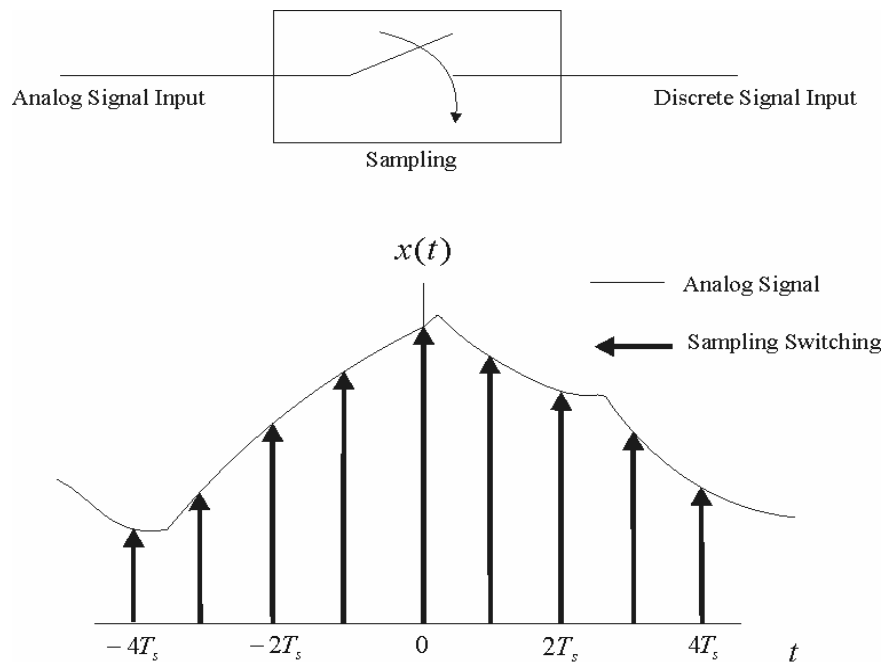


Figure 11. Sampling of the analog signal

The switching rate (sampling rate, period), defined as T_s , is the rate at which the switch is opened and closed.

In the second part of the Fig. 11, the dark lines represent the analog signal amplitude at the moment at which the switch is closed. The switching is assumed to be a perfect one and zero interval (one single perfect point) of the impulse; therefore, there are no transient phenomena in this case. The sampling interval is defined as the time the switch remains closed.

Figure 12 illustrates the sampled data, defined as “digital signal data” instead of “discrete data”. Discrete data means just one single point without the useful information related to sampling rate and period.

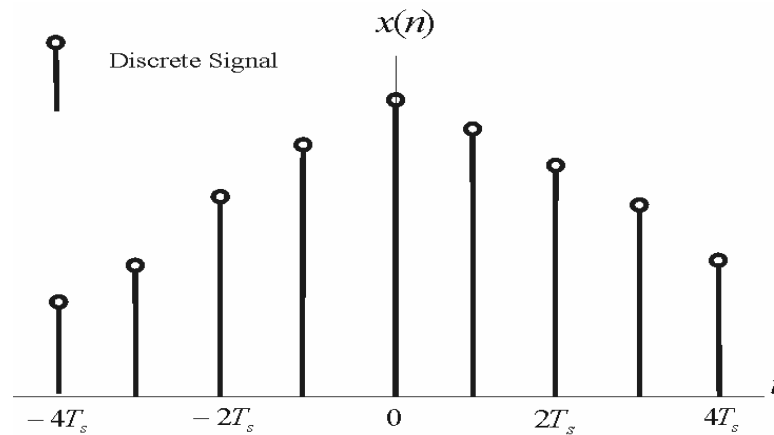


Figure 12. Digital signal sampled by the switching box

Next, we will demonstrate the analog-to-digital conversions by drawing on the basic impulse sampling technique and the one used in the all-optical ADC. Assume the analog signal to be converted is shown in Fig. 13 and that the frequency is in the range of $-f_m \sim f_m$.

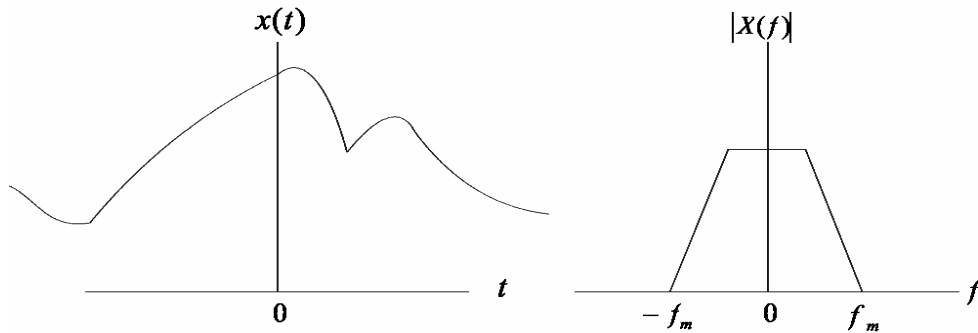


Figure 13. Analog signal in time and frequency domain

The periodic impulse sampling, illustrated in Fig. 14 is also called ideal sampling and is defined as

$$x_\delta(t) = \sum_{n=-\infty}^{\infty} \delta(t - nT_s) \quad (3)$$

x_δ : impulse function, T_s : sampling period

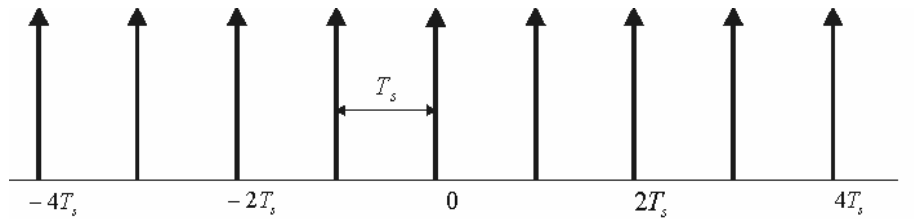


Figure 14. Periodic sampling impulse function

In Fig. 15 the analog signal is sampled by the periodic impulse and is simply multiplication in the time domain or

$$x_s(t) = x(t)x_\delta(t) = \sum_{n=-\infty}^{\infty} x(t)\delta(t - nT_s) = \sum_{n=-\infty}^{\infty} x(nT_s)\delta(t - nT_s) \quad (4)$$

x_s : sampled data

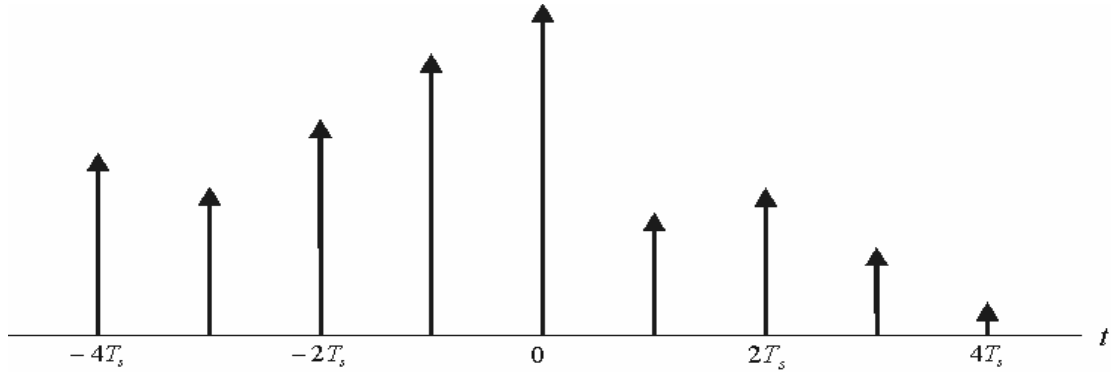


Figure 15. Sampled signal in the time domain

Before considering perfect sampling, we need to observe the sampling and the digitized message in the frequency domain. The impulse function, illustrated in Fig. 16, and the result by the Fourier transform is still the a periodic impulse train or

$$X_{\delta}(f) = \frac{1}{T_s} \sum_{n=-\infty}^{\infty} \delta(f - nf_s) \quad (5)$$

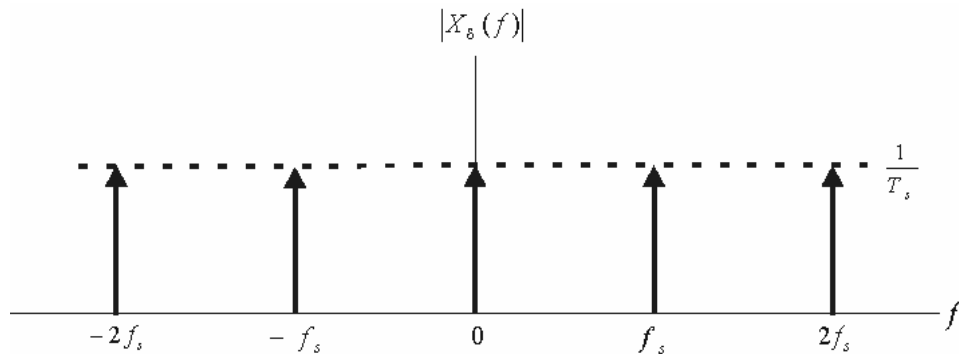


Figure 16. Periodic impulse train in the frequency domain

The multiplication in the time domain now becomes a convolution:

$$\begin{aligned} X_s(f) &= X(f) * X_{\delta}(f) = X(f) * \left[\frac{1}{T_s} \sum_{n=-\infty}^{\infty} \delta(f - nf_s) \right] = \frac{1}{T_s} \sum_{n=-\infty}^{\infty} X(f - nf_s) \\ \therefore X(f) * \delta(f - nf_s) &= X(f - nf_s) \quad (6) \end{aligned}$$

The results in the frequency domain signify a “replication” of the original message in the f_s interval. Therefore, the frequency distribution of the sampled information is illustrated in Fig. 17, which indicates an important requirement of the sampling technique, the Nyquist criterion.

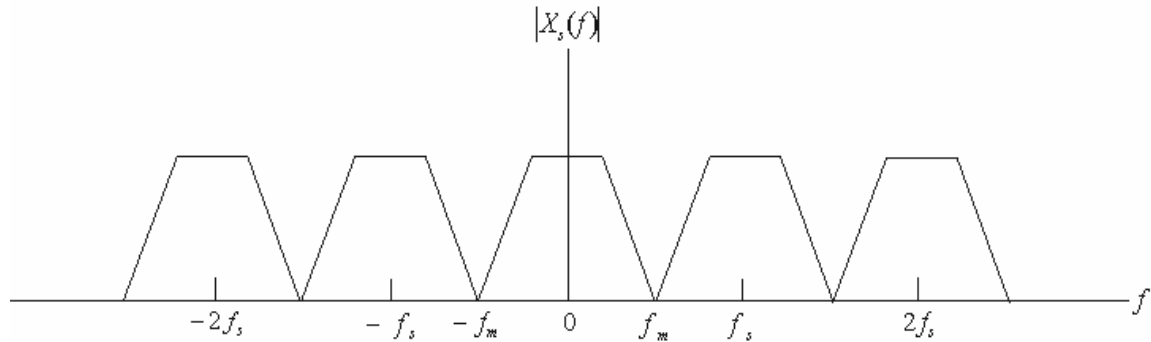


Figure 17. Sampled data in the frequency domain

In Fig. 17, the sampling frequency $f_s = \frac{1}{T_s}$ needs to be at least twice as large as the analog frequency being sampled f_m , or the frequency replica will overlap and cause the aliasing problem, as shown in Fig. 18.

$$f_s \geq 2 \cdot f_m \quad (7)$$

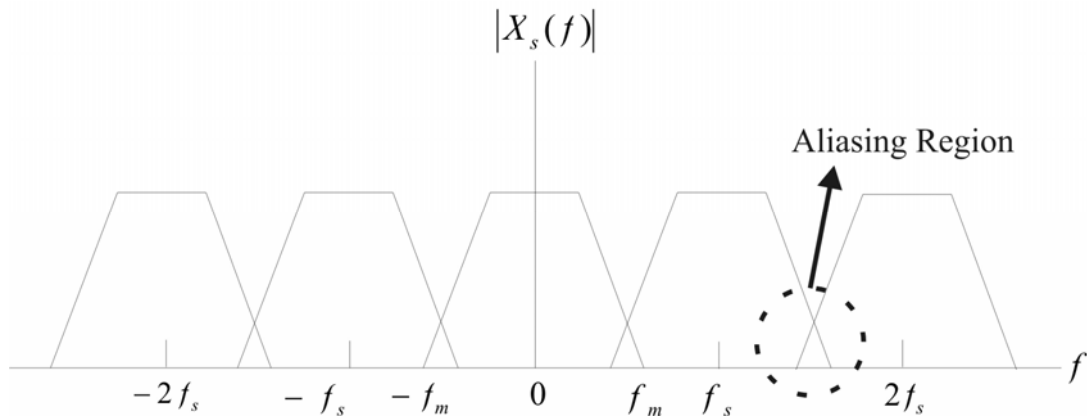


Figure 18. Aliasing in the frequency domain

The sampling impulse illustrated in Fig. 14 represents the perfect sampling in Fig. 11. However, there is always a finite width of the sampling signal. The same sampling analysis procedure described in the perfect sampling will be used to explain the imperfect sampling. Figure 19 illustrates the imperfect periodic sampling waveform of the finite width in time domain.

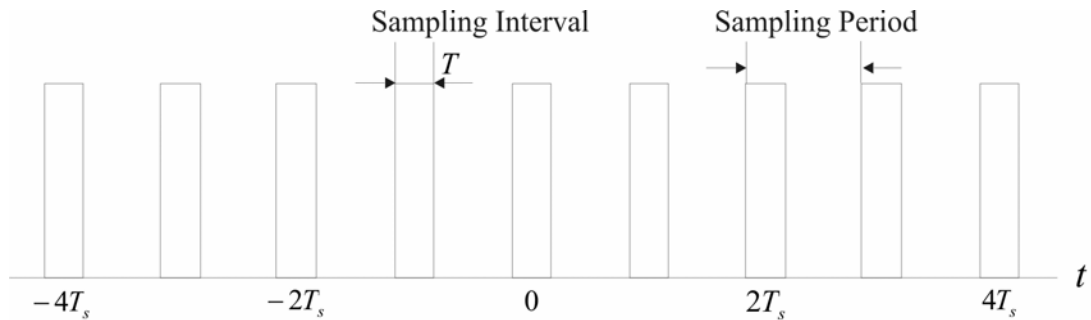


Figure 19. Short duration periodic sampling waveform

The basic assumption is that the Nyquist criterion is fulfilled ($\frac{1}{T_s} = f_s \geq 2 \cdot f_m$); the time domain multiplication is shown in Fig. 20.

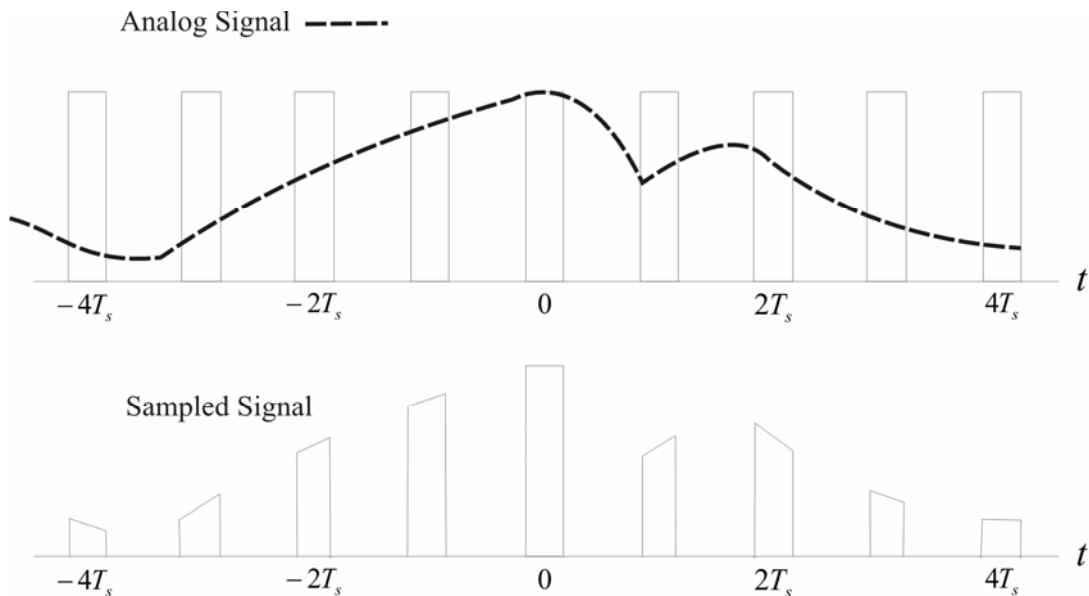


Figure 20. Sampled waveform with finite sampling interval

However, the sampling signal is not the perfect impulse, as shown in the previous example. In order to address the short duration sampling pulse, non-impulse sampling is represented in the frequency domain by the Fourier series as

$$x_p(t) = \sum_{n=-\infty}^{\infty} c_n e^{j2\pi n f_s t}, \quad c_n = (1/T_s) \text{sinc}(nT/T_s), \quad n = 0, 1, 2, \dots \quad (8)$$

$$x_p : \text{periodic pulse train}, \quad c_n : \text{Fourier series}, \quad \text{sinc}(y) = \frac{\sin \pi y}{\pi y}$$

The Fourier series power spectrum as a function of frequency in the frequency is plotted in Fig. 21.

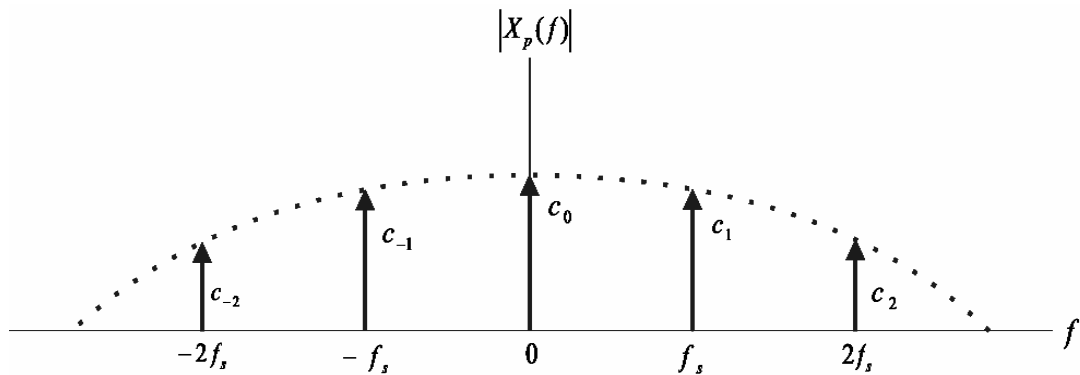


Figure 21. Fourier series representation of periodic pulse train

Notice that the impulse train in the frequency domain of Fig. 21 is no longer flat-top, and finite sampling period which also affects the frequency domain replica illustrated in Fig. 22.

$$X_s(f) = F \left\{ x(t) \sum_{n=-\infty}^{\infty} c_n e^{j2\pi n f_s t} \right\} = \sum_{n=-\infty}^{\infty} c_n F \left\{ x(t) e^{j2\pi n f_s t} \right\}, \quad (9)$$

$$X_s(f) = \sum_{n=-\infty}^{\infty} c_n X(f - n f_s)$$

$F\{ \}$: Fourier transform

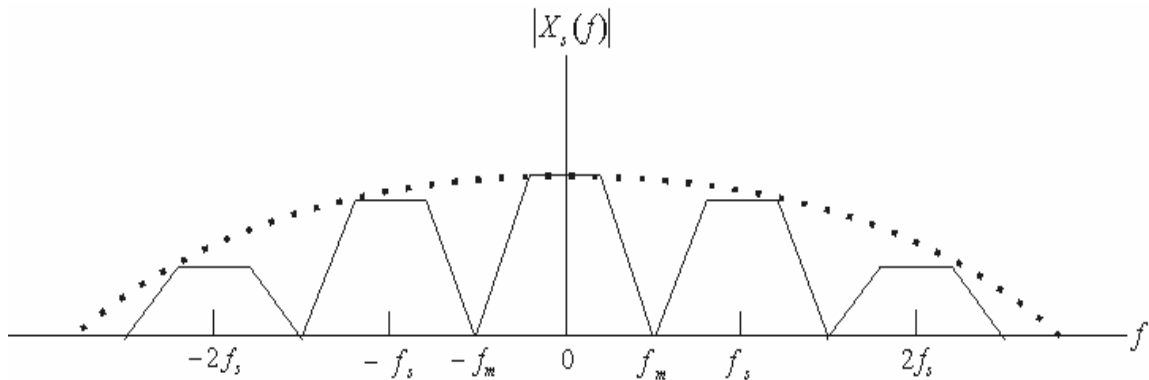


Figure 22. Sampled data in the frequency domain

The second sampling method in the analog-to-digital conversion is called natural sampling because the sampled data in the time domain, as shown in Fig. 20, still preserves the original “partial” information. However, an imperfect sampling pulse lowers the high frequency coefficients as in Fig. 21. After the Fourier method is used, no matter in time or frequency domain, the result should be straight-forward. First, sampling of the analog signal enables a cyclic frequency sweep and a duplication of the information reaches infinity in frequency spectrum. Second, as shown in Fig. 22, the frequency pattern of the sampled signal is continuous and periodic; however, the sampled signal in time domain is discrete and aperiodic [3].

Before this section concludes, there remains one more point of interest regarding analog-to-digital conversion. The sampled digital data, shown in Fig. 20, remain in an unacceptable (not simple) format for the digital interface, because the non-flat top of the waveform is “analog.” The digital signal has to be processed one more step; that is, the quantization has to take place, as shown in Fig. 23.

In Fig. 23, the quantization is based on the assumption of 3-bit ADC. The flattened data are categorized according to uniform mapping, and the digital sequence is {100, 100, 101, 110, 111, 011, 100, 010, 001}. The quantization error is introduced if a digitized signal is rounded by the mapping level [3].

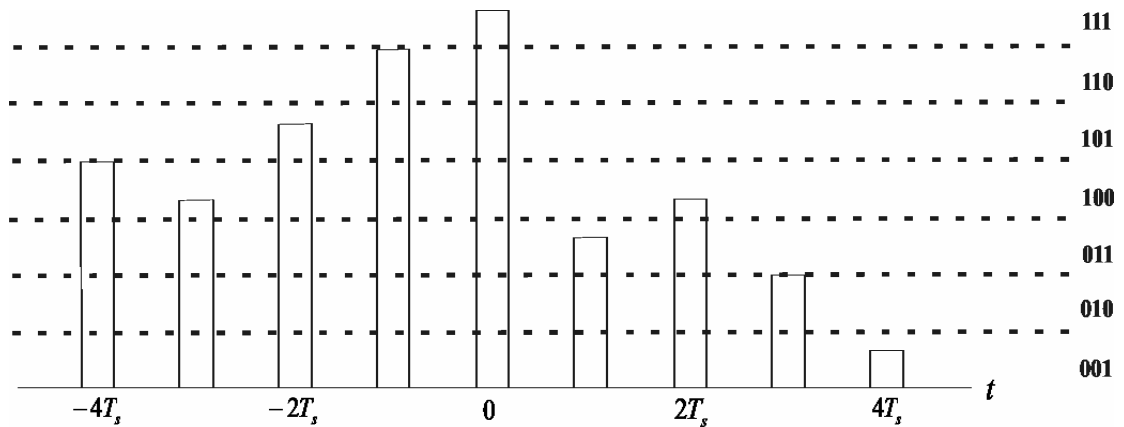


Figure 23. Digitized data in the quantization mappings

Figure 24 illustrates the designed all-optical ADC block diagram, and the frequency transition in each unit is included. The first high frequency component in the ADC is considered, as shown in the block diagram, there is no frequency-processing scheme required in the ADC.

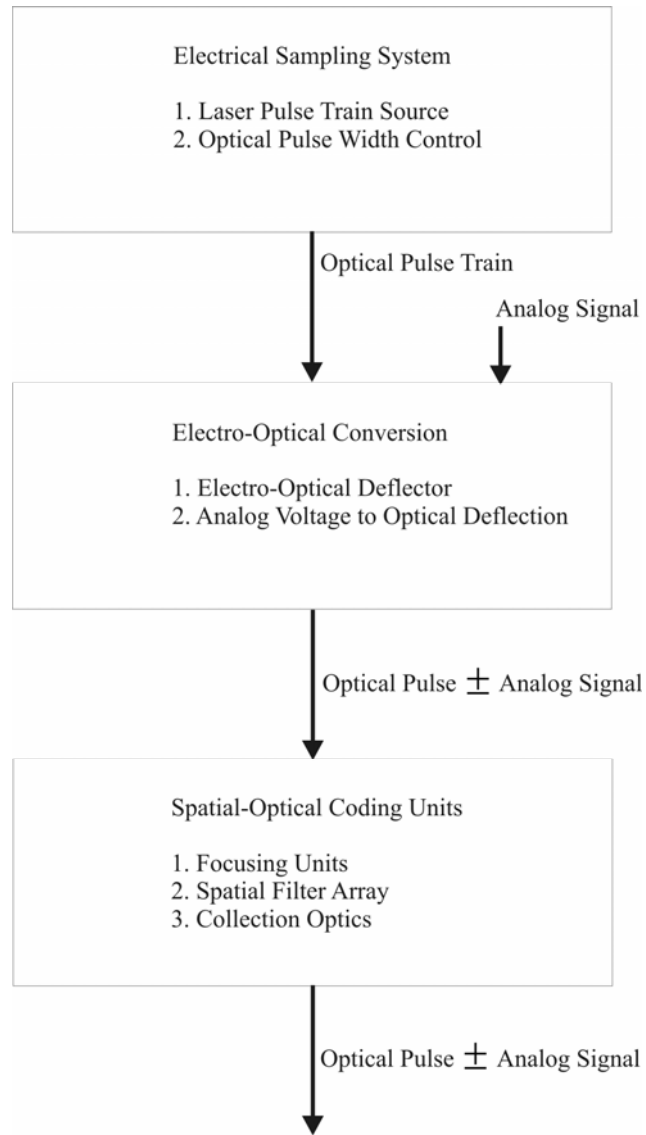


Figure 24. All-optical ADC flow diagram.

Figure 25 is a simple diagram that illustrates the all-optical ADC system in this research.

The diagram also describes the fundamental operation of the all-optical ADC in Fig. 24.

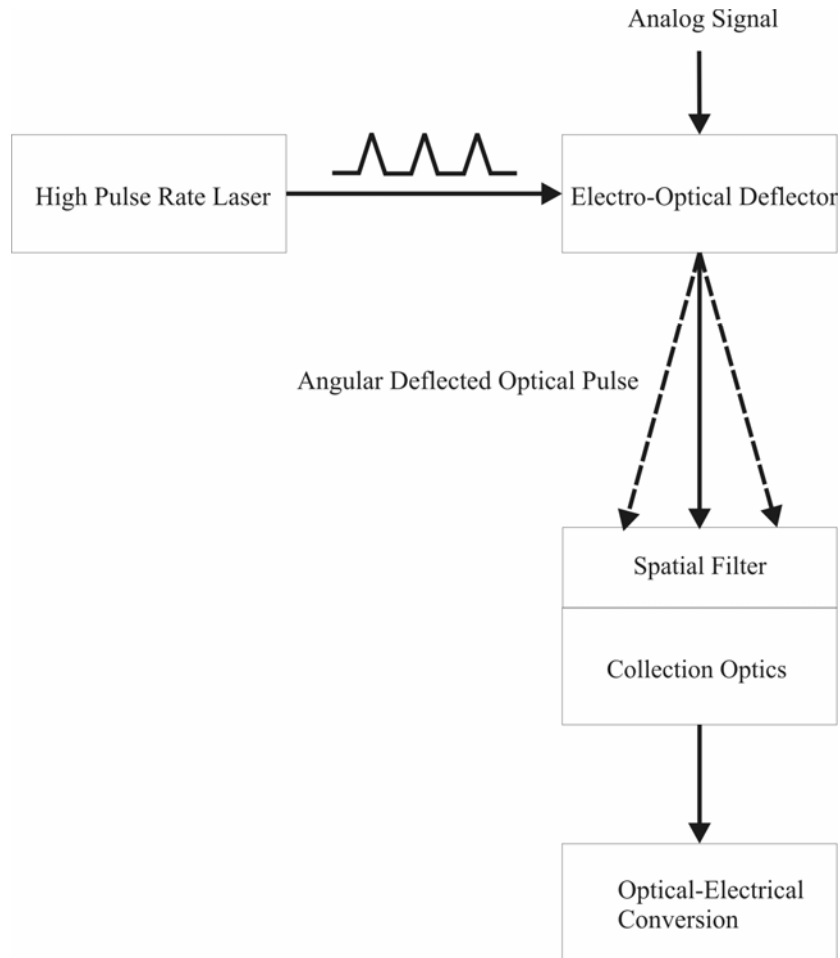


Figure 25. All-optical ADC data diagram.

1.3 All-optical analog-to-digital converter

The all-optical ADC is designed for application in advanced electro-optical sensors and advanced radar module, where a combination of high bandwidth (10's GHz) and high resolution (>10 bits) are required.

The basic operation of the ADC is illustrated in Fig. 26. In particular, the figure shows the basic structure of a 2-bit ADC, which involves an optical pulse that will be deflected by the electrical signal when passing through the deflector [8]. The angular deflection of the probe optical pulse for an analog voltage of zero is also zero and corresponds to the center of the spatial filter [9]. A positive analog voltage results in a deflection in a positive-phase direction, and a negative voltage results in a deflection in a negative-phase direction.

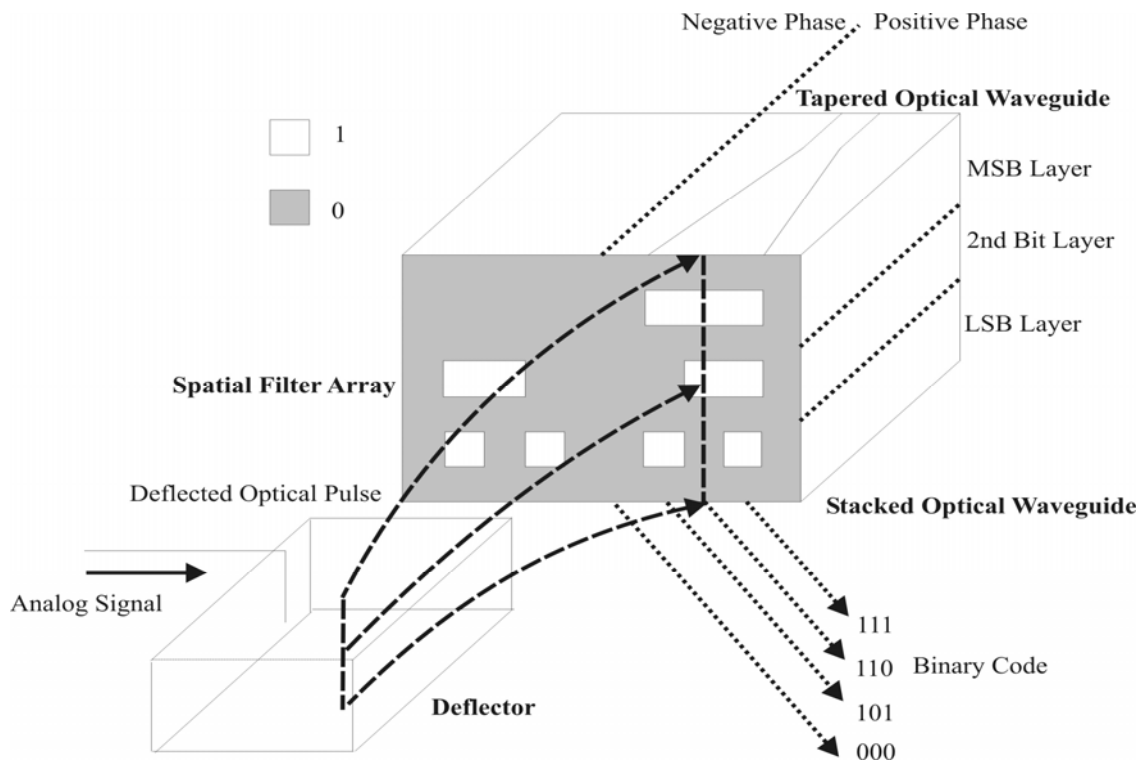


Figure 26. All-Optical ADC structure

For example, if an analog signal of 2 arbitrary units comes in, the deflector is designed so that the optical pulse, will be deflected and strike the position labeled “110” (the first “one” represents the positive unit) in the spatial filter. The deflected optical pulse will pass through both the integrated optical waveguide and the output to another integrated photodetector to be identified. If the analog signal is zero, then the optical pulse will strike only the center of the spatial filter labeled “000,” and the collection optics will transmit no optical energy; the photodetector will identify the output end of the collection optics as zero.

On the basis of the proposed structure in Fig. 26, we define the subsystems of the ADC.

1. Electro-optical sampling units
 - High pulse rate laser source (10’s GHz)
2. Electro-optical conversion units
 - Microwave electro-optical deflector (10’s GHz)
3. Spatial-optical coding and collection units
 - Focusing units
 - Binary coded spatial filter array
 - Tapered waveguide – Collection optics

For the significant characteristics of the all-optical ADC, they are summarized as followings

1. All-passive optical components

The purpose of the passive optical component is to reduce power consumption and weight. The modulation or sampling task in the proposed ADC will be accomplished by the deflecting interface; therefore, there is no electrical power for the extra modulator or amplifier. After the sampling and the direct quantization which will be introduced later, no further frequency domain action has to be taken and no extra integrated electrical device is needed.

2. Direct decimal-to-binary conversion

The all-optical ADC needs no wavelength or spatial multiplexing of the analog signal. In the following, the linear matrix transformation is used to model the direct decimal-to-binary conversion.

$$2^N = f \cdot \tau \quad (10)$$

N : number of bits, f : operation frequency (Hz), τ : random access time, deflector response time (sec)

Random access time (1) means the average time it takes for a deflected signal to move from the present location to the next one, and (2) refers to the response speed of the deflector. By extending the linear spatial transform in [9], the transform matrix can be defined as [10]

$$Y = HU \quad (11)$$

H : spatial filter array of $(2^n - 1) \times N$ matrix, U : input analog signal, Y : binary-encoded optical signal

Assume that $N=3$ and that the spatial filter is composed of 2 binary bits and 1 polarity bit. If signal of 2 in analog units is the input, and the spatial filter matrix is

$$H = \begin{bmatrix} MSB \\ 2nd \text{ bit} \\ LSB \end{bmatrix} = \begin{bmatrix} 1 & 1 & 1 & 0 & 0 & 0 & 0 \\ 1 & 1 & 0 & 0 & 0 & 1 & 1 \\ 1 & 0 & 1 & 0 & 1 & 0 & 1 \end{bmatrix}, U = [0 \ 1 \ 0 \ 0 \ 0 \ 0 \ 0]^T;$$

then the encoded optical signal is $Y = [1 \ 1 \ 0]^T$. The first “1” means the positive analog unit, and the second “1” means 2 in conventional binary code. The spatial filter array simply achieves a decimal-to-binary conversion, and the matrix form implies that a complex geometric design can be applied.

Chapter 2. Analog-to-digital converter limitation

This chapter will describe (1) the conventional types of ADCs performance and (2) the general rules for evaluation of the ADC performance. The limitations of an ADC originate from the physical and circuitry nature of the quantization of the analog signal. The trade-offs of the structures and limitations of the ADC are quantized by the mathematical model to be analyzed. Therefore different types of ADCs can be designed to fulfill different requirements because of the applications. The second section will briefly define different universal measures for evaluations of ADCs, and the dynamic measures of ADCs: Signal-to-Noise Ratio (SNR) and Spurious Free Dynamic Range (SFDR).

2.1 Analog-to-digital converter architectures

The conventional types of high-speed ADCs are described in the following:

1. Sigma-delta Modulator ADC system [11]

As shown in Fig. 27, the sigma-delta modulator is composed of a differential amplifier, a comparator, an integrator, and a 1-bit Digital-to-Analog Converter (DAC) in negative feedback. This structure requires much fewer analog components than other kinds, and the back-end digital filter of tunable center frequency such as $Sinc^3$ filter shown in Fig. 27. The negative feedback of the DAC (simple switch box) also enables noise shaping of this particular design.

The SNR can be improved by using higher orders for the sigma-delta modulator ADC than the 1st order in Fig. 27; however, circuit complexity will be higher as well.

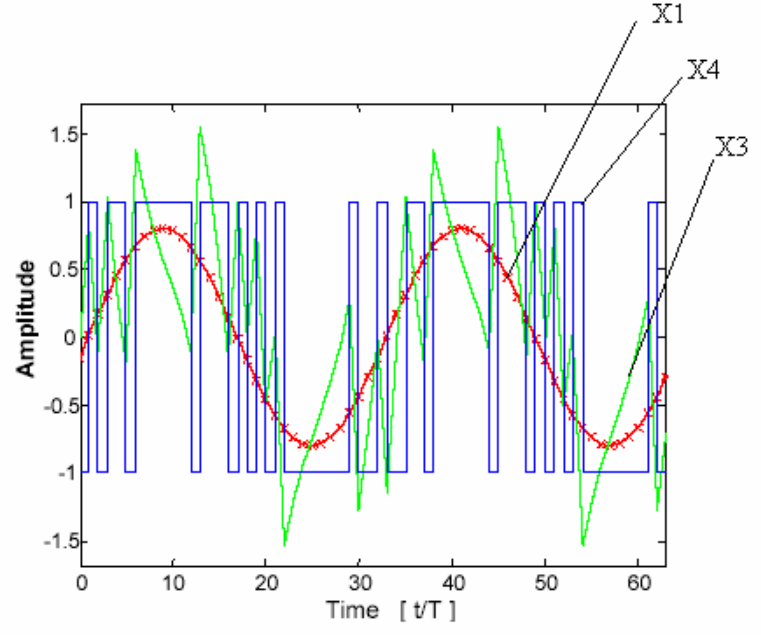
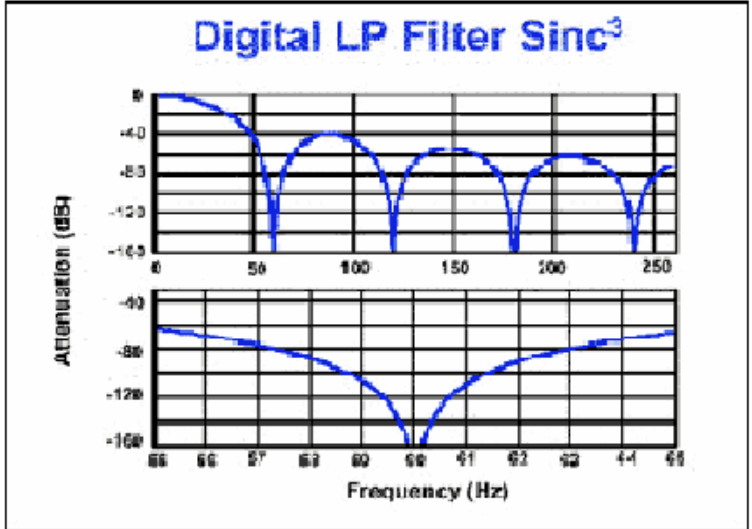
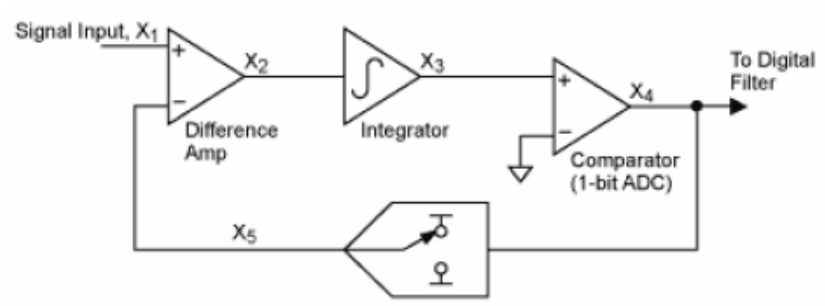


Figure 27. Sigma-delta ADC [11].

2. Pipelined ADC [12]

The pipelined ADC includes low-resolution ADCs, DACs, summing circuits, and an interstage amplifier. Large power consumption, high nonlinearity, and interstage gain error are the main limitations to this structure.

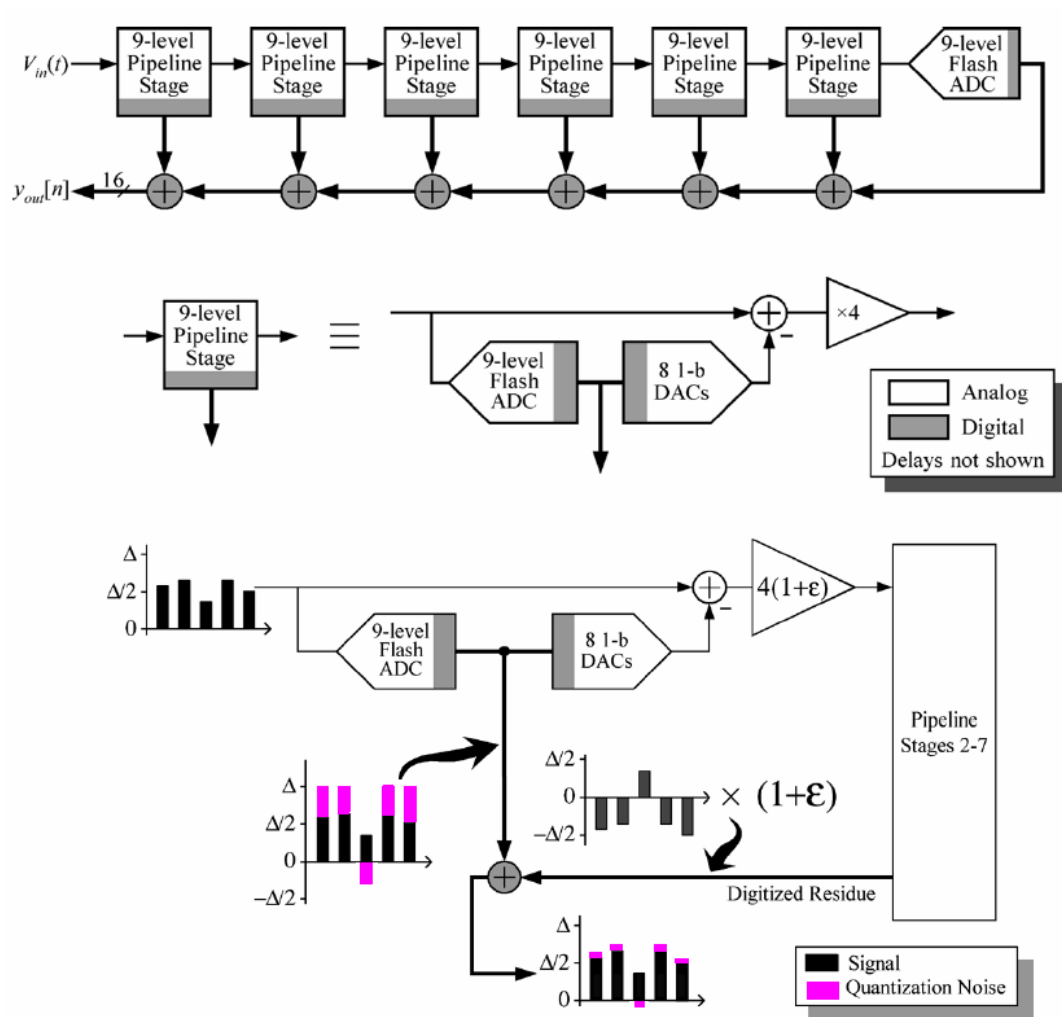


Figure 28. 15-bit pipelined ADC [12].

As shown in Fig. 28, the analog input $V_{in}(t)$ is converted in the first pipeline stage. In the first stage, the output of the ADC will be back-converted by the DAC and subtracted from the original $V_{in}(t)$. The difference is called “residue”, and amplified by the factor of 4.

The residue will be processed by the same operation in the second stage. The final single flash ADC in the pipelined structure resolves the last 3 least significant bits.

The structure shown in Fig. 28 encoded the analog signal to 9 levels (slightly higher than 3-bit, 8 levels), and also illustrates an example of the interstage gain error of ϵ to describe how it affects the digitization.

3. Flash ADC [13]

The flash ADC is the simplest and fastest structure for parallel high-speed processing. The flash ADC is composed of the comparator bank which requires higher power consumption and a larger size than the other kinds of ADCs. Also, the component matching to the comparator channels in the chip integration is one limitation of the flash ADC.

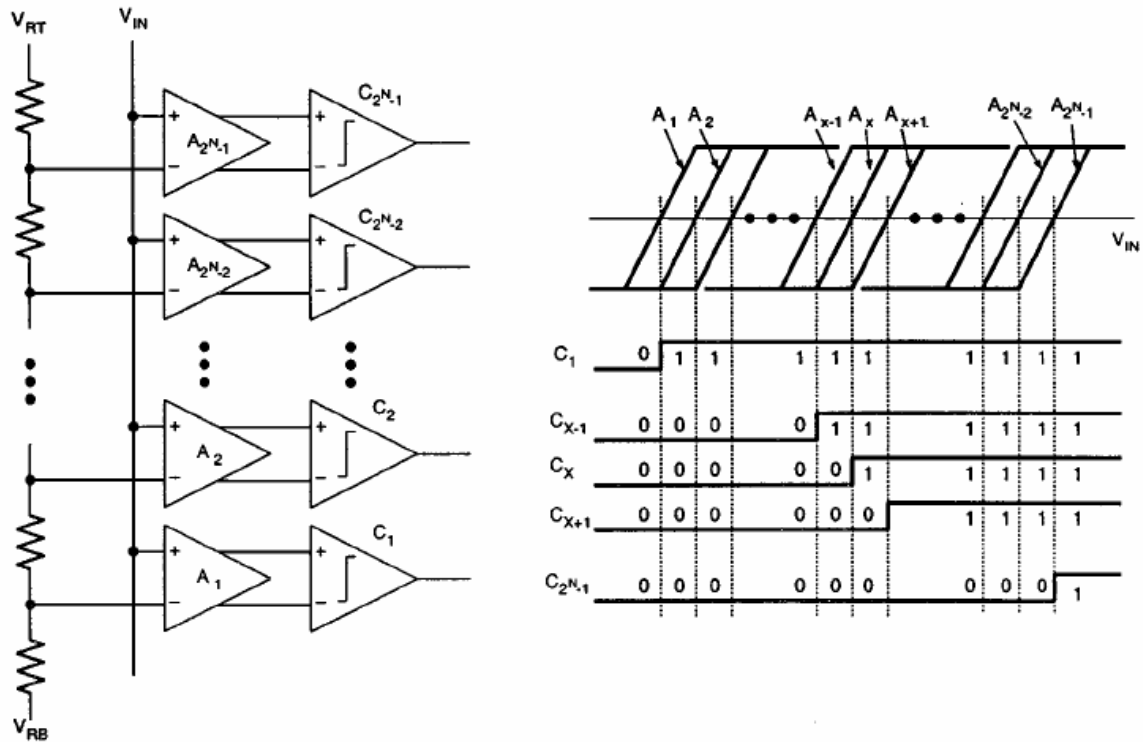


Figure 29. Flash ADC [13].

4. Time-interleaved ADC [14]

The time-interleaved ADC uses a multiplexing switch to distribute analog data to parallel-located ADCs in sequence. Therefore, the slower ADCs can be used to achieve a higher speed of conversion. Systematic jitters between channels (time skews), offset, and gain mismatches are the main limits to this structure.

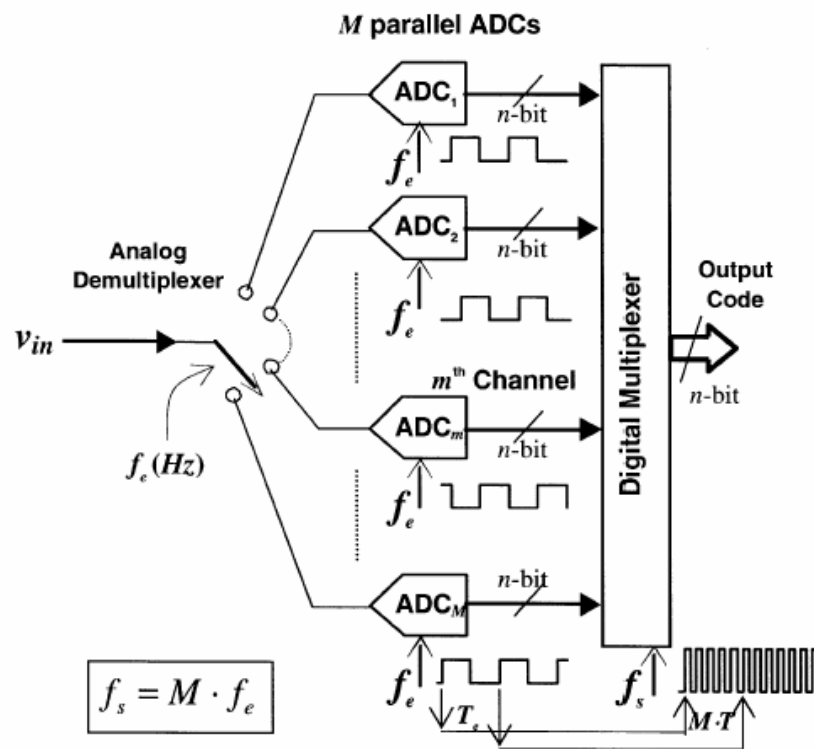


Figure 30. 4-channel time-interleaved ADC [14].

2.2 Analog-to-digital converter measures

1. Signal-to-Noise Ratio (SNR) [3]

Signal-to-Noise Ratio (SNR) applies a calculation of the white-noise approximation (uniform distribution) to the quantization error representation. The quantization noise power, P_q , is defined as

$$P_q = \frac{A^2}{3 \cdot 2^{2b}} \quad (12)$$

where A is the maximum amplitude of the signal, and b is number of bits.

The quantization step is $\Delta = \frac{2A}{2^{2b}}$ as illustrated in Fig. 31. b is the resolution of the ADC.

The average power of the original signal if there is a sinusoidal input analog wave is

$$P_{analog} = \frac{1}{T} \int_0^T (A \sin \omega t)^2 dt = \frac{A^2}{2} \quad (13)$$

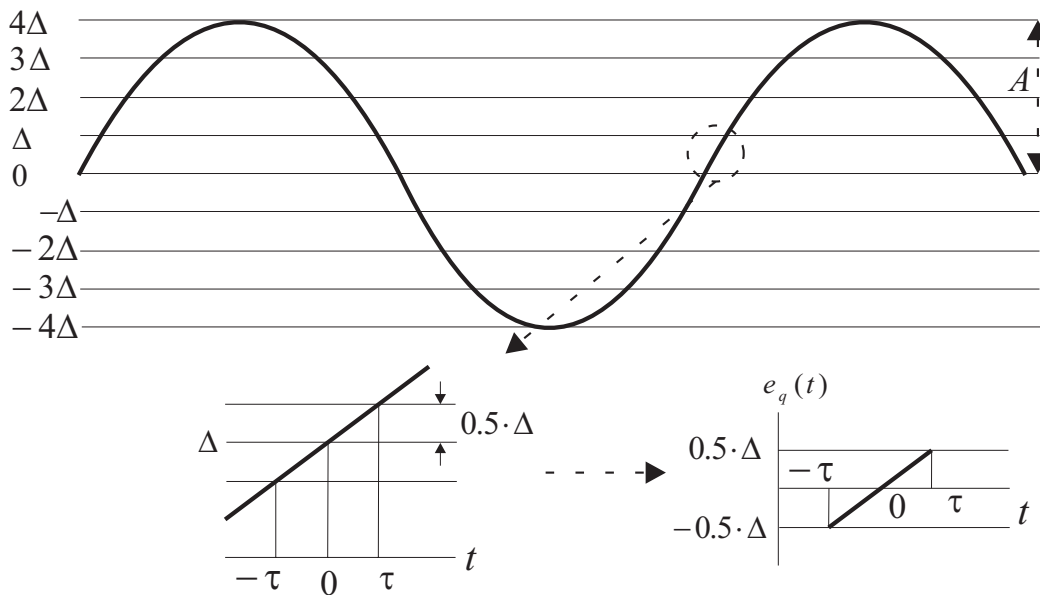


Figure 31. Signal-to-noise ratio (SNR) illustration [3].

Therefore SNR is defined as

$$SNR_{dB} = 10 \log_{10} \left(\frac{P_{analog}}{P_q} \right) = 6.02 \cdot b + 1.76 \quad (14)$$

2. Spurious Free Dynamic Range (SFDR) [15]

SFDR represents the ratio of the fundamental frequency amplitude to the largest nonsignal-related component in the Nyquist spectrum. The Nyquist spectrum is half of the sampling frequency.

The effective bit determined by the SFDR is

$$SFDR_{bit} = \frac{SFDR(dBc)}{6.02} \quad (15)$$

Figure 32 shows an example of the full spectrum. $0 \sim \frac{f_s}{2}$ is the Nyquist spectrum.

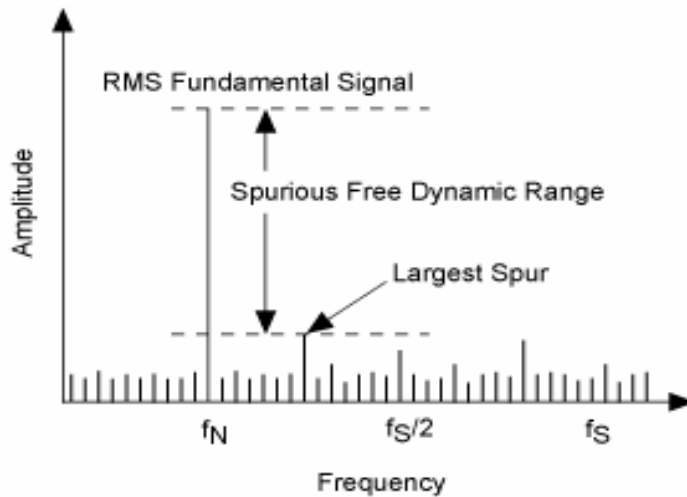


Figure 32. Spurious Free Dynamic Range (SFDR) [15].

Except the two commonly used dynamic measures of the ADC, the universal measures of the ADC are (1) the product of the effective quantization number and sampling rate P and (2) figure of merit F , which will be introduced. They are defined as

$$P = 2^{SNR_{bit}} \cdot f_s, F = \frac{2^{SNR_{bit}} \cdot f_s}{P_{diss}}, SNR_{bit} = \frac{SNR_{db} - 1.76}{6.02} \quad (16)$$

P_{diss} : power consumption.

Figures 33 and 34 illustrate the parameters of the F and P ADCs in the market. In Fig. 33, P is calculated and distributed in the range of $1.024 \times 10^{11} \sim 4.096 \times 10^{11}$. As shown in Fig. 34, power consumption is considered. The results show that the same ADCs of different parameters will have different measures, and they are randomly distributed.

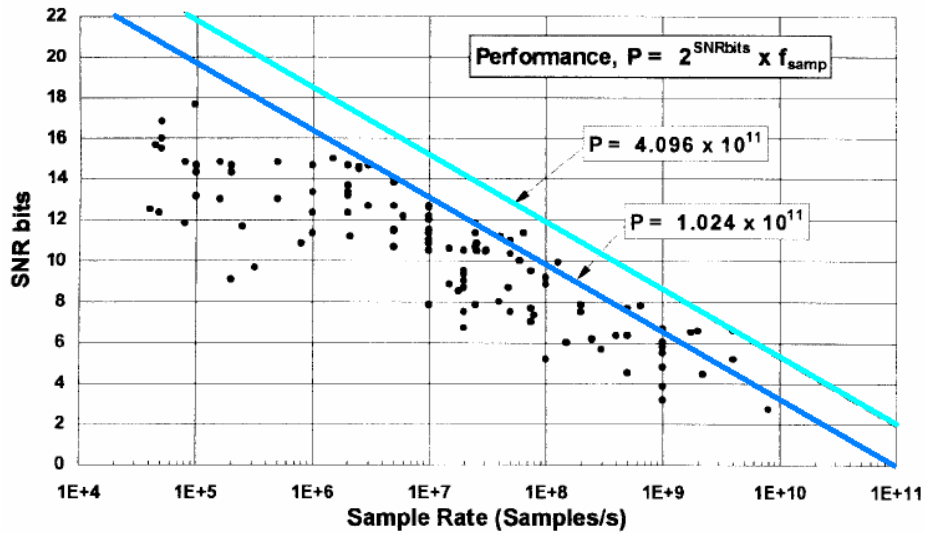


Figure 33. Product of the effective quantization number and sampling rate [16]. The state of art is $1.024 \times 10^{11} < P < 4.096 \times 10^{11}$.

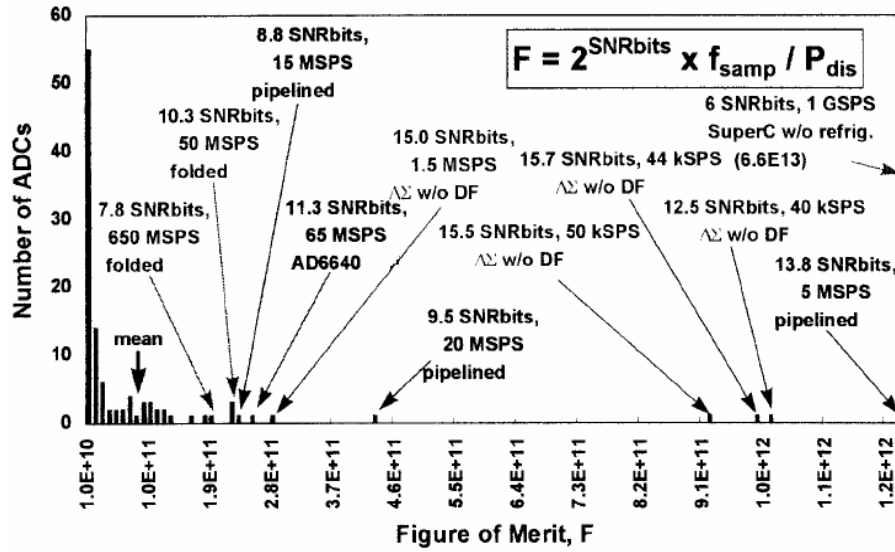


Figure 34. Figure of merit [16]. The average of F is 7.9×10^{10} .

From the investigation concluded in [16], these three factors limit ADC performance in different specifications respectively. The limitation Factors of the resolution according to the different sampling rates are as follows:

$$f_s \leq 2M \text{ samples/s: Thermal noise}$$

$$2M \leq f_s \leq 4G \text{ samples/s: Aperture jitter}$$

$$4G \leq f_s \text{ samples/s: Comparator ambiguity}$$

They are used to calculate the achievable resolution on the basis of physical phenomenol in the ADC.

1. Thermal Noise

$$B_{thermal} = \log_2 \left(\frac{(2 \cdot A)^2}{6 \cdot k \cdot T \cdot R_{eff} \cdot f_s} \right)^{0.5} - 1 \quad (17)$$

k : Boltzmann's constant= $1.380658 \cdot 10^{-23} J / K$, T : temperature in K , R_{eff} : effective thermal resistance.

2. Aperture Uncertainty

$$B_{aperture} = \log_2 \left(\frac{2}{\sqrt{3} \cdot \pi \cdot f_s \cdot \tau_a} \right) - 1 \quad (18)$$

τ_a : standard deviation of the variation of the sampling position in t .

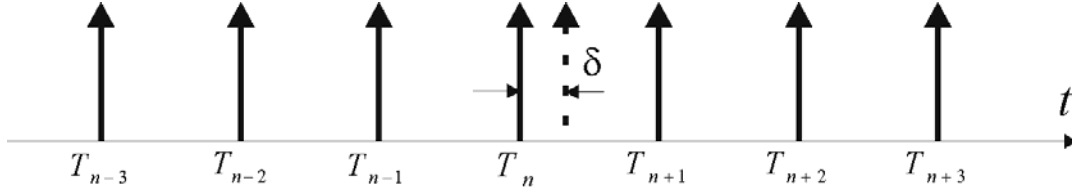


Figure 35. Aperture jitter [17].

3. Comparator Ambiguity

$$B_{ambiguity} = \frac{\pi \cdot f_T}{6.93 \cdot f_s} - 1.1 \quad (19)$$

$f_T = \frac{2.5}{\pi \cdot t_{reg}}$, f_T : unity current gain frequency of the transistor, t_{reg} : regeneration time

constant of the comparator.

4. Heisenberg Uncertainty Principle

$$2^b \cdot f_s \leq \frac{A}{\sqrt{\hbar \cdot R}} \quad (20)$$

R : impedance, $\hbar = \frac{h}{2 \cdot \pi}$, $h = 6.62617 \cdot 10^{-34} J \cdot s$: Planck's constant.

2.3 Comparisons and trade-offs of analog-to-digital converter architectures

Table 1 is the comparison table of the previous ADC architectures. The comparisons are based on application, resolution, core die size, and power consumption.

	Flash ADC	Pipelined ADC	Time-Interleaved ADC	Sigma-Delta ADC
Application	Satellite communication or radar processing	Charge-coupled device imaging, digital video application	Radar system and high-speed processing application	Audio instrumentation and sonar processing
Resolution	8-bit resolution	8-to-14-bit resolution	8-bit resolution	12-to-16-bit resolution
Size	Core size increases with the exponential function of resolution	Core size increases with the linear function of resolution	Core size increases with the linear function of resolution	Core size does not increase with the function of resolution
Power Consumption	Increases with the exponential function of resolution	Low power consumption	Increases with the linear function of resolution	Low power consumption
Sampling Speed or Bandwidth	Higher than 4GHz	Several M~100 M samples/s	40 M samples/s or higher rates	Low speed, bandwidth is less than 1MHz

Table 1. Comparisons of ADCs [18].

As shown in Fig. 36, the analog-to-digital conversion time of sigma-delta ADCs and pipelined ADCs increases linearly with the number of bits (resolution). However, the conversion time does not have the same impact on the flash converter because of the parallel structure, which is shown in Fig. 8.

Component matching affects pipelined and flash converters much more than it affects the sigma-delta converter. Calibration and trimming techniques are used to solve this problem. The most significant advantage of the flash converter is the fast processing speed of the parallel structure; however, this speed necessitates much higher complexity and chip size than the do other approaches. Also, power consumption in the flash converter is much higher than in others once the resolution increases.

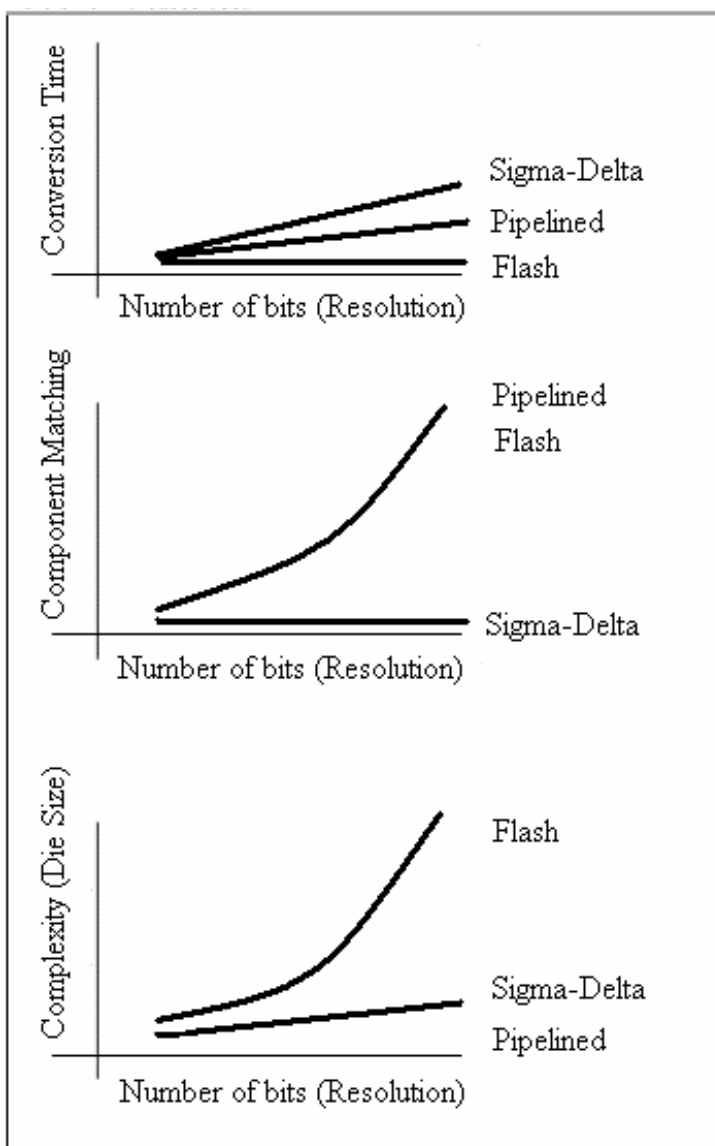


Figure 36. Trade-offs of ADC architectures [19].

2.4 Optical ADC

In this section, several examples of the optical ADCs will be introduced. The objectives of the optical ADC are to overcome the limitation described in the previous sections, and also prevent trade-offs as possible. The example of optically assisted ADC is shown in Fig. 37 and is called as hybrid ADC [20], because the optical components dominate more than in the Complementary Metal Oxide Semiconductor (CMOS) ADC, as shown in the previous example. The proposed structure is expected to have the performance of 6-bit 15 GHz, and the optical signal helps out, especially in the channel multiplexing function.

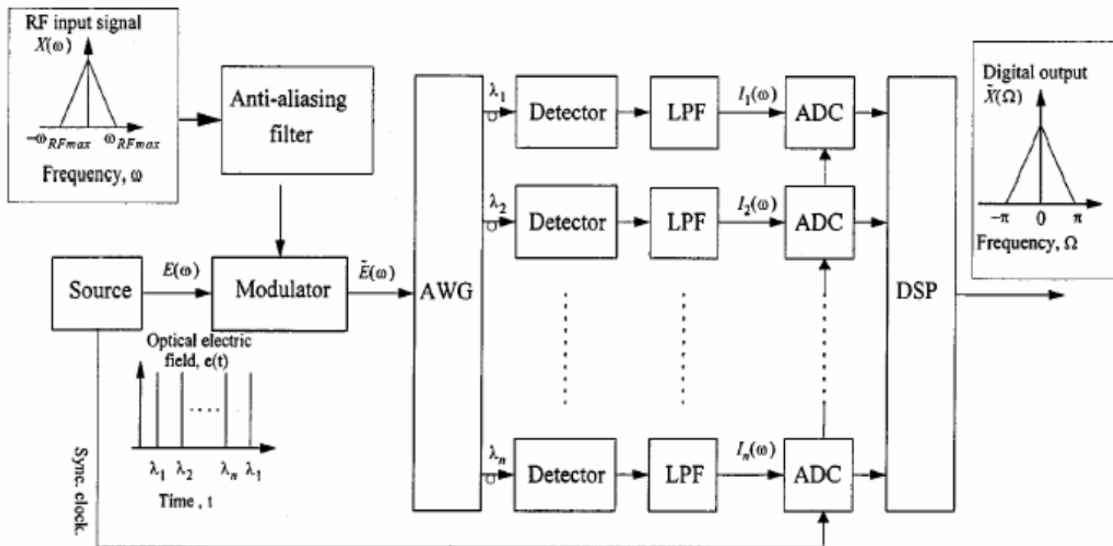


Figure 37. Optically assisted ADC [20]

The sampling (modulating) task is also accomplished by the optical pulse but makes use of the wavelength multiplexing distribution. The analog-to-digital conversion is processing in the wavelength (λ) domain instead of the time (t) domain, which is more familiar to us. The processing speed can be greatly enhanced because of the use of Arrayed Waveguide Grating (AWG), and more numbers of ADCs can be used than the CMOS ADC.

We now turn to the examples illustrated in Fig. 38. The structure is called all-optical ADC [21] because the system is composed entirely of active and passive optical devices.

The expected performance is 8-bit 12.5 G samples/sec.

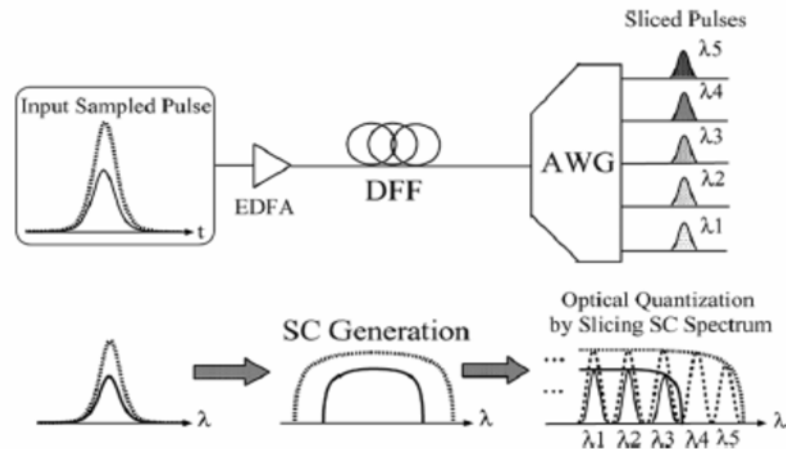
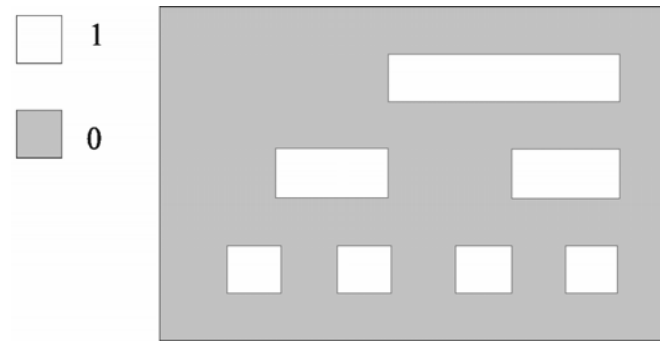


Figure 38. All-optical ADC [21]

In the all-optical ADC, the key means to enhance the processing speed more than the optically assisted ADC is to bypass the electrical method. The outgoing optical pulse of the AWG will depend on the intensity of the input optical pulse. The dependency of the input-to-output feature is designed to form the optical quantization. Therefore, no electrical devices are involved in the analog-to-digital conversion steps in the previous section.

In Fig. 39, the uni-directional ADC is proposed [9]. The ADC makes use of the acousto-optical deflection to accomplish sampling and quantization steps, however, the design sets a limit to positive analog voltage only. The analog-to-digital conversion speed and specifications are also as described in Chapter 1.



Binary Code (000, 001, 010, 011, 100, 101, 110, 111)

Figure 39. Optically assisted ADC [9]

As the measurements recorded in [9], the acousto-optical deflector of 500 MHz is assumed and 4-bit resolution is used. The extended positive and negative dual-directional scanning modeling has also already shown in the Chapter 1, therefore the deflection speed as shown in Fig. 39 is the same as the conceptual one.

Chapter 3. Basics of research methods

3.1 Wave optics

Analyzing the arrival of the optical impulse with the spatial filter geometry receives an understanding of the wave equation. In this section, the wave equations [22] will be defined in their 1-dimensional and 3-dimensional aspects, and demonstrate the formulation of the wave distributions in the optical waveguide [23]. Figure 40 illustrates a fundamental 1-dimensional wave, and its parameters are defined as

$$\psi(z, t) = \psi_0 \cos(kz - \omega t) \quad (21)$$

$$\omega = 2\pi \cdot \nu, \quad \lambda = \frac{2\pi}{k}, \quad c = \nu \cdot \lambda, \quad c = \frac{1}{\sqrt{\mu_0 \epsilon_0}}$$

ω : angular frequency, radians. k : propagating constant. λ : wavelength. c : speed of light in vacuum, $3 \cdot 10^8$ meters per second (m/s). ν : wave frequency. ϵ_0 : permittivity of vacuum, $8.854 \cdot 10^{-12}$ farads per meter (F/m). μ_0 : permeability of vacuum, $4\pi \cdot 10^{-7}$ henries per meter (H/m).

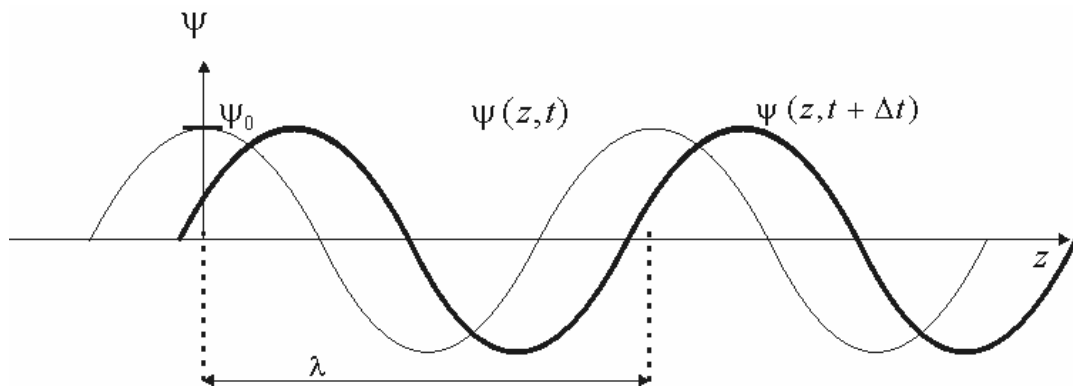


Figure 40. 1-Dimensional wave

The plane harmonic wave satisfies the wave equation

$$\frac{\partial^2 \psi}{\partial z^2} = \frac{1}{u^2} \frac{\partial^2 \psi}{\partial t^2}, \quad u = \frac{\omega}{k} \quad (22)$$

u : phase velocity

In the 3-dimensional scalar representation, the linearly polarized optical wave is

$$E = E_0 \cos(k \cdot r - \omega t), \quad H = H_0 \cos(k \cdot r - \omega t) \quad (23)$$

$$k \cdot r - \omega t = k_x x + k_y y + k_z z - \omega t = \text{constant}$$

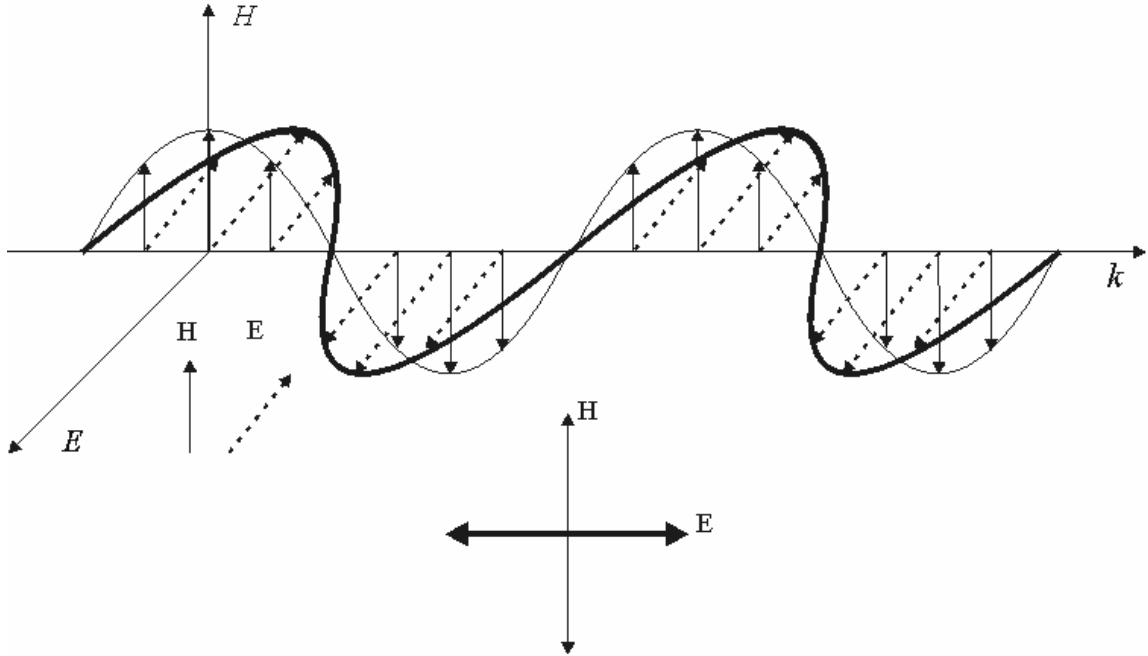


Figure 41. 3-Dimensional linearly polarized wave

The 3-dimensional wave also satisfies the scalar wave equation

$$\frac{\partial^2 \psi}{\partial x^2} + \frac{\partial^2 \psi}{\partial y^2} + \frac{\partial^2 \psi}{\partial z^2} = \frac{1}{u^2} \frac{\partial^2 \psi}{\partial t^2}, \quad u = \frac{\omega}{k} = \frac{\omega}{\sqrt{k_x^2 + k_y^2 + k_z^2}} \quad (24)$$

From the plane wave and the 3-dimensional wave definitions, the general wave definitions are described by curl Maxwell's equations as follows

$$\nabla \times E = -\mu \frac{\partial H}{\partial t}, \quad \nabla \times H = \varepsilon \frac{\partial E}{\partial t} \quad (25)$$

$\mu = \mu_0 \mu_r$, $\varepsilon = \varepsilon_0 \varepsilon_r$. μ_r , ε_r : relative permeability and permittivity of transmitting medium. $\nabla \times ()$: curl operation. The divergence relationships in the homogeneous medium accompanying the curl equations are

$$\nabla \cdot E = 0, \nabla \cdot H = 0. \nabla \cdot () = \hat{i} \frac{\partial}{\partial x} + \hat{j} \frac{\partial}{\partial y} + \hat{k} \frac{\partial}{\partial z} \quad (26)$$

The curl Maxwell equations will also be the fundamentals for the calculations in this research. The optical energy per unit area is called the Poynting vector, which is defined as

$$S = E \times H = E_0 \times H_0 \cos^2(k \cdot r - \omega t) \quad (27)$$

$$I = \frac{1}{2} E_0 H_0 = \frac{n}{2Z_0} |E_0|^2, Z_0 = \sqrt{\frac{\mu_0}{\epsilon_0}}, n = \frac{c}{u}$$

I : average Poynting vector, also called Irradiance. Z_0 : impedance of free space. n : refractive index.

In the next part of this section, the transmission and the reflection of the plane wave will be discussed. Consider the plane wave incidents from the medium 1 (n_1) at the angle of θ to the medium 2 (n_2) as shown in Fig. 42.

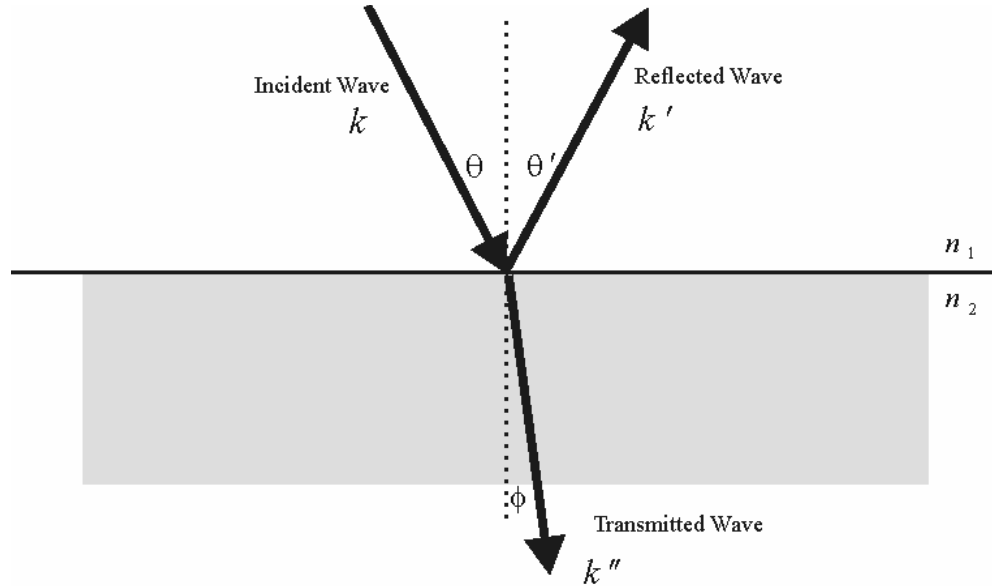


Figure 42. Plane wave transmission and reflection

The transmitted and reflected waves follow Snell's law

$$\frac{\sin \theta}{\sin \phi} = \frac{n_2}{n_1}, \quad \theta = \theta' \quad (28)$$

As shown in Fig. 43, the critical angle is defined as

$$\theta_c = \sin^{-1}\left(\frac{n_2}{n_1}\right), \quad n_1 > n_2 \quad (29)$$

Once the incident angle is greater than the critical angle, the plane wave will be totally reflected.

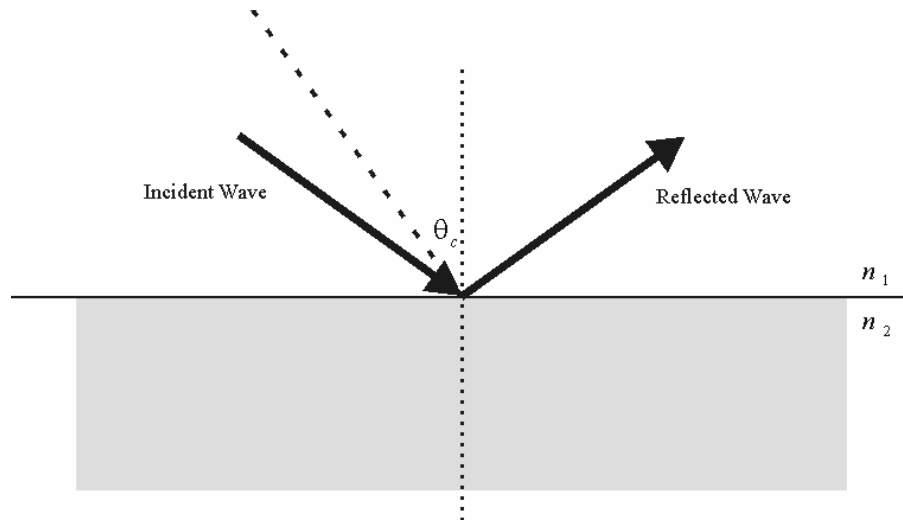


Figure 43. Incident angle is larger than the critical angle

The special case, as shown in Fig. 44, occurs when $\theta = \theta_c$, so that the reflected wave will be the surface wave. The surface wave [24] in Fig. 43 is neglected because the wave will be totally attenuated in a few wavelengths.

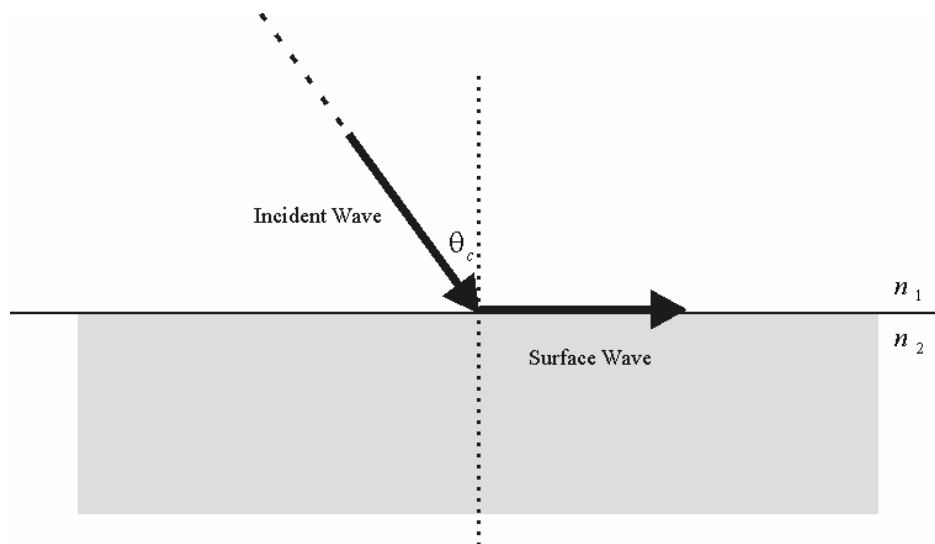


Figure 44. Critical angle

If the electric and magnetic fields are considered in the transmission-reflection relationship, the different transverse modes will be defined. The linearly polarized waves [25] can be categorized as two modes: Transverse Electric (TE) and Transverse Magnetic (TM) polarizations. In the TE mode, the electric field is in the y -axis (positive y -direction) and is perpendicular to the plane of incidence. Figure 45 illustrates the TE mode case, and the XZ plane is defined as the plane of incidence.

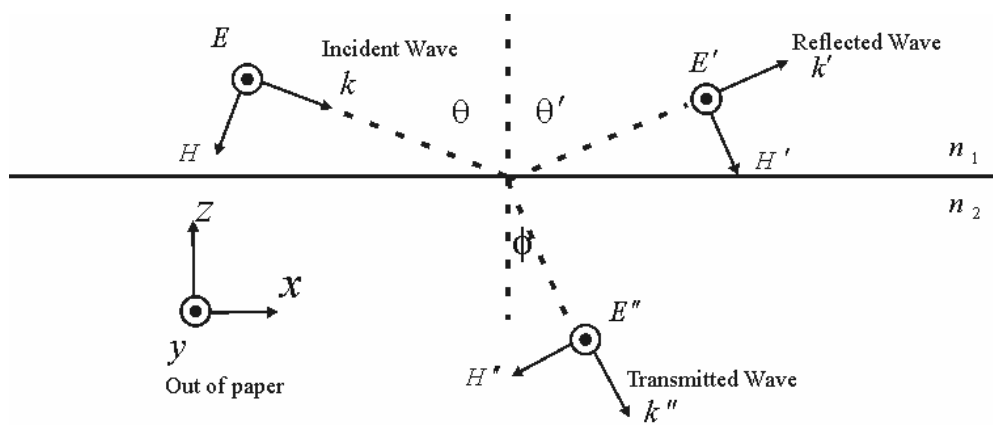


Figure 45. TE mode

The electric fields' and the magnetic fields' relationships in the TE mode are defined as

$$E + E' = E'', \quad -H \cos \theta + H' \cos \theta = -H'' \cos \phi \quad (30)$$

In Fig. 46, concerning the TM mode, the magnetic fields are defined in the positive y -direction, and the electric-magnetic fields' relationships are

$$H + H' = H'', \quad -E \cos \theta + E' \cos \theta' = -E'' \cos \phi \quad (31)$$

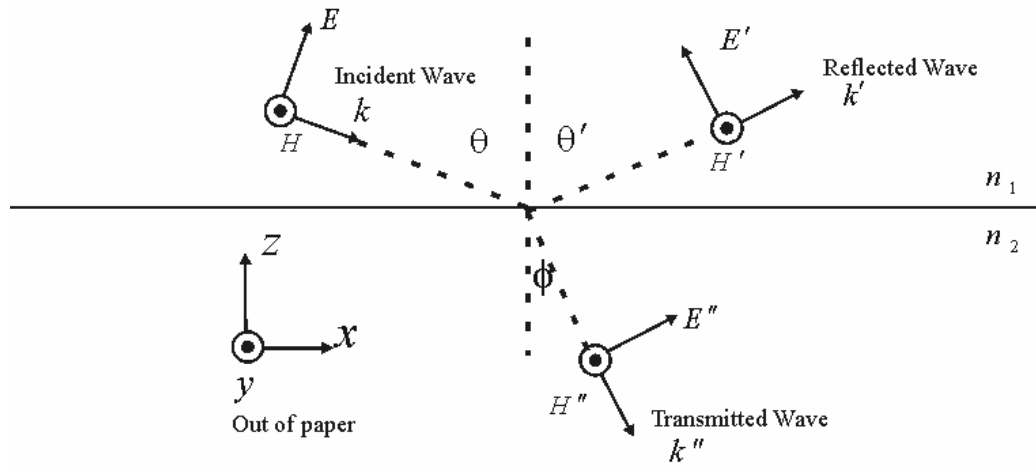


Figure 46. TM mode

3.2 Integrated optical waveguide

In this section, the wave distributions of the multi-dimensional model in the waveguide structure [23] will be defined. The relative refractive-index difference is defined in Equation 32 and the waveguide structure is illustrated in Fig. 47.

$$\Delta = \frac{n_{core}^2 - n_{cladding}^2}{2 \cdot n_{core}^2} \quad (32)$$

n_{core} : refractive index of the core region, $n_{cladding}$: refractive index of the cladding region.

In the Silicon-On-Insulator (SOI) optical waveguide design [26], Si is used as the core ($n_{core} = 3.5$) and SiO_2 as the cladding ($n_{cladding} = 1.45$) at $\lambda = 1.55 \mu m$; therefore, $\Delta = 45\%$. The silica core material is $n_{core} = 1.5$.

As illustrated in Fig. 47, the z-axis and the x-axis propagation constants are $\beta = kn_1 \cos \phi$, and $\kappa = kn_1 \sin \phi$. Also, $\phi = \sin^{-1}(n_{cladding} / n_{core})$ is the critical angle.

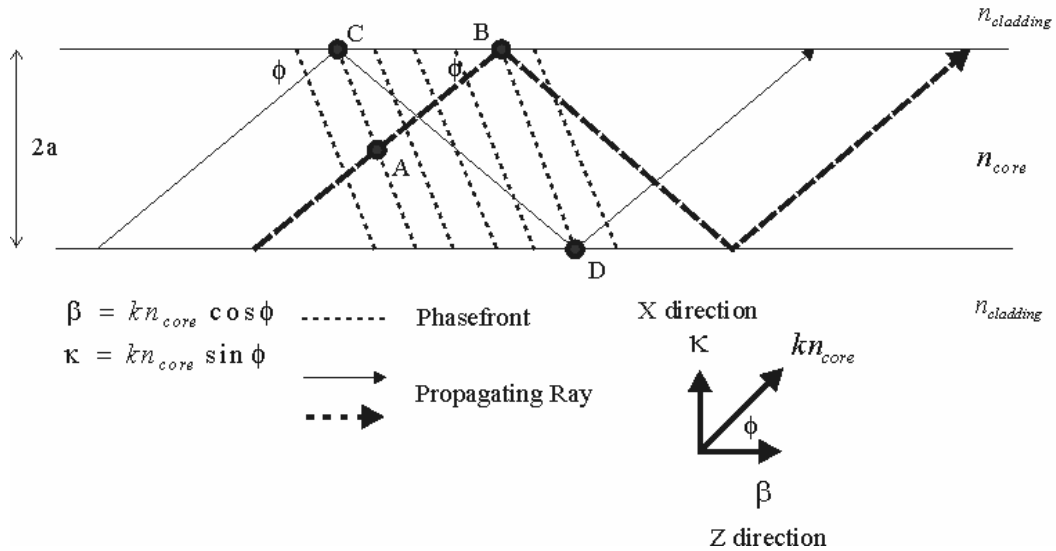


Figure 47. 1-dimensional waveguide

The dispersion relationship in the 1-dimensional waveguide structure is

$$kn_{core}a\sqrt{2\Delta} = \frac{\cos^{-1} \xi + m\pi / 2}{\xi}, \quad \xi = \frac{\sin \phi}{\sqrt{2\Delta}} \quad (33)$$

m : integer

The normalized frequency is

$$v = kn_{core}a\sqrt{2\Delta} \quad (34)$$

The cut-off wavelength is

$$\lambda_c = \frac{2\pi}{v_c} an_{core}\sqrt{2\Delta} \quad (35)$$

In this section, we should notice two important conclusions concerning the 1-dimensional wave solutions in the optical waveguide. First, $v < v_c$ ($\lambda > \lambda_c$) means no more than that the fundamental mode ($m = 0$) can be propagated in the core region and that $v_c = 0.5\pi$; this can be clearly observed in the crossing point in Fig. 48. In Fig. 47, $a = 0.5\mu\text{m}$, $n_{cladding} = 1$, $n_{core} = 3$ for the silicon core, and $n_{core} = 1.5$ for the silica core. The reason that different waveguide refractive indexes for both the waveguide core and the cladding are chosen will be stated later in this section. The commercial Matlab software [27] is used to calculate and plot the results of Equation 33.

Second, Equation 33 solves for ξ , makes use of a different m , and is denoted as ξ_m ; one can calculate ϕ_m by $\xi_m = \sin \phi_m / \sqrt{2\Delta}$, and one can calculate β_m by $\beta_m = kn_{core} \cos \phi_m$. The examples of Equation 33 are plotted in Fig. 48. In Fig. 48 (a), two modes exist in the silica core region are determined by the crossing points; however, in Fig. 48 (b), four modes are in the silicon core region because of a higher normalized frequency.

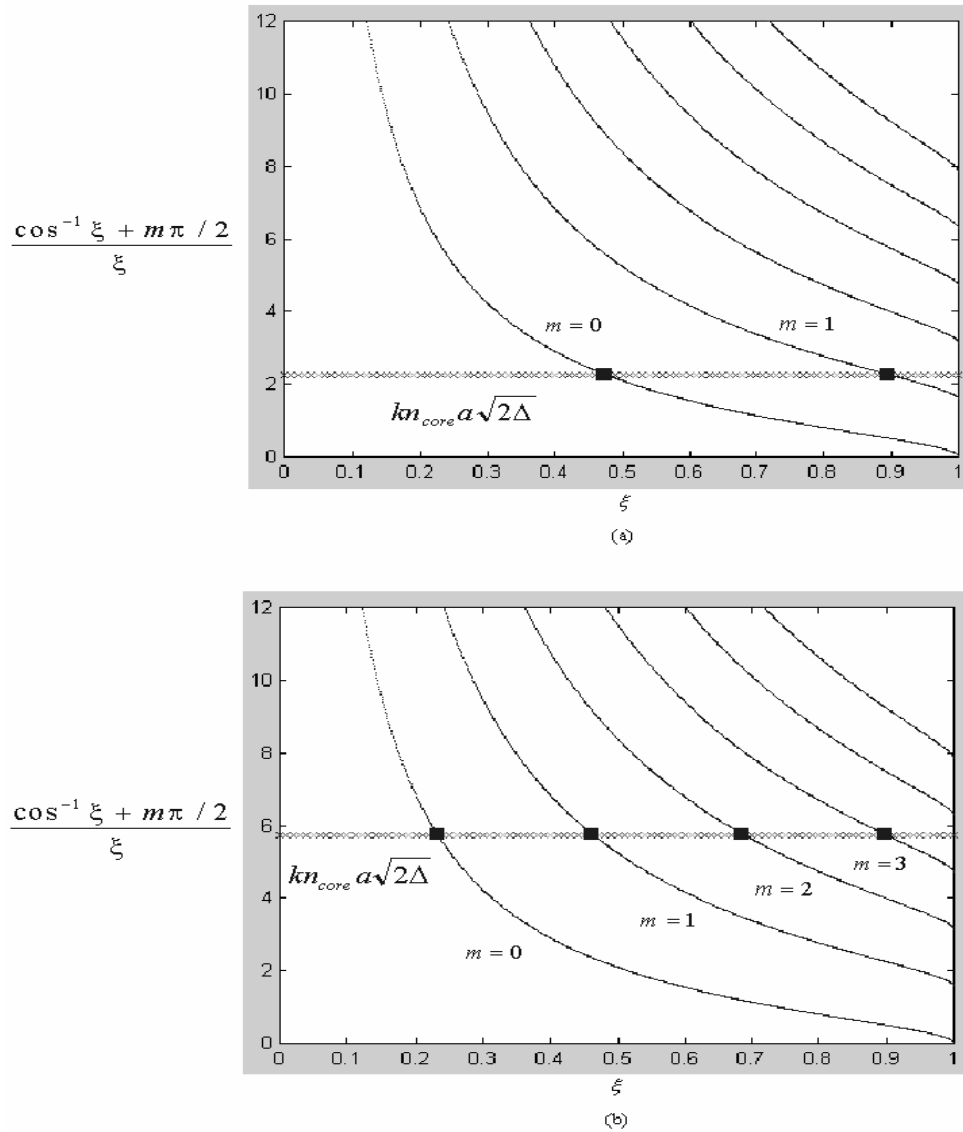


Figure 48. Matlab calculations and plots of dispersion curves of Equation 33 for (a) silica core (b) silicon core

The wave functions in the slab waveguide are based on the 2-dimensional structure and simplification of the curl Maxwell's equations. The advantages of the slab waveguide formation are twofold: the wave distributions can be greatly simplified, and the computation complexity is reduced. The wave propagation equations are defined [23] as

$$E = E(x, y)e^{j(\omega t - \beta z)}, H = H(x, y)e^{j(\omega t - \beta z)} \quad (36)$$

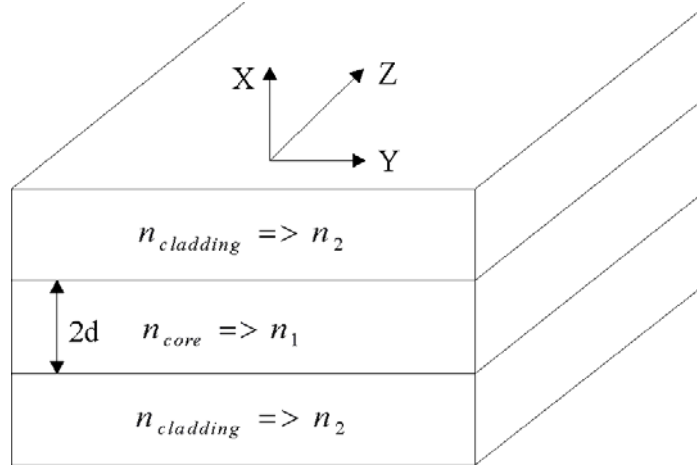


Figure 49. Slab waveguide

In the slab waveguide, the y-axis dependency is ignored ($\frac{\partial E}{\partial y} = 0$ and $\frac{\partial H}{\partial y} = 0$). The TE mode wave equation in the slab waveguide is defined as

$$\frac{d^2 E_y}{dx^2} + (k^2 n^2 - \beta^2) E_y = 0 \quad (37)$$

$$H_x = -\frac{\beta}{\omega \mu_0} E_y, \quad H_z = \frac{j}{\omega \mu_0} \frac{dE_y}{dx}, \quad E_x = E_z = H_y = 0, \quad k_2 \leq \beta \leq k_1$$

and the TM mode is

$$\frac{d}{dx} \left(\frac{1}{n^2} \frac{dH_y}{dx} \right) + \left(k^2 - \frac{\beta^2}{n^2} \right) H_y = 0 \quad (38)$$

$$E_x = \frac{\beta}{\omega \epsilon_0 n^2} H_y, \quad E_z = -\frac{j}{\omega \epsilon_0 n^2} \frac{dH_y}{dx}, \quad E_y = H_x = H_z = 0, \quad k_2 \leq \beta \leq k_1.$$

In the TE mode, the wave in the core region of E_y is to be in the form of $E_y(x, z) = A \cos(kx) e^{j(\omega t - \beta z)}$. E_y in the form of x-axis dependency is used; therefore, both $E_y(x) = A \cos(kx)$ and this triangular function proves that the optical confinement in both the core region and other wave equations in the cladding region have exponential decay.

The propagating waves along the z-axis by the x-axis dependency are

$$\begin{cases} E_y(x) = A \cos(kx), & -d \leq x \leq d \\ E_y(x) = B e^{-\alpha x}, & d \leq x \\ E_y(x) = B e^{\alpha x}, & -d \geq x \end{cases} \quad (39)$$

$$k_1 = \sqrt{\omega^2 \mu \epsilon_1 - \beta^2}, \quad \alpha = \sqrt{\beta^2 - \omega^2 \mu \epsilon_2}, \quad A, B: \text{constant}, \quad B = A e^{\alpha d} \cos(kd).$$

Equation 30 is the TE even mode (symmetric to the origins at the x-axis), and the wave is also symmetrical in the upper and lower cladding regions. The dispersion formula is

$$\tan(kd) = \sqrt{\left(\frac{V}{kd}\right)^2 - 1} \quad (40)$$

The TE odd mode is

$$\begin{cases} E_y(x) = A \sin(kx), & -d \leq x \leq d \\ E_y(x) = A \sin(kd) e^{\alpha(d-x)}, & d \leq x \\ E_y(x) = -A \sin(kd) e^{\alpha(d+x)}, & -d \geq x \end{cases} \quad (41)$$

$$\tan(kd) = -1 / \left[\sqrt{\left(\frac{V}{kd}\right)^2 - 1} \right]$$

The total number of modes is $Even + Odd = 2(V/\pi)$.

As for the TM mode, just start with the “even” mode,

$$\begin{cases} H_y(x) = A \cos(kx), & -d \leq x \leq d \\ H_y(x) = A \cos(kd) e^{\alpha(d-x)}, & d \leq x \\ H_y(x) = -A \cos(kd) e^{\alpha(d+x)}, & -d \geq x \end{cases} \quad (42)$$

we can have the same result if we just interchange the H with the E and if different constant coefficients are used in the z components through the definitions in Equation 42.

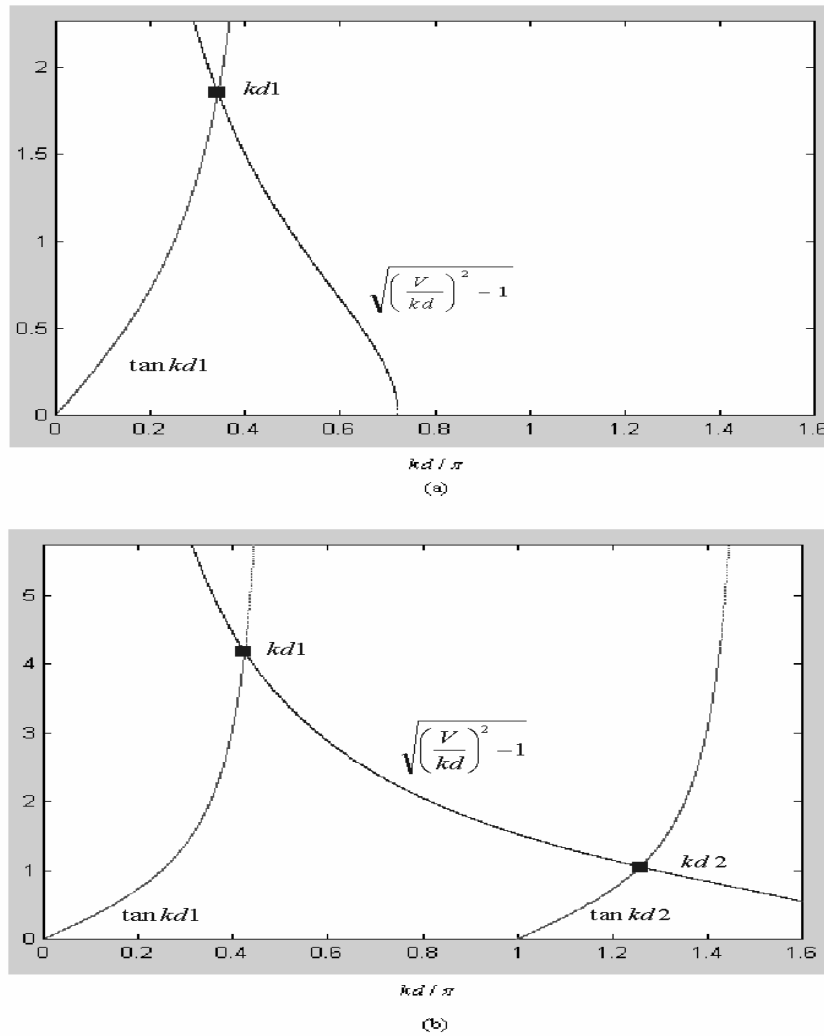


Figure 50. Matlab calculations and plots of TE even mode dispersion curves of (a) silica and (b) silicon materials

The results calculated and plot by Matlab in Fig. 50 derive from the dispersion relationship in Equation 31. The specifications are $d = 0.5 \mu\text{m}$, $n_2 = 1$, $n_1 = 3$ for the silicon core and $n_1 = 1.5$ for the silica core. The comparison in Fig. 50 establishes that the silicon core can support more mode propagations in the same core size. In Figs. 51 and 52, we plot (a) the first TE even mode in the silica core region and (b) two TE even modes in the silicon core region. The greatest difference is that the first mode is more well-confined in the silicon core region.

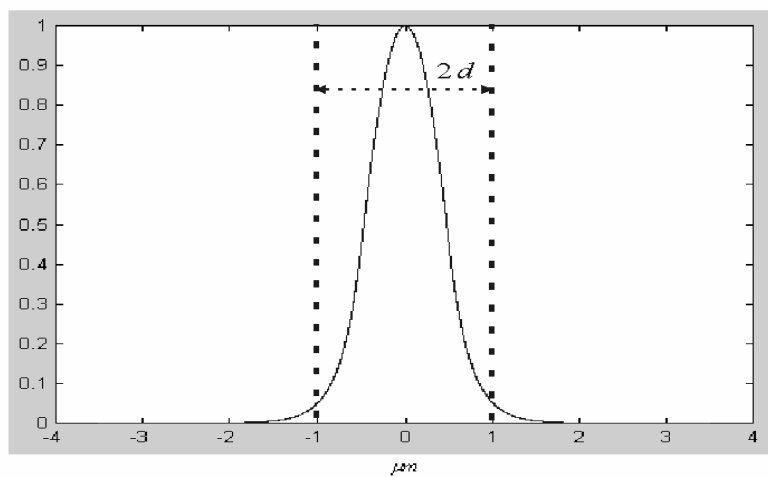


Figure 51. Matlab calculations an plot of TE even mode field distribution in the silica material

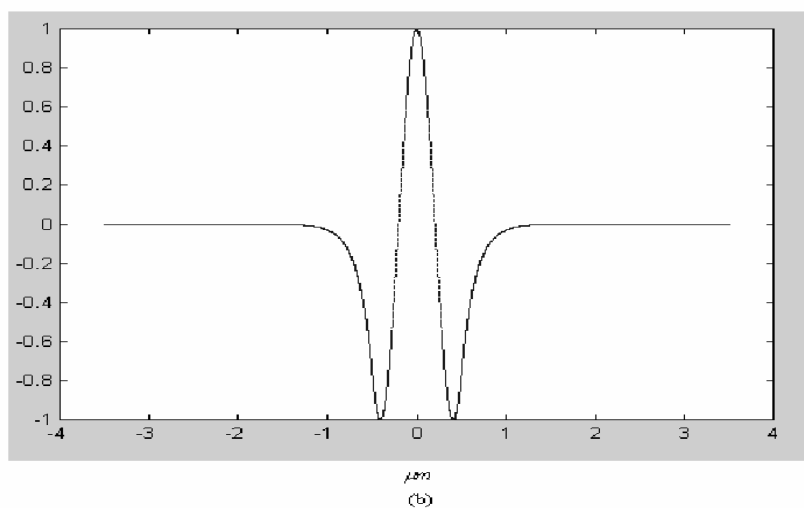
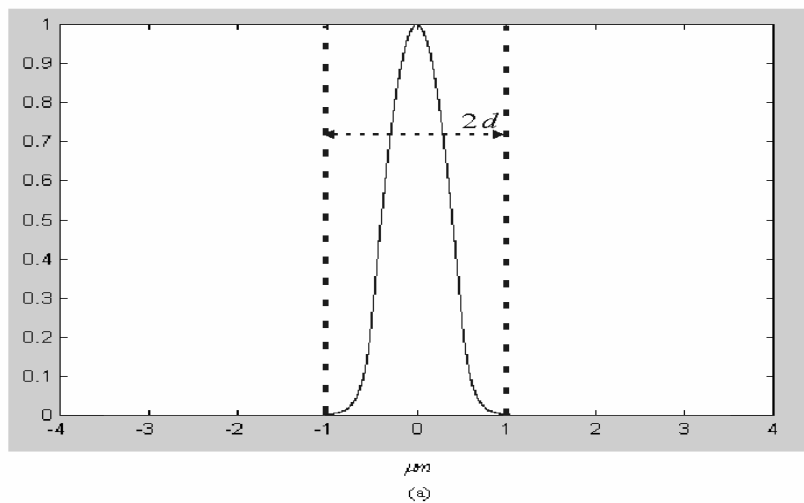


Figure 52. Matlab calculations and plots of TE even mode electric field distributions in the silicon material

Except for the wave equations for the 2-D slab waveguide, the last thing to be determined is the constant A .

The TE mode is

$$P = \frac{\beta}{2\omega\mu_0} \int_{-\infty}^{\infty} |E_y|^2 dx \quad (43)$$

$$\tau = \sigma \cdot d, \quad \psi = \delta \cdot d, \quad \sigma = \sqrt{\beta^2 - k^2 n_{cladding}^2}, \quad \delta = \sqrt{\beta^2 - k^2 n_{core}^2}$$

Therefore, $A = \sqrt{\frac{2\omega\mu P}{\beta d(1 + \frac{1}{2\tau} + \frac{1}{2\psi})}}$, and the same definition for the TM mode is

$$P = \frac{\beta}{2\omega\epsilon_0} \int_{-\infty}^{\infty} \frac{1}{n^2} |H_y|^2 dx \quad (44)$$

The refractive indexes of the core and the cladding are different from the corresponding indexes in the experiments because of the 2-D wafer definition in the simulation method in the later chapter. In Fig. 47, the silicon wafer and the upper cladding will be shown (or considered) only in 3-D simulation; however, it would take several days to complete the example already treated in Fig. 48 or Fig. 50. The air setting for the lower cladding ($n=1$) is set to be the same as the air setting for the upper cladding (in the 2-D simulation), and this scheme still leads to the equivalent SOI structure. The core refractive index of 3 and the cladding index of 1 still maintain the relative difference of 45% by the calculation of Equation 32. We choose a silica index of 1.5 to be simply compared to the high value of the SOI in order to discuss the impacts caused only by the change of the refractive index.

As shown in the Fig. 53 [28], both a simple SOI waveguide and a comparison of the fabrication size of the silica waveguide or CMOS are presented. The buried oxide layer is produced by the implanting of high-energy oxygen ions into *Si* and then by the annealing at a high temperature for several hours. The later epitaxial *Si* layer is grown by the Chemical Vapor Deposition (CVD). The sample endface has to be cleaved and polished so that the testing light can focus into the core region.

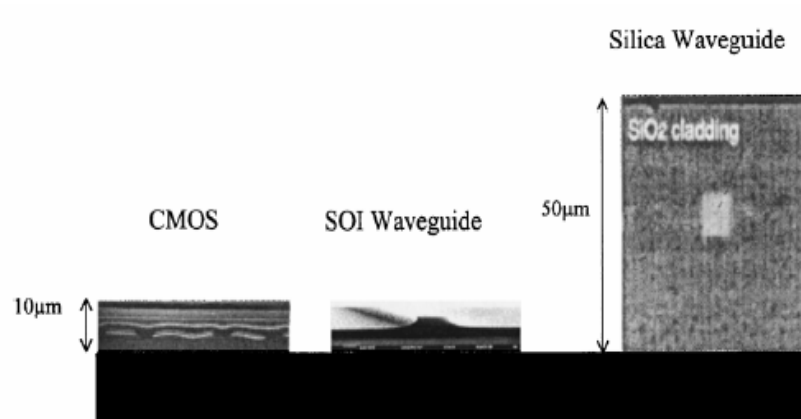


Figure 53. Comparison of fabricated SOI waveguide and other silicon applications [27]

3.3 Finite difference time domain method

The simulation code used in this research is based on the Finite Difference Time Domain (FDTD) scheme [29] derived from Equation 25. The six sub-equations in the rectangular system as shown in Fig. 54 are

$$\frac{\partial E_x}{\partial t} = \frac{1}{\varepsilon} \left(\frac{\partial H_z}{\partial y} - \frac{\partial H_y}{\partial z} \right), \quad \frac{\partial E_y}{\partial t} = \frac{1}{\varepsilon} \left(\frac{\partial H_x}{\partial z} - \frac{\partial H_z}{\partial x} \right), \quad \frac{\partial E_z}{\partial t} = \frac{1}{\varepsilon} \left(\frac{\partial H_y}{\partial x} - \frac{\partial H_x}{\partial y} \right) \quad (45)$$

$$\frac{\partial H_x}{\partial t} = -\frac{1}{\mu} \left(\frac{\partial E_z}{\partial y} - \frac{\partial E_y}{\partial z} \right), \quad \frac{\partial H_y}{\partial t} = -\frac{1}{\mu} \left(\frac{\partial E_x}{\partial z} - \frac{\partial E_z}{\partial x} \right), \quad \frac{\partial H_z}{\partial t} = -\frac{1}{\mu} \left(\frac{\partial E_y}{\partial x} - \frac{\partial E_x}{\partial y} \right)$$

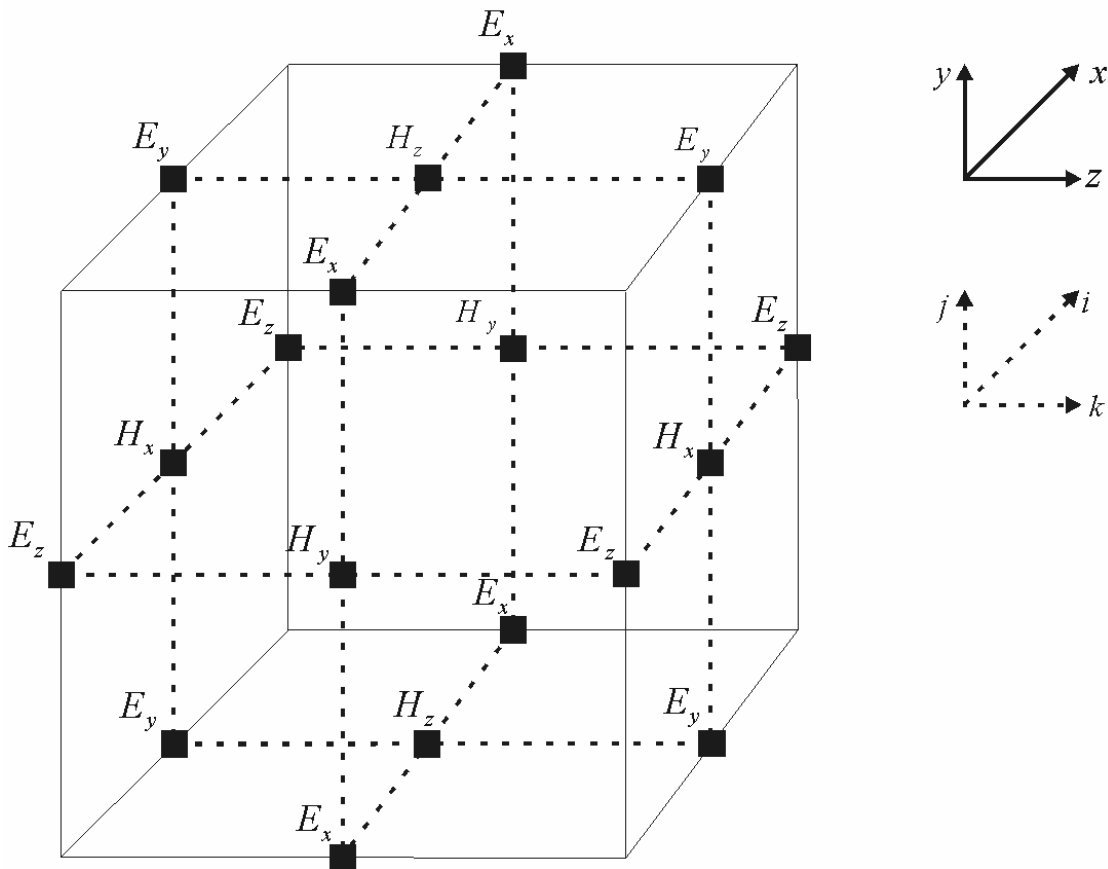


Figure 54. 3-dimensional FDTD cell

The $x - y - z$ axis constitutes the physical mesh coordinates, and $i - j - k$ constitutes the FDTD calculation step indices.

Take the first sub-equation $\frac{\partial E_x}{\partial t} = \frac{1}{\varepsilon} \left(\frac{\partial H_z}{\partial y} - \frac{\partial H_y}{\partial z} \right)$ for example. Here, the FDTD

representation based on Yee's algorithm [30] is

$$\begin{aligned} & \frac{E_x^{n+1/2}(i, j + \frac{1}{2}, k + \frac{1}{2}) - E_x^{n-1/2}(i, j + \frac{1}{2}, k + \frac{1}{2})}{\Delta t} \\ &= \frac{1}{\varepsilon} \left(\frac{H_z^n(i, j + 1, k + \frac{1}{2}) - H_z^n(i, j, k + \frac{1}{2})}{\Delta y} - \frac{H_y^n(i, j + \frac{1}{2}, k + 1) - H_y^n(i, j + \frac{1}{2}, k)}{\Delta z} \right) \end{aligned} \quad (46)$$

The required 3-dimensional computational stability is

$$\sqrt{(\Delta x)^2 + (\Delta y)^2 + (\Delta z)^2} > c\Delta t \quad (47)$$

For a 2-dimensional FDTD calculation, assume $\frac{\partial}{\partial y} = 0$ as shown in Equation 45; the

TE and the TM modes are then distinguished as

TE Mode:

$$\frac{\partial E_y}{\partial t} = \frac{1}{\varepsilon} \left(\frac{\partial H_x}{\partial z} - \frac{\partial H_z}{\partial x} \right), \quad \frac{\partial H_x}{\partial t} = \frac{1}{\mu_0} \frac{\partial E_y}{\partial z}, \quad \frac{\partial H_z}{\partial t} = -\frac{1}{\mu_0} \frac{\partial E_y}{\partial x} \quad (48)$$

TM Mode:

$$\frac{\partial H_y}{\partial t} = \frac{1}{\varepsilon} \left(\frac{\partial E_x}{\partial z} - \frac{\partial E_z}{\partial x} \right), \quad \frac{\partial E_x}{\partial t} = \frac{1}{\mu_0} \frac{\partial H_y}{\partial z}, \quad \frac{\partial E_z}{\partial t} = -\frac{1}{\mu_0} \frac{\partial H_y}{\partial x} \quad (49)$$

By the same discrete derivation, the 2-dimensional TE mode becomes

$$\begin{aligned}
 E_y^n(i, k) &= E_y^{n-1}(i, k) + \frac{\Delta t}{\varepsilon \Delta z} [H_x^{n-1/2}(i, k+1/2) - H_x^{n-1/2}(i, k-1/2)] \\
 &\quad - \frac{\Delta t}{\varepsilon \Delta x} [H_z^{n-1/2}(i+1/2, k) - H_z^{n-1/2}(i-1/2, k)] \\
 H_x^{n+1/2}(i, k+1/2) &= H_x^{n-1/2}(i, k+1/2) \\
 &\quad + \frac{\Delta t}{\mu_0 \Delta z} [E_y^n(i, k+1) - E_y^n(i, k)] \\
 H_z^{n+1/2}(i+1/2, k) &= H_x^{n-1/2}(i+1/2, k) \\
 &\quad - \frac{\Delta t}{\mu_0 \Delta x} [E_y^n(i+1, k) - E_y^n(i, k)]
 \end{aligned} \tag{50}$$

The computational stability limit is

$$\sqrt{(\Delta x)^2 + (\Delta z)^2} > c \Delta t \tag{51}$$

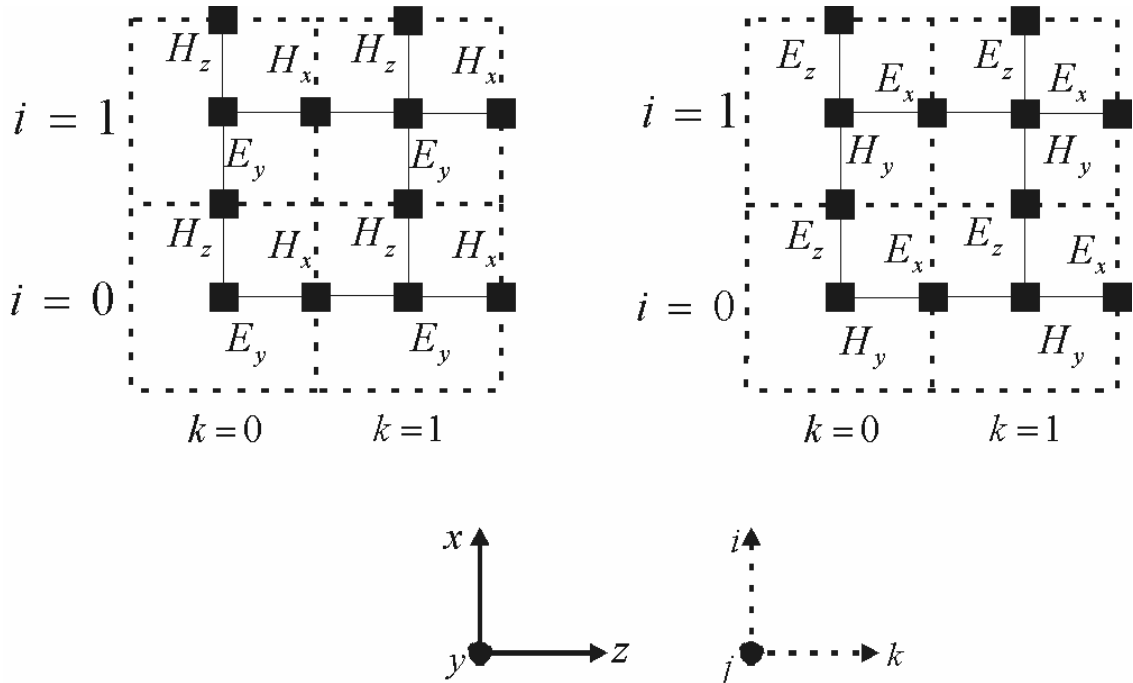


Figure 55. 2-dimensional FDTD cells in the TE and the TM modes

The sub-wavelength mesh size ΔL ($x = i \cdot \Delta L, z = k \cdot \Delta L$) of the FDTD is chosen as $\Delta L = \lambda / (10 \cdot n) = 0.05 \mu m$, $\lambda = 1.55 \mu m$, $n = 3$: the constant refractive index defined for the rest of this research. The definition of the Poynting vector (the TE mode) is

$$\begin{aligned} S &= 0.5 \cdot \text{Re}(E \times H^*) \\ S_z &= 0.5 \cdot \text{Re}(E_y \cdot H_x^*) \\ &= -0.5 \cdot (\text{Re}(E_y) \cdot \text{Re}(H_x) + \text{Im}(E_y) \cdot \text{Im}(H_x)) \end{aligned} \quad (52)$$

E, H : TE mode, the stationary value calculated by Discrete Fourier Transform (DFT)

[2].

$\text{Re}(E, H)$: real part of the electric and magnetic components.

$\text{Im}(E, H)$: imaginary part of the electric and magnetic components.

The real part of S_z is considered to be the desired propagating power density in this research.

Chapter 4. Research objectives

In this chapter, the research objectives will be defined based on the requirements and basic operations in chapter 1-3. The objectives are focused on the spatial filter and collection optics of the all-optical ADC, also to investigate the theoretical details in these devices; the results and findings will be able to improve the transmission efficiency of the all-optical ADC.

At the beginning of this chapter, the research objectives are:

1. Investigate the design methods and existing fabrication processes for the spatial filter with the goal of understanding the operations of the device.
2. Investigate the design method and existing fabrication processes for the collection optics with the goal of understanding the operations of the device.
3. Define the analytical parameters and specifications for both of the spatial filter and collection optics.
4. Analyze the optical transmission efficiency and crosstalk ratio of the spatial filter array.
5. Investigate and optimize optical collection optics transmission efficiency.
6. Develop the analytical modeling method in order to calculate the transmission efficiency of the spatial filter.

4.1 Components of the spatial optical pulse collection system

The basic geometry of the spatial optical pulse collection system will be presented in this section. The introduction will also illustrate the existing fabrication schemes prepared for the designs. Figure 56 illustrates the basic structure of a single spatial filter aperture that is composed of two parts: an aperture mask and a straight optical waveguide. The aperture mask is a widely used component in next-generation nano-optical storage [31] and is also enabled in parallel nano-optical write-in and read-out methods. In the application of the all-optical ADC, we have made modifications and combined designs in [32] and [33].

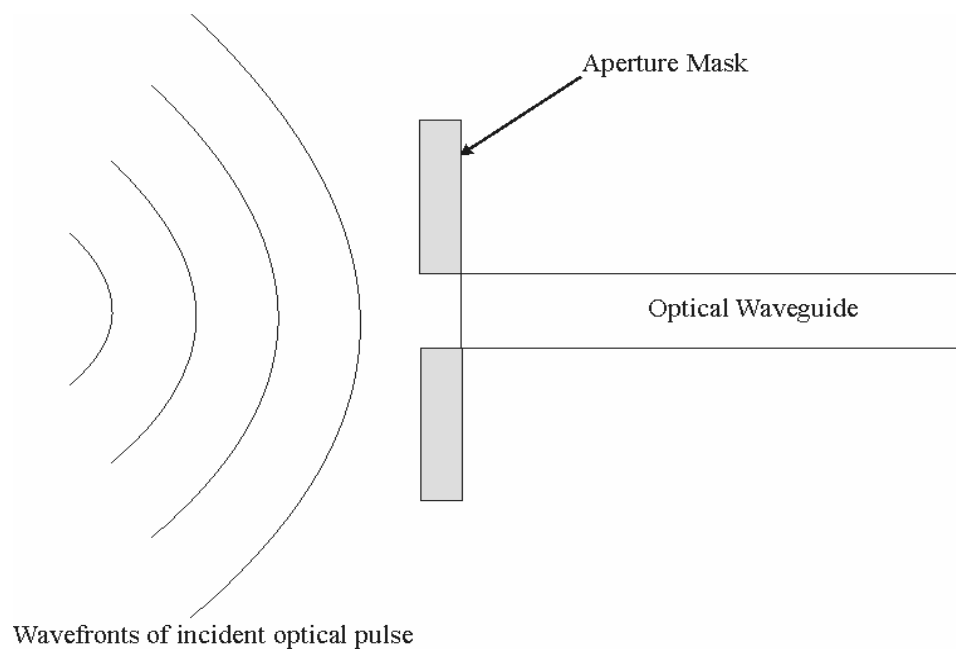


Figure 56. Single spatial filter

As shown in Fig. 56, the optical pulse strikes the surface of the aperture mask and partially transmits through the optical waveguide. In this basic illustration, there are two design considerations: (1) optical pulse width versus filter array dimension and (2) aperture geometry.

Figure 57 illustrates two different designs of the spatial filter. The first design is based on tapered conic geometry, and the second one is a basic square shape.

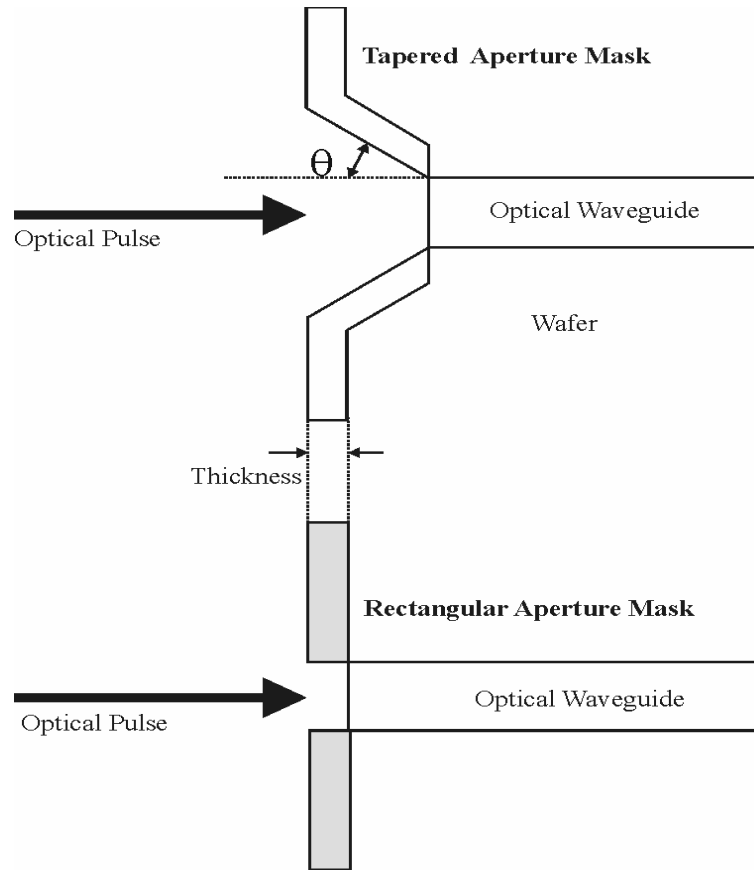


Figure 57. Tapered and square spatial filter

The discussion of both the design conclusion and the simulations will be devoted to the later chapters; here, consider functional effects in the spatial filter: (1) optical transmission and (2) frequency response.

The transmission ratio will affect the overall system performance, because the active amplifier has to be excluded, as much as possible, in the analog-to-digital conversion platform. We need to control the transmission and the coupling loss at each stage, or the accumulated loss will enable a significant percentage loss at the final output.

Also, in the beginning stage, the frequency characteristics have to be preserved, since the photodetector array will identify the signal by the center wavelength (center frequency) distribution.

In Fig. 58, the pulse width will be larger than the aperture mask, and the partial optical power will pass through the adjacent waveguide, as well as through the main input. Therefore, the pulse propagation in this circumstance will be investigated to define crosstalk between adjacent waveguides.

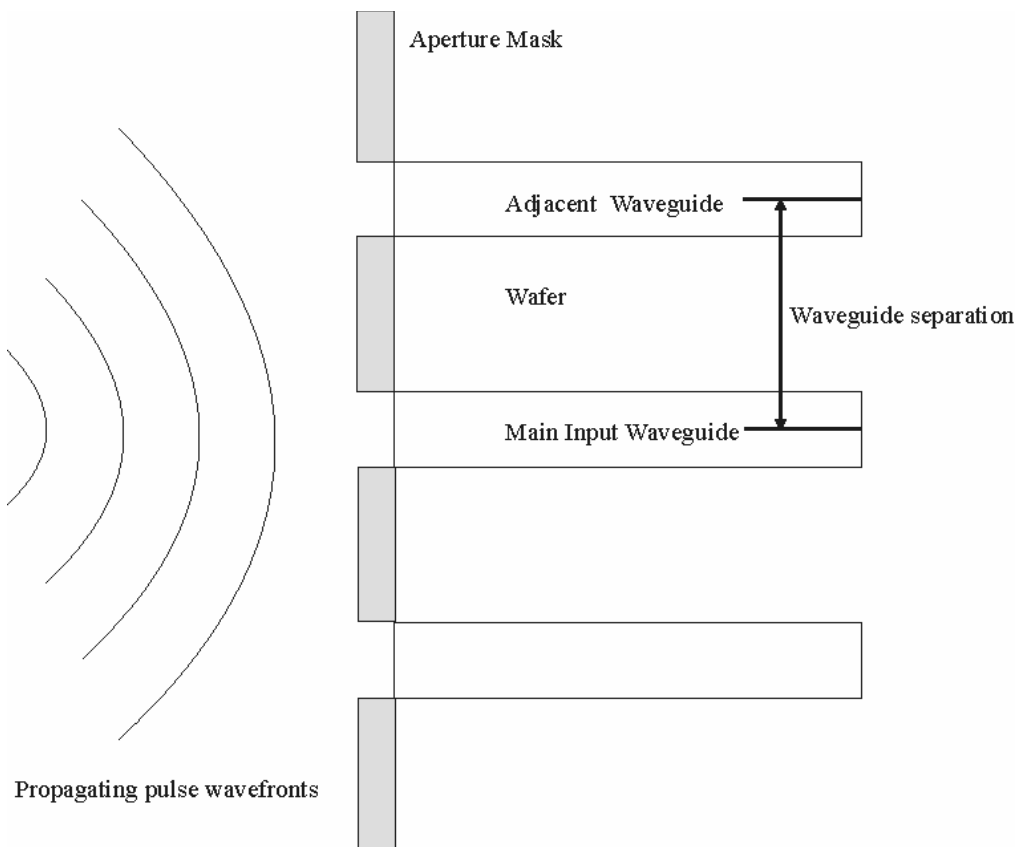


Figure 58. Spatial filter array

As shown in Fig. 59, the chosen existing fabrication scheme of the aperture mask array can make a single aperture size of 150 nm. The aperture array is fabricated on the basis of the SOI technique; the tapered geometry is generated by photolithography and wet etching methods. The optical transmissions of the probes in Fig. 59 are, both, about 14%.

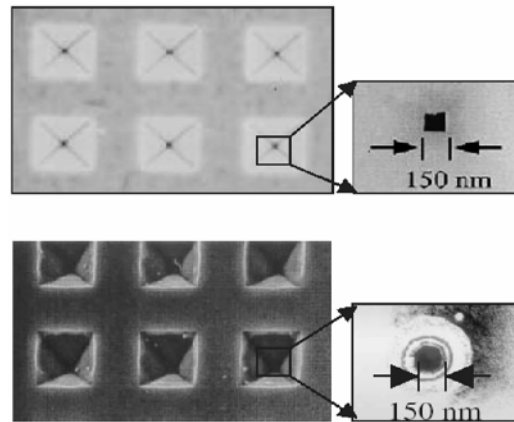


Figure 59. Fabricated near field aperture array [34].

On the basis of the available near-field aperture array measurements [34], the width of the spatial filter is estimated to be larger than the width of the example in Fig. 59, so that the transmission ratio can be enhanced. First, we need to find out the relationship of the half apex degree θ versus the transmission ratio in the design procedures. Second, the optical waveguide separation depends also on the filter array specification, and the coupling problem (crosstalk, adjacent-to-main input optical power ratio) will be considered for the design criterion. The design considerations are summarized as follows:

1. Optical pulse dispersion
2. Transmission ratio
3. Input optical waveguide separation

For the tapered waveguide, the purpose is to transmit an optical signal to the next stage of the integrated photodetector. The design, as shown in Fig. 60, is based on the large dimensional multiple-to-one tapered waveguide and is different from the tree structure waveguide. In the tree structure waveguide, a large portion of the branch loss will be introduced once the multi-stage is expected; the simulation will also be presented in the later chapters.

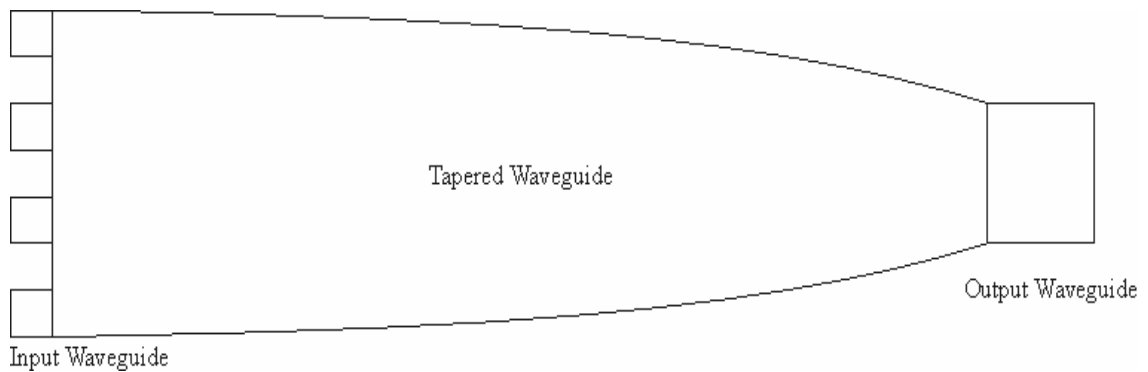


Figure 60. Tapered waveguide

The tapered waveguide is also widely used in spot-size conversion to be coupled with either output fiber ports or the wavelength dividing multiple accessing devices. Also, the tapered waveguide can be used as an N by N or 1 by N power splitter [35].

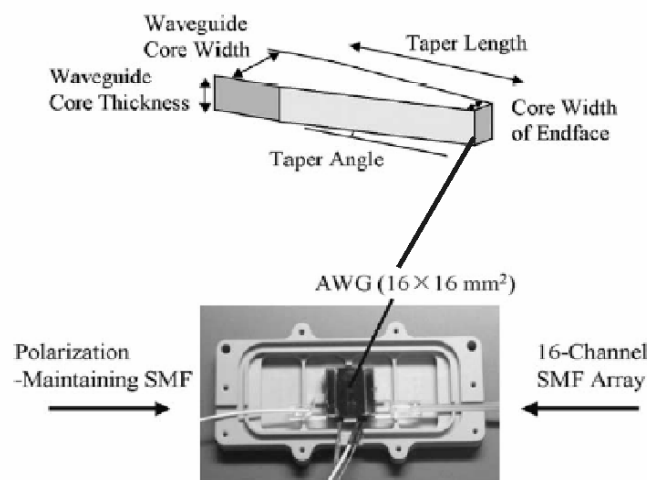


Figure 61. Tapered waveguide in application of wavelength multiplexing chip [35].

Figure 61 is an example of a fabricated wavelength multiplexor, and the tapered waveguide is used as a spot-size converter. The tapered waveguide is 2mm long and has a width of $4.5\mu\text{m}$ -to- $1.5\mu\text{m}$, a tapered angle of 3×10^{-3} rads, and a core thickness of 2mm.

The design criteria of the optical waveguide are summarized as follows

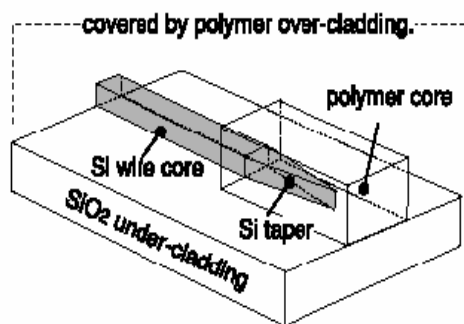
1. Low loss in the $1.55\mu\text{m}$ wavelength
2. Condensed circuitry
3. Fabrication compatible with near-field spatial filter array
4. Stacked optical waveguide structure

The Silicon-On-Insulator and the Separation IMplanted by the OXYgen (SOI-SIMOX) waveguide structure [36,37] are chosen for the waveguide implementation, and Fig. 62 shows the fabricated waveguide example.

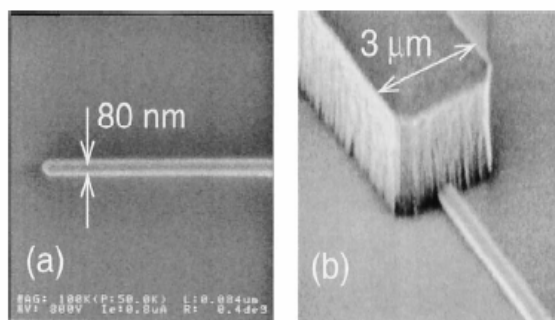


Figure 62. Optical waveguide by SOI method [37].

Also as shown in Fig. 63, a large polymer core with an SOI waveguide is used for the fiber coupling purpose. The SOI tapered waveguide is $200\mu\text{m}$ long and has a width of 200 nm-to-100 nm, and a core dimension of 400 by 200nm.



Schematic of mode field size converter.



Scanning electron micrographs of mode field size converter.

Figure 63. Silicon waveguide and output coupling example [37].

4.2 Limitations

The 2-dimensional FDTD method of the TE mode is used, here, for a preliminary examination of the spatial optical pulse collection system. The proposed objective of this theoretical analysis will be introduced in the next section. This section covers the demonstration of, and the discussion of, the separate simulations of spatial filters and tapered waveguide. Also, this section treats the results related to the design criteria.

1. Spatial filter array

For the spatial filter simulation as shown in Fig. 64, Gallium Phosphide (GaP) ($n = 3.05$) [32] was used as the aperture material. The simulation was based on the assumption that the optical pulse would incident into the waveguide through the spatial filter without any tilting angle (properly deflected as desired); however, the Full Width Half Maximum (FWHM) of the incident pulse to the waveguide width is 2-to-1. The tapered geometry θ (half apex angle) of 30° is used.

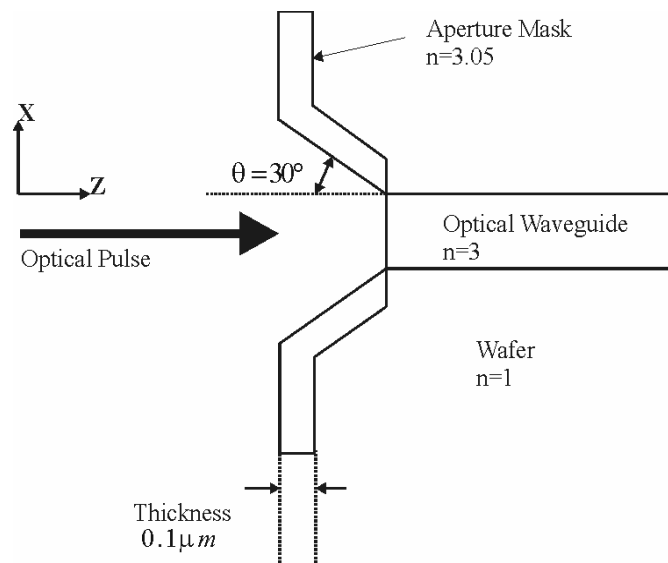


Figure 64. Tapered spatial filter

Figure 65 is a simulation example of the single spatial filter. The simulation example shows that the optical pulse is collected through the tapered structure and also blocks unwanted portion; therefore, no optical pulse passes behind the aperture mask.

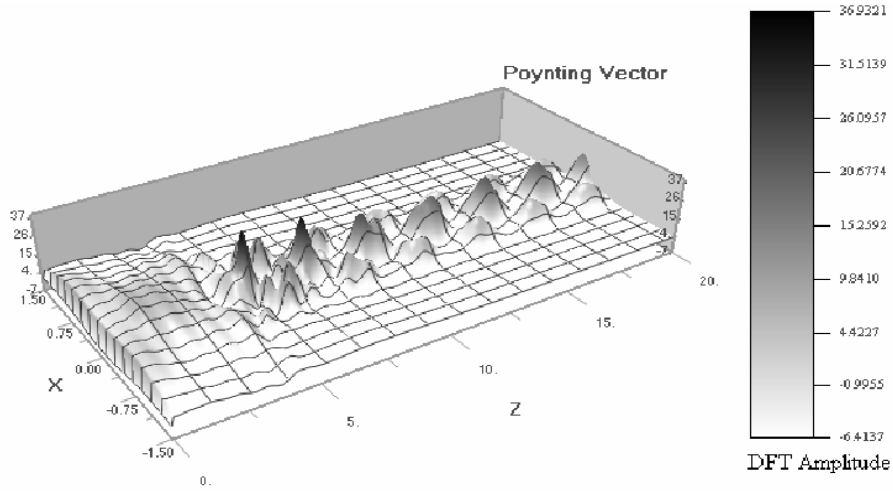


Figure 65. FDTD simulation example of tapered spatial filter

The next example to be demonstrated is the spatial filter array simulation. The purpose underlying the simulation is to calculate the crosstalk (cross-coupling) effect caused by the incident optical pulse that was covering two or more input waveguides.

The definition of the crosstalk ratio based on the measurement line in Fig. 66 is

$$\begin{aligned} \text{Main input power ratio: } & \frac{P(A)}{P(B)} \\ \text{Crosstalk power ratio: } & \frac{P(C)}{P(B)} \end{aligned} \quad (53)$$

Figure 66 illustrates the spatial filter array simulation layout. The waveguide center-to-center distance is $2\mu\text{m}$, and the waveguide width is $1\mu\text{m}$. Positions A, B, and C constitute the Poynting vector (z-direction optical power defined in Equation 52) line respectively.

Different deflection angles (the deflected optical pulse from the electro-optical deflector) are assumed in the FDTD simulations.

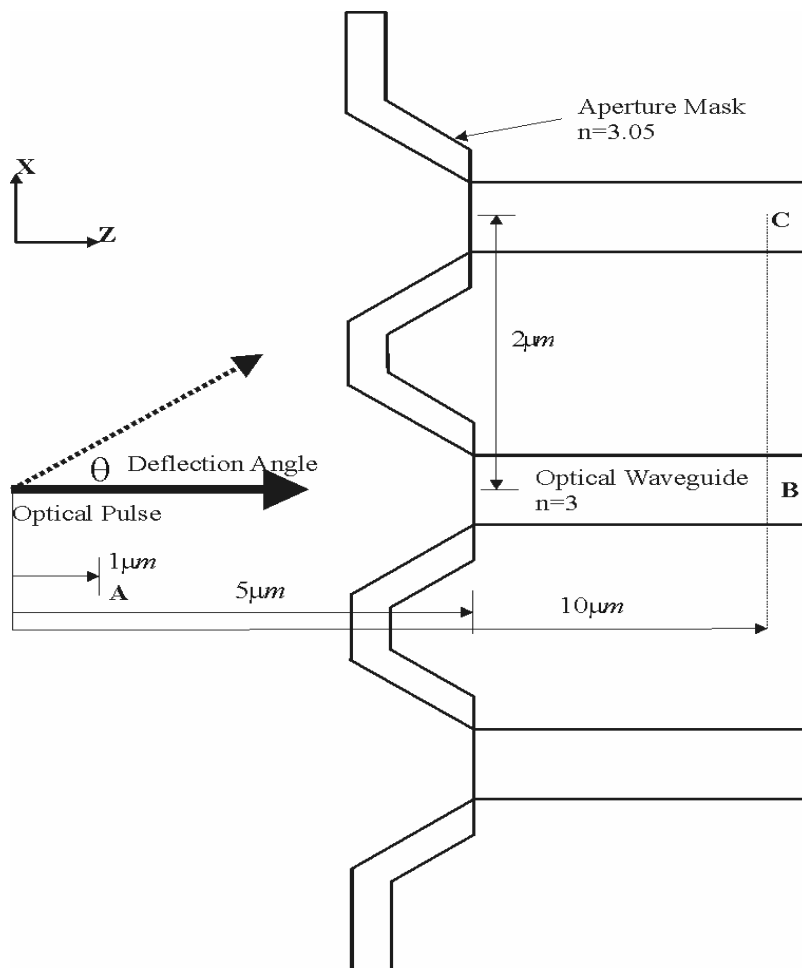


Figure 66. Spatial filter array

Figure 67 is an example of a 5° angle of deflection. The optical pulse strikes the spatial filter and is blocked by the aperture mask; however, some of the optical pulses still pass through the optical waveguide.

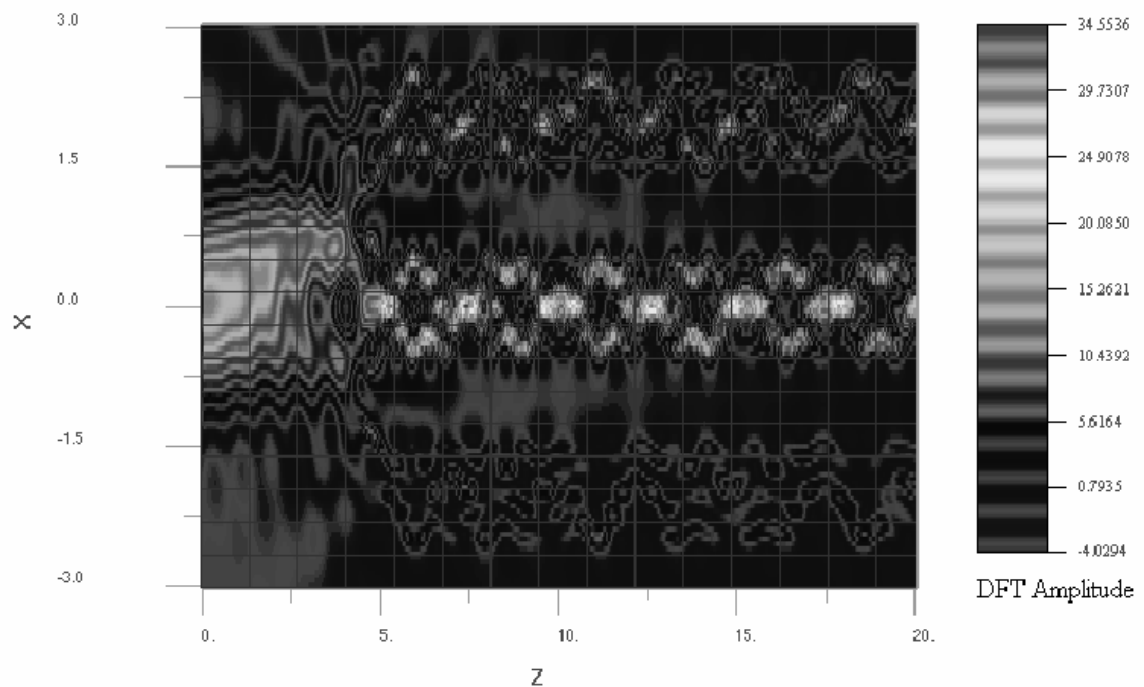


Figure 67. FDTD simulation example of 5-degree deflection angle

Figure 68 is the calculated transmission and crosstalk ratio defined in Equation 53. The main input transmission ratio simply refers to the collected optical pulse; however, the crosstalk ratio describes every analog-to-digital conversion per 12° that is needed.

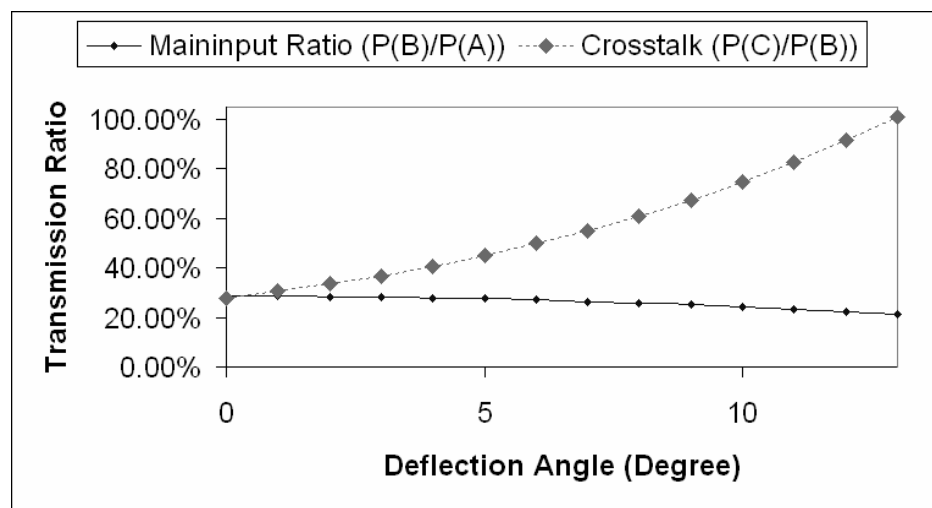


Figure 68. Transmission ratio of tapered spatial filter array by various deflection angles

2. Tapered waveguide

Figure 69 illustrates the design of the tapered waveguide layout. In order to reduce the device length, we applied twice the tapered angle as in [38]. The exponentially tapered function is defined as

$$X = e^{\left[\frac{\alpha \cdot Z}{L1}\right]} - 1, \quad \alpha = 3 \quad (54)$$

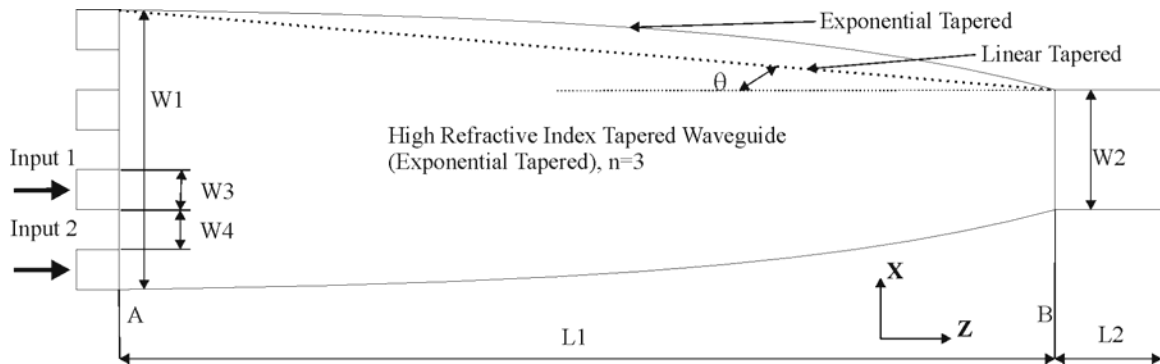


Figure 69. Specifications for tapered optical waveguide

As shown in Fig. 70, we calculated the transmission ratios of the tapered waveguide for the lower half branches (because of the symmetry) in different scaling factors $\left(\frac{W1}{W2}\right)$, and the length is fixed at $L1 = 78 \mu m, W3 = W4 = 1 \mu m$. From the power ratio calculations in Fig. 70, the optimized scaling factor is 0.57 ($W1 = 7 \mu m, W2 = 4 \mu m$). The feature of this design shows the optical power confinement of the large dimensional optical waveguide, and no tilting angle of the input waveguide is required [39].

Figure 71 is the FDTD simulation example of the tapered waveguide. The optical pulse is deflected along the z-direction inside the tapered waveguide, and scattered to the output end.

Figure 70 records the simulation results of the optical transmission ratio versus the scaling factor. The transmission ratio shows that there is no significant enhancement since the scaling factor of 0.57, therefore, the factor of 0.57 is chosen as the optimized factor.

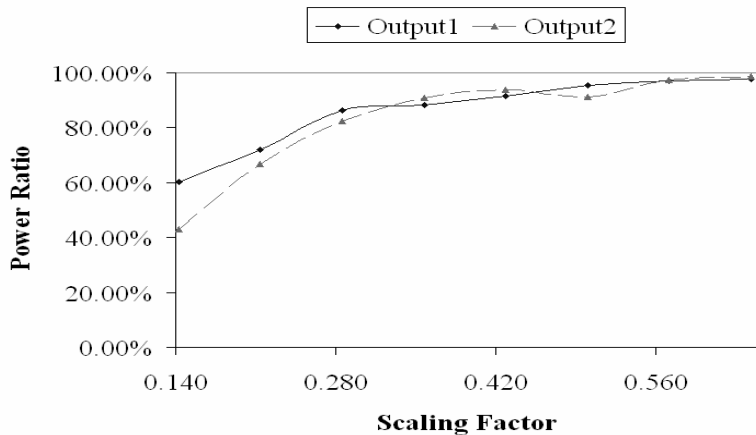


Figure 70. Power ratio ($P(B)/P(A)$) of different scaling factors

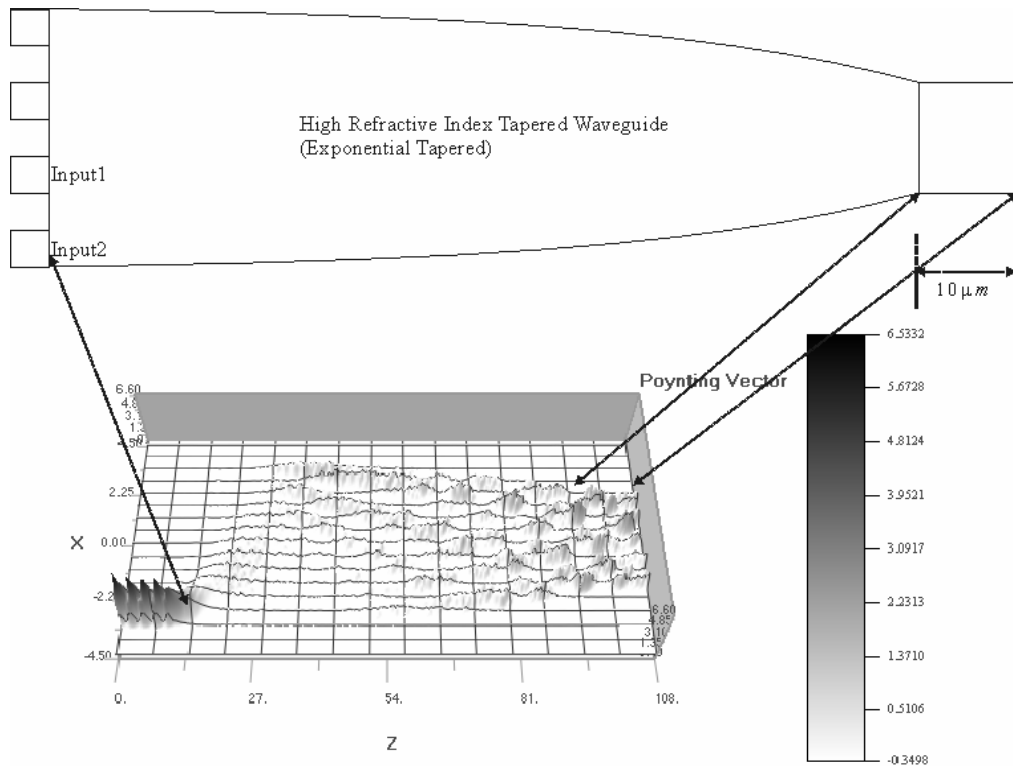


Figure 71. FDTD simulation example of tapered waveguide

4.3 Proposed research

As Fig. 72 illustrates, this research will investigate and analyze the transmission ratio of the spatial filter. The optical source is assumed to be an optical pulse whose deflection of angle is θ ; the pulse propagates to the spatial filter of the binary pattern, as shown in Fig. 26. The objective of this research is to introduce a systematic integration method for the applied techniques. The integration method can be further combined with the transmission characteristics introduced in the conclusion of this research; therefore, we can construct complete analytical model of the analog-to-digital converter.

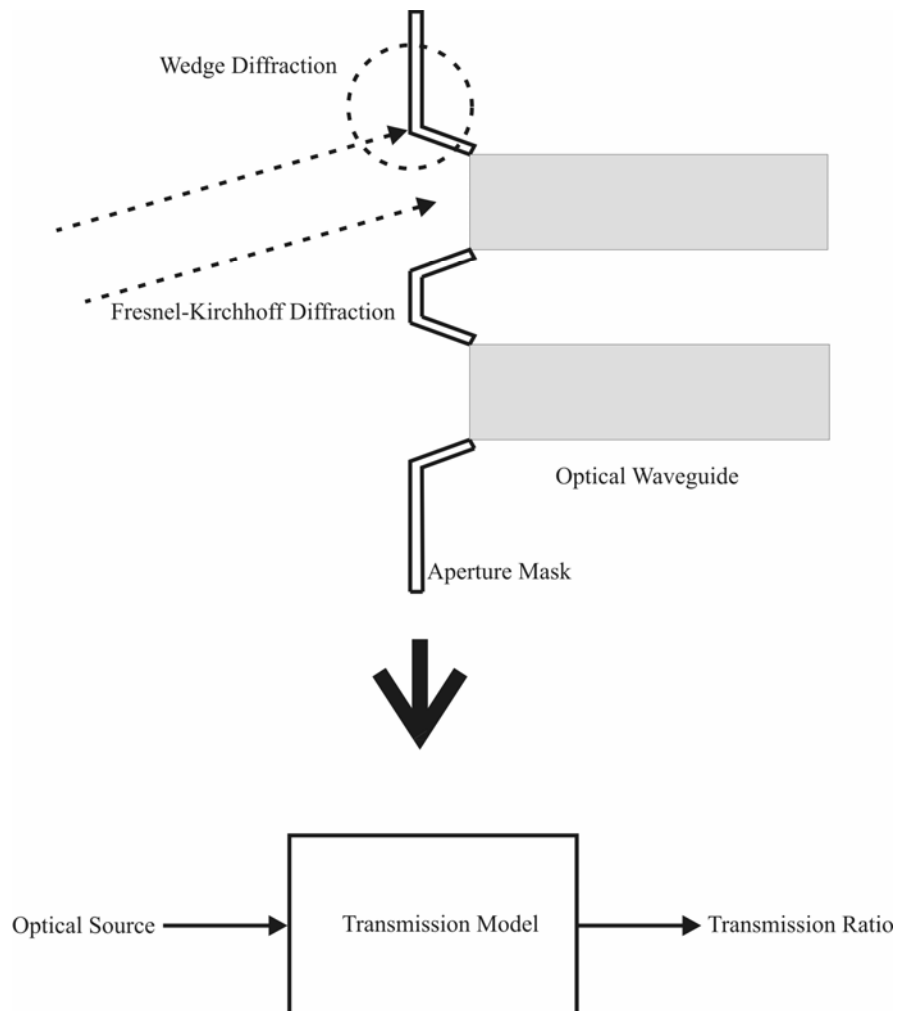


Figure 72. Illustration of the proposed research.

1. Fresnel-Kirchhoff diffraction:

Originally, researchers used the Fresnel-Kirchhoff diffraction to calculate the ratio of wave propagation through an aperture to a case without an aperture—that was, defined as the diffraction coefficient. In Chapter 5, I review the modification that is necessary for calculations pertaining to the transmission ratio of the wave propagation through the aperture and to the input wave.

2. Wedge diffraction

In this research, wedge diffraction describes the diffraction phenomena that result from the tapered-edge structure of the spatial filter.

3. Fresnel equations

The deflected optical pulse passes through the spatial filter and then collected by the high-refractive index optical waveguide. Fresnel equations are derived from Snell's law to calculate the final transmission ratio of the spatial filter.

Fresnel-Kirchhoff diffraction [40]:

Figure 73 illustrates both the basic structure of the diffracting aperture and the Fresnel-Kirchhoff diffraction. Also as illustrated in Fig. 73, the dimensional variables in the formation of the diffraction are given the following definitions:

$\psi(x, y, x)$: optical source

$\psi(x', y', x')$: optical wave at the observation point

s : vector from O to the optical source

r : vector from O to the observation point

O : chosen point at the aperture opening; any point at the opening

n : directional vector, normal to the surface of the aperture mask; positive z direction

(n, r) : angle of the vector r between n

(n, s) : angle of the vector s between n

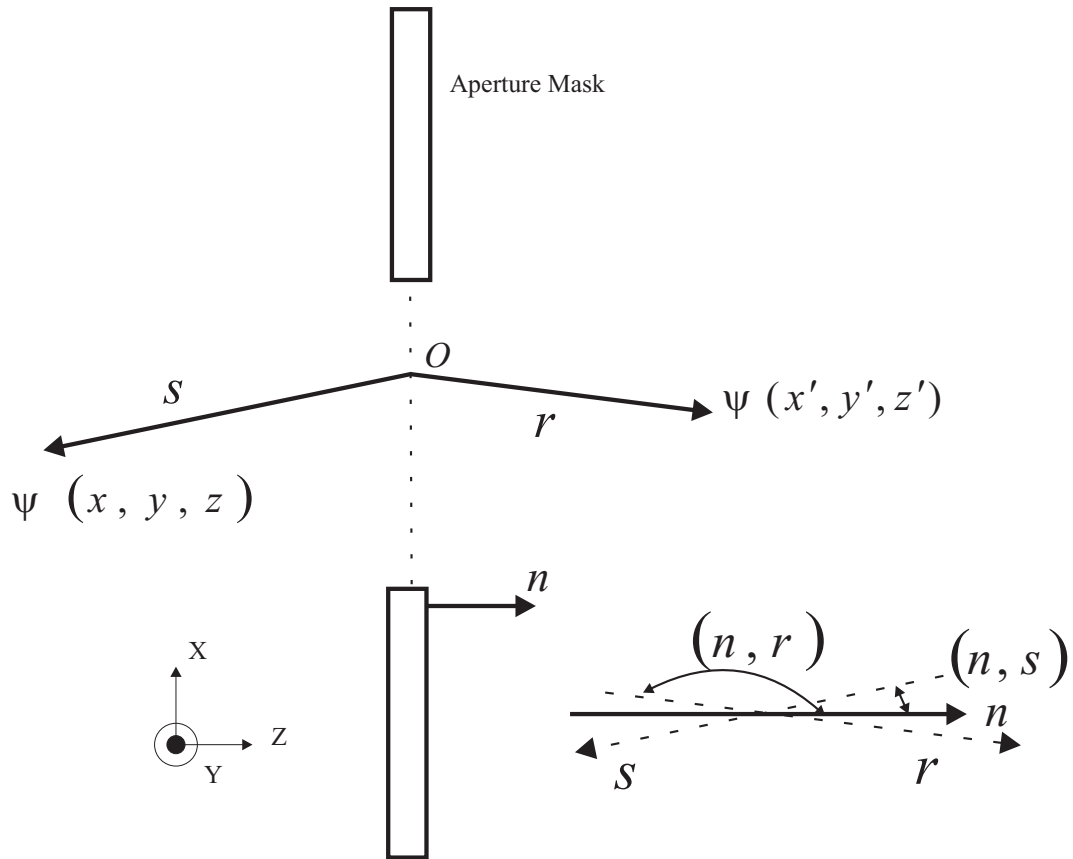


Figure 73. Diffracting aperture

The first step in the diffraction problem involves the Helmholtz equation [41]

$$\nabla^2 \psi + k^2 \psi = 0 \quad (55)$$

The monochromatic wave is defined in terms of

$$\psi(x, y, z, t) = \psi(x, y, z) e^{-j\omega t} \quad (56)$$

The solution to the wave equation makes use of Green's equation:

$$\nabla^2 G + k^2 G = \delta(r - r') \quad (57)$$

$$\delta(r - r') = \delta(x - x')\delta(y - y')\delta(z - z'), \quad G = G(x, y, z, x', y', z')$$

Therefore, the Helmholtz equation can be written as

$$\psi(x', y', z') = \int_S \left(\psi \frac{\partial G}{\partial n} - G \frac{\partial \psi}{\partial n} \right) dS \quad (58)$$

The choice of G for the diffraction problem in the single medium (single refractive index) can be expressed as

$$G = \frac{A}{4\pi} \frac{e^{-jkr}}{r}, \quad r = \sqrt{(x' - x)^2 + (y' - y)^2 + (z' - z)^2}, \quad A: \text{constant} \quad (59)$$

The wave equation becomes

$$\psi(x', y', z') = \frac{1}{4\pi} \int_S \left(\psi \frac{\partial}{\partial n} \frac{A \cdot e^{-jkr}}{r} - \frac{A \cdot e^{-jkr}}{r} \frac{\partial \psi}{\partial n} \right) dS \quad (60)$$

Let the spherical wave ψ of constant amplitude A be already propagated to the point O in Fig. 73, so that ψ is in the form of $\frac{A \cdot e^{-jks}}{s}$ (spherical wavefront). The term inside the

integral of Equation 60 can be written as

$$\frac{\partial \psi}{\partial n} = \frac{A \cdot e^{-jks}}{s} \left(jk + \frac{1}{s} \right) \cdot (n, s), \quad \frac{\partial}{\partial n} \frac{A \cdot e^{-jkr}}{r} = \frac{A \cdot e^{-jks}}{r} \left(jk + \frac{1}{r} \right) \cdot (n, r)$$

Assume $k \gg \frac{1}{s}$ or $\frac{1}{r}$; therefore, $\frac{1}{s^2}$ and $\frac{1}{r^2}$ are neglected. Equation 60 will be

$$\psi(x', y', z') = \frac{j \cdot k \cdot A}{4\pi \cdot s \cdot r} \cdot [(n, r) - (n, s)] \cdot \int_S e^{-jk(s+r)} dS \quad (61)$$

Equation 61 is the so-called Fresnel-Kirchhoff integral. It is used to calculate the diffraction coefficient, and the details of both the calculation and related examples will be shown in Chapter 5.

Wedge diffraction [24]:

The wedge diffraction starts from the cylindrical wave equation for the structure illustrated in Fig. 74:

$$\frac{\partial^2 \psi}{\partial \rho^2} + \frac{1}{\rho} \frac{\partial \psi}{\partial \rho} + \frac{1}{\rho^2} \frac{\partial^2 \psi}{\partial \phi^2} + \frac{\partial^2 \psi}{\partial z^2} = -\beta^2 \psi \quad (62)$$

The solution to the wave equation (traveling wave solution) is

$$\psi(\rho, \phi, z) = f(\rho)g(\phi)h(z) = [C_1 H_m^{(1)}(\beta_\rho \rho) + D_1 H_m^{(2)}(\beta_\rho \rho)] \cdot [C_2 \cos(m\phi) + D_2 \sin(m\phi)] \cdot [A_3 e^{-j\beta z} + B_3 e^{j\beta z}] \quad (63)$$

A , B , C , D : constant, β : phase constant, $H_m^{(1)}$: Hankel function of the first kind,

$H_m^{(2)}$: Hankel function of the second kind.

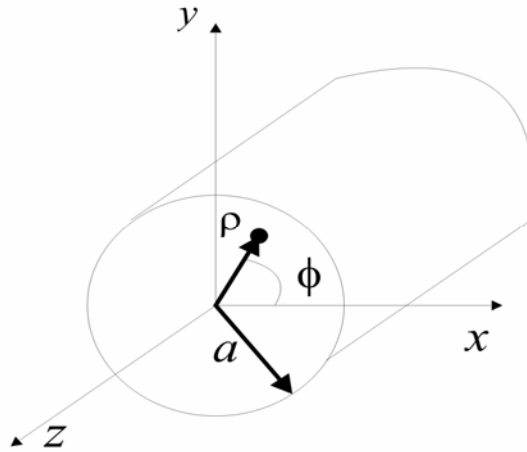


Figure 74. Cylindrical waveguide

For the following derivation, the TM mode and duality theorem are used to obtain the wave distribution of the wedge structure.

Assume there is a constant current source I_e ; therefore,

$$I_e(z') = \hat{a}_z I_e \quad (64)$$

The TM_z field that is radiated by the line source in the cylindrical coordinate system is

$$F = 0$$

$$A = \hat{a}_z A_z(\rho, \phi, z) = \hat{a}_z [C_1 H_m^{(1)}(\beta_\rho \rho) + D_1 H_m^{(2)}(\beta_\rho \rho)] \cdot [C_2 \cos(m\phi) + D_2 \sin(m\phi)] \cdot [A_3 e^{-j\beta_z z} + B_3 e^{j\beta_z z}] \quad (65)$$

H_m^p : Hankel function of p kind of order p. F : electric vector potential, A : magnetic vector potentials

The line source is of infinite length; the lower order is chosen as

$$\beta_z = 0 \Rightarrow \beta_\rho = \beta$$

The solutions become

$$A = \hat{a}_z A_z(\rho) = \hat{a}_z A_0 H_0^{(2)}(\beta\rho)$$

$$E_z = -j \frac{1}{\omega\mu\epsilon} \left(\frac{\partial^2}{\partial z^2} + \beta^2 \right) A_z = -j\omega A_0 H_0^{(2)}(\beta\rho) \quad (66)$$

$$H_\phi = -\frac{1}{\mu} \frac{\partial}{\partial \rho} A_z = A_0 \frac{\beta}{\mu} H_1^{(2)}(\beta\rho)$$

$$A_0 = -j \frac{\mu}{4} I_e$$

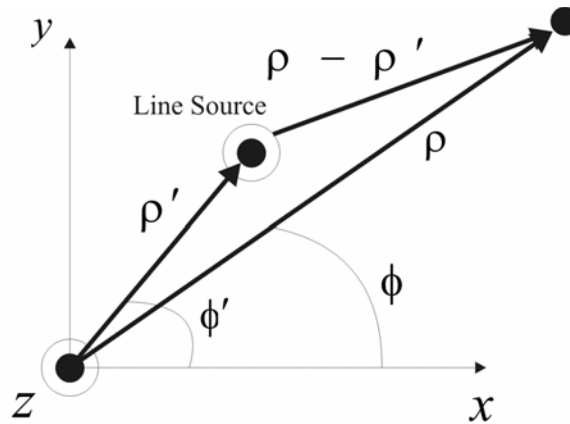


Figure 75. Line source being located away from the origin

The previous solutions will be transformed into the case that Fig. 75 illustrates. This transformation means that the current source is not located at the origin.

The solution as the source is placed away from the origin

$$E_z = -I_e \frac{\beta^2}{4\omega\epsilon} H_0^{(2)}(\beta|\rho - \rho'|) \quad (67)$$

$$H_\psi = -jI_e \frac{\beta}{4} H_1^{(2)}(\beta|\rho - \rho'|)$$

ψ : circumferential angle around the source

According to the duality theorem, the TE_z of the magnetic current source (I_m) will be

$$E_\psi = jI_m \frac{\beta}{4} H_1^{(2)}(\beta|\rho - \rho'|) \quad (68)$$

$$H_z = -I_m \frac{\beta^2}{4\omega\epsilon} H_0^{(2)}(\beta|\rho - \rho'|)$$

The field that is generated by the constant magnetic current (TE_z) is illustrated in Fig. 75

$$H_z^i = -\frac{\beta^2 I_m}{4\omega\epsilon} H_0^{(2)}(\beta|\rho - \rho'|) \quad (69)$$

The addition theorem for the Hankel function represents the source located away from the origin as shown in Fig. 75, and transforms the cylindrical wave functions originates at the origin. The addition theorem is

$$H_0^{(2)}(\beta|\rho - \rho'|) = \begin{cases} \sum_{n=-\infty}^{\infty} J_n(\beta\rho) H_n^{(2)}(\beta\rho') e^{jn(\phi-\phi')} & \rho \leq \rho' \\ \sum_{n=-\infty}^{\infty} J_n(\beta\rho') H_n^{(2)}(\beta\rho) e^{jn(\phi-\phi')} & \rho \geq \rho' \end{cases} \quad (70)$$

The transformed field is written as

$$H_z^i = -\frac{\beta^2 I_e}{4\omega\epsilon} \begin{cases} \sum_{n=-\infty}^{\infty} J_n(\beta\rho) H_n^{(2)}(\beta\rho') e^{jn(\phi-\phi')} & \rho \leq \rho' \\ \sum_{n=-\infty}^{\infty} J_n(\beta\rho') H_n^{(2)}(\beta\rho) e^{jn(\phi-\phi')} & \rho \geq \rho' \end{cases} \quad (71)$$

Figure 76 is the 3-dimensional view of the wedge structure. Through variations in the wedge angle, the total field can be used to represent the incident field distribution of the spatial filter structure. For example, $n = 1.31$ is a 125° wedge; in other words, the half-apex angle of the spatial filter is 35° .

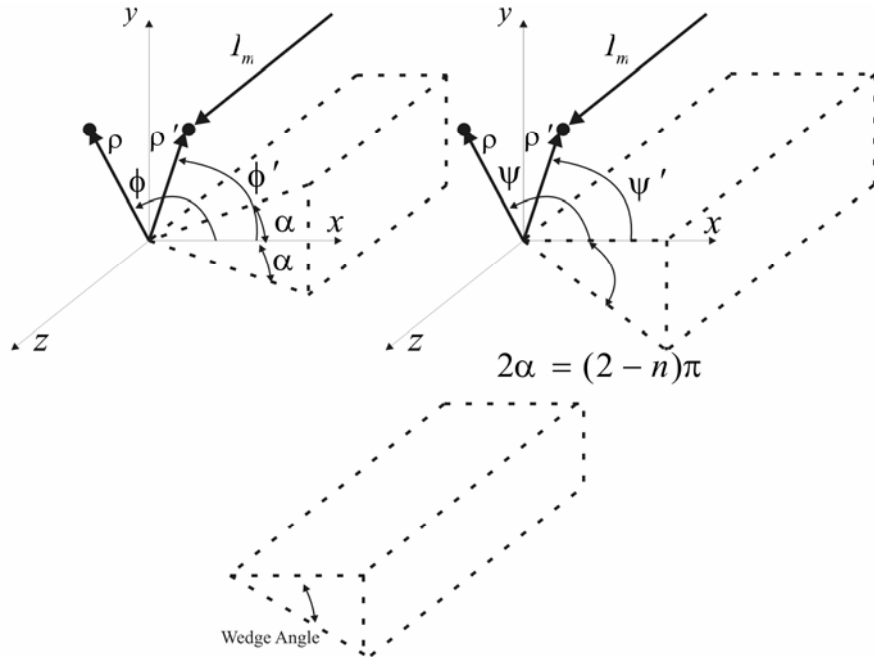


Figure 76. 3-D view of wedge scattering

The total field includes the incident field and the scattered field, both of which result from the wedge. The total field is defined as

$$H_z^t = H_z^i + H_z^s = \begin{cases} \sum_s b_s J_s(\beta\rho) H_s^2(\beta\rho') \cos[s(\phi' - \alpha)] \cos[s(\phi - \alpha)] & \rho \leq \rho' \\ \sum_s b_s J_s(\beta\rho') H_s^2(\beta\rho) \cos[s(\phi' - \alpha)] \cos[s(\phi - \alpha)] & \rho \geq \rho' \end{cases} \quad (72)$$

H_z^i : incident field, H_z^s : scattered field caused by the wedge

These variables are defined as

$$s = \frac{m\pi}{2(\pi - \alpha)}, m = 1, 2, 3, \dots \quad b_s = \varepsilon_s \frac{\pi\omega\mu I_m}{4(\pi - \alpha)}, \quad \varepsilon_s = \begin{cases} 1 & s = 0 \\ 2 & s \neq 0 \end{cases} \quad (73)$$

As shown in Fig. 76, we have

$$2\alpha = (2 - n)\pi \Rightarrow n = 2 - \frac{2\alpha}{\pi} \quad (74)$$

Therefore, $s = \frac{m}{n}, m = 1, 2, 3, \dots$

$$b_s = \frac{\omega\varepsilon I_m}{2} \frac{\varepsilon_s}{n}, \quad \phi' = \psi' + \alpha, \quad \phi = \psi + \alpha$$

$$\cos[s(\phi' - \alpha)]\cos[s(\phi - \alpha)] = \frac{1}{2} \left\{ \cos\left[\frac{m}{n}(\psi - \psi')\right] + \cos\left[\frac{m}{n}(\psi + \psi')\right] \right\} \quad (75)$$

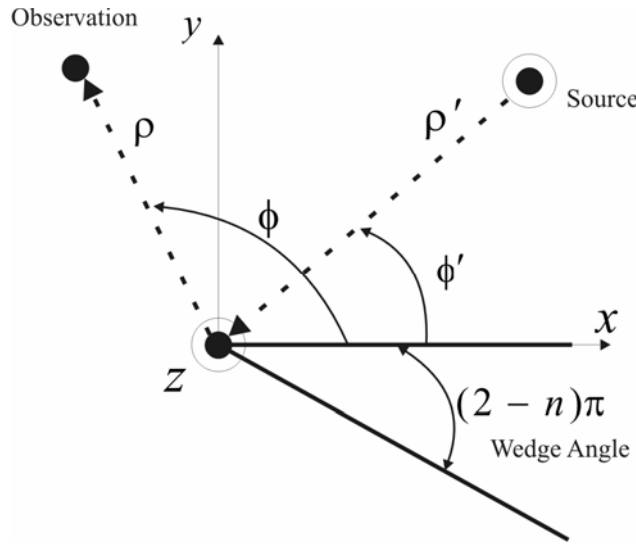


Figure 77. 2-D view of the wedge

The total field is re-written as

$$H_z^t = \frac{\omega \varepsilon I_m}{4} \frac{1}{n} \begin{cases} \sum_{m=0,1,\dots}^{\infty} \varepsilon_m J_{m/n}(\beta \rho) H_{m/n}^{(2)}(\beta \rho') \left\{ \cos \left[\frac{m}{n}(\psi - \psi') \right] + \cos \left[\frac{m}{n}(\psi + \psi') \right] \right\} & \rho \leq \rho' \\ \sum_{m=0,1,\dots}^{\infty} \varepsilon_m J_{m/n}(\beta \rho') H_{m/n}^{(2)}(\beta \rho) \left\{ \cos \left[\frac{m}{n}(\psi - \psi') \right] + \cos \left[\frac{m}{n}(\psi + \psi') \right] \right\} & \rho \geq \rho' \end{cases} \quad (76)$$

Equation 76 is the starting point for the wedge diffraction calculation that I not only explain in Chapter 5 but demonstrate with examples, as well.

Fresnel equations [25]:

Snell's law is described in Chapter 3-1 (Figures 45 and 46). The Fresnel equations continue to describe the transmission coefficients and the reflection coefficients. The Fresnel equations are defined as

$$\text{TE mode: } r = \frac{E_r}{E} = \frac{\cos \theta - \sqrt{n^2 - \sin^2 \theta}}{\cos \theta + \sqrt{n^2 - \sin^2 \theta}}, \quad t = \frac{E_t}{E} = \frac{2 \cos \theta}{\cos \theta + \sqrt{n^2 - \sin^2 \theta}} \quad (77)$$

$$\text{TM mode: } r = \frac{E_r}{E} = \frac{n^2 \cos \theta - \sqrt{n^2 - \sin^2 \theta}}{n^2 \cos \theta + \sqrt{n^2 - \sin^2 \theta}}, \quad t = \frac{E_t}{E} = \frac{2n \cos \theta}{n^2 \cos \theta + \sqrt{n^2 - \sin^2 \theta}}$$

$E' = E^r$, $E'' = E^t$, $n = \frac{n_2}{n_1}$: relative refractive index as illustrated in Figures 45 and 46.

Babinet's principle [42]:

In Chapter 5, I will use the concept of Babinet's principle in order to systematically integrate the previous introduced methods. Babinet's principle simply states that

$$U_{total} = U_1 + U_2 + U_3 + \dots + U_n, \quad n = 1, 2, 3, \dots \quad (78)$$

U_{total} : total diffraction pattern, $U_1, U_2, U_3, \dots, U_n$: different independent diffracting aperture.

The condition of this principle is applied only to the same observation point or plane in Equation 78. Also, the calculation must be multiplied by the phase difference of the assumed optical sources (point sources).

The spatial filter can be decomposed into two parts: effective upper and effective lower wedges. The second step is to decompose the effective upper wedge into the upper wedge and upper edge of the aperture. The same decomposition procedure also applies to the effective lower wedge.

According to the common example of Babinet's principle, if there are two different diffracting apertures and one fixed observation point or plane, the total diffraction effect can be written as $U_{total} = U_1 + U_2$. U_{total} : total or sum of the diffracting pattern, U_1 : diffraction by the first structure, U_2 : diffraction by the second structure

As shown in Fig. 78, the total effect will be that no aperture (obstruction) exists, because the second aperture is the complementary of the first aperture (the obstruction).

Obstruction 1: aperture with opening

Obstruction 2: complementary of obstruction 1, blockage of the opening of the aperture

Effective obstruction: Sum of obstructions 1 and 2, no obstruction exists

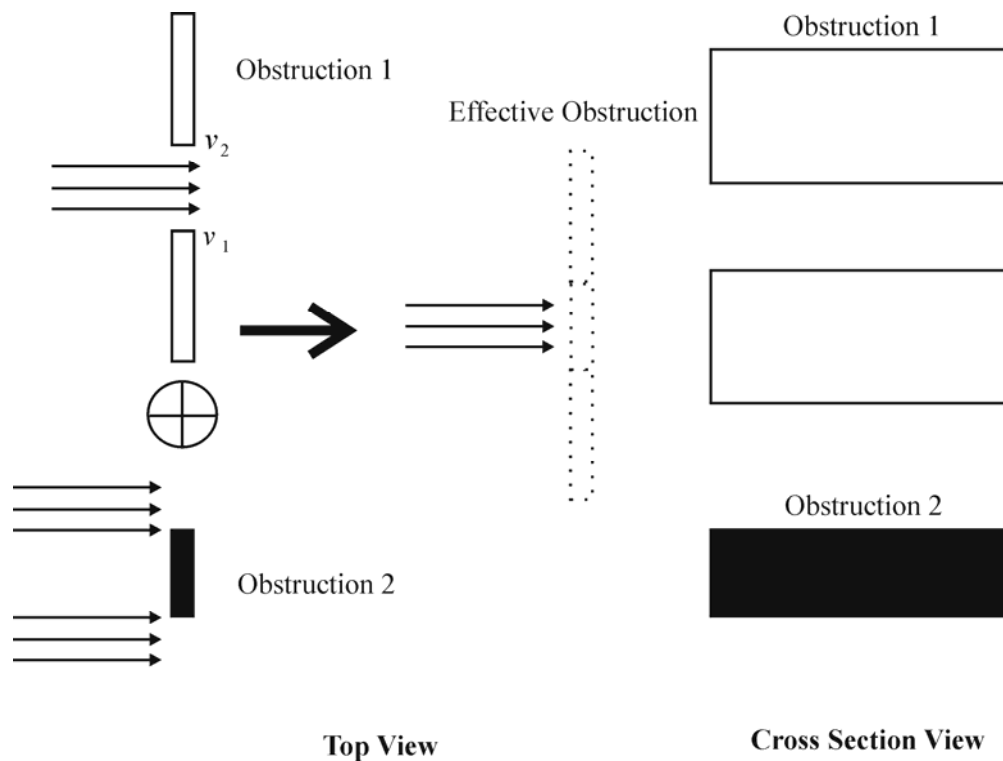


Figure 78. Special example of Babinet's principle

In the next chapter, I will apply the concept of Babinet's principle to the decomposition of the spatial filter. The sum of the transmission calculation will include adjustment factors according to the phase shift of the deflected optical source.

Chapter 5. Research results

5.1 Fundamentals of the modeling methods for the spatial filter

5.1.1 Fresnel-Kirchhoff diffraction

The previous section has already described the wave equation derived by the Fresnel-Kirchhoff integral; the details of the calculations will be introduced in this section. In terms of spatial vectors, the calculation of the Fresnel-Kirchhoff calculation is based on these two conditions: (1) a small θ and (2) a large distance from P_1 to P_2 compared to

x_1 or x_2 as shown in Fig. 79. Therefore I replace $\frac{1}{sr}$ in Equation 62 with $\frac{1}{r_1 r_2}$, and the term $e^{-jk(s+r)}$ becomes $e^{-jk(r_1+r_2)}$.

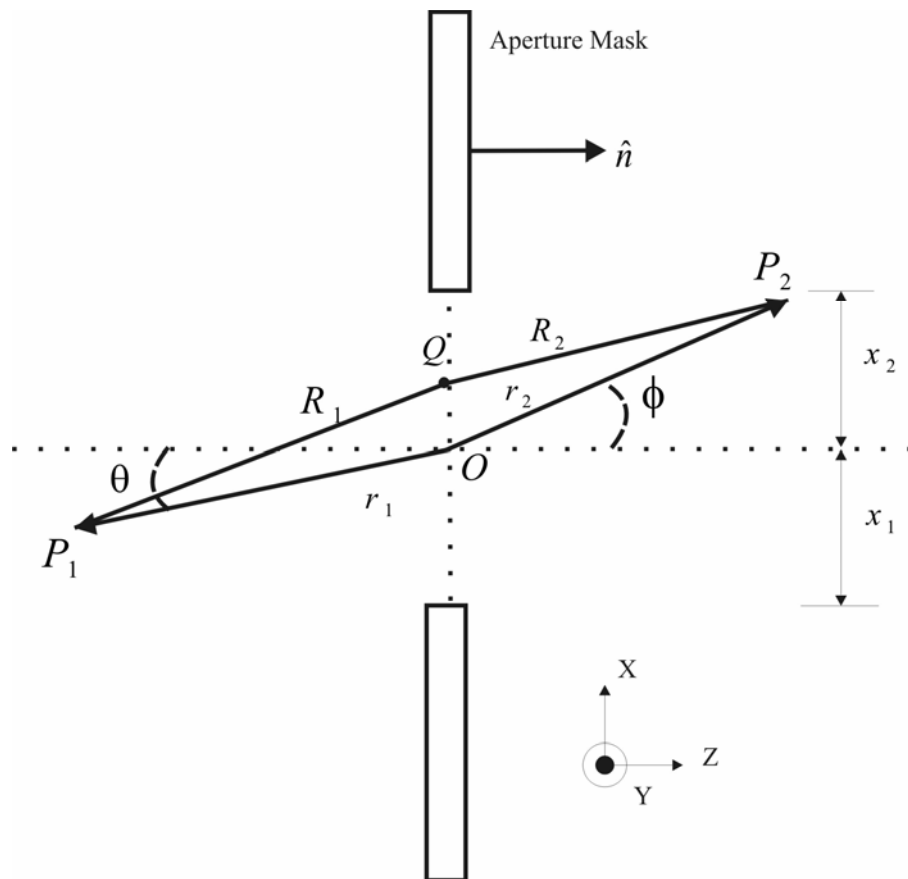


Figure 79. Dimensional specifications of the Fresnel-Kirchhoff integral

If we rewrite the Fresnel-Kirchhoff integral formula of Equation 61, and if we define the dimensional specifications of the aperture as shown in Fig. 79, an incident wave of constant amplitude A for electric field at P_2 is

$$E = \frac{j \cdot k \cdot A}{4\pi \cdot r_1 \cdot r_2} [(\hat{n} \cdot \hat{r}_2) - (\hat{n} \cdot \hat{r}_1)] \cdot \int_S e^{-j \cdot k \cdot (R_1 + R_2)} dS' \quad (79)$$

The diffraction coefficient [43] is defined as

$$D = \frac{E}{E(P_2 \sim P_1)} = \frac{j \cdot k}{4\pi \cdot L} [(\hat{n} \cdot \hat{r}_2) - (\hat{n} \cdot \hat{r}_1)] \cdot \int_S e^{-j \cdot k \cdot (R_1 + R_2 - r_1 - r_2)} dS' \quad (80)$$

$$R_1 = |r_1 - r'| = \sqrt{r_1^2 - 2r_1 \cdot r' + r' \cdot r'}, \quad R_2 = |r_2 - r'| = \sqrt{r_2^2 - 2r_2 \cdot r' + r' \cdot r'}, \quad \phi = \theta,$$

$$L = \frac{r_1 \cdot r_2}{r_1 + r_2}, \quad E(P_2 \sim P_1) = \frac{A \cdot e^{-jk(r_1 + r_2)}}{r_1 + r_2} : \text{wave that is propagated from } P_1 \text{ to } P_2 \text{ without an}$$

aperture

In a later section, I will discuss and derive the case of $\phi \neq \theta$ especially for the electro-optical deflector.

As defined in Fig. 73, $\hat{n} = \hat{z}$ represents the directional vector. Using Taylor's expansion,

R_1 and R_2 are approximated as

$$R_1 = r_1 \cdot \sqrt{1 - \frac{2\hat{r}_1 \cdot r'}{r_1} + \frac{r' \cdot r'}{r_1^2}} = r_1 - \hat{r}_1 \cdot r' + \frac{1}{2 \cdot r_1} [r' \cdot r' - (\hat{r}_1 \cdot r')^2] \quad (81)$$

$$R_2 = r_2 \cdot \sqrt{1 - \frac{2\hat{r}_2 \cdot r'}{r_2} + \frac{r' \cdot r'}{r_2^2}} = r_2 - \hat{r}_2 \cdot r' + \frac{1}{2 \cdot r_2} [r' \cdot r' - (\hat{r}_2 \cdot r')^2]$$

(Taylor's expansion, $\sqrt{1+x} = 1 + \frac{1}{2}x - \frac{1}{8}x^2$)

The approximation is also based on the Fresnel region limit [44]

$$z < \frac{D^2}{\lambda} \quad (82)$$

D : cross-sectional area of the aperture

$$r' = x'\hat{x} + y'\hat{y}, \hat{r}_1 = -\hat{z}\cos\theta - \hat{x}\sin\theta, \hat{r}_2 = \hat{z}\cos\theta + \hat{x}\sin\theta, \hat{n} \cdot \hat{r}_2 = \cos\theta, \hat{n} \cdot \hat{r}_1 = -\cos\theta$$

$$\begin{aligned} R_1 + R_2 - r_1 - r_2 &= -(\hat{r}_1 + \hat{r}_2) \cdot r' + \frac{1}{2} \left[\left(\frac{1}{r_1} + \frac{1}{r_2} \right) \cdot (r' \cdot r') - \frac{(\hat{r}_1 \cdot r')^2}{r_1} - \frac{(\hat{r}_2 \cdot r')^2}{r_2} \right] \\ &= \frac{1}{2 \cdot L} \cdot [(x')^2 \cdot \cos^2 \theta + (y')^2] \end{aligned}$$

$$D = \frac{jk \cos \theta}{2\pi L} \int_{-x_1}^{x_2} \int_{-y_1}^{y_2} e^{-jk \cdot (\frac{1}{2}L) [(x')^2 \cdot \cos^2 \theta + (y')^2]} dx' dy' \quad (83)$$

The Fresnel integral is defined as

$$F(x) = C(x) - j \cdot S(x) = \int_0^x e^{-j(\pi/2)u^2} du \quad (84)$$

As shown in Fig. 80, the oscillation characteristics of the Fresnel integral will also appear in the result of the diffraction coefficient calculation.

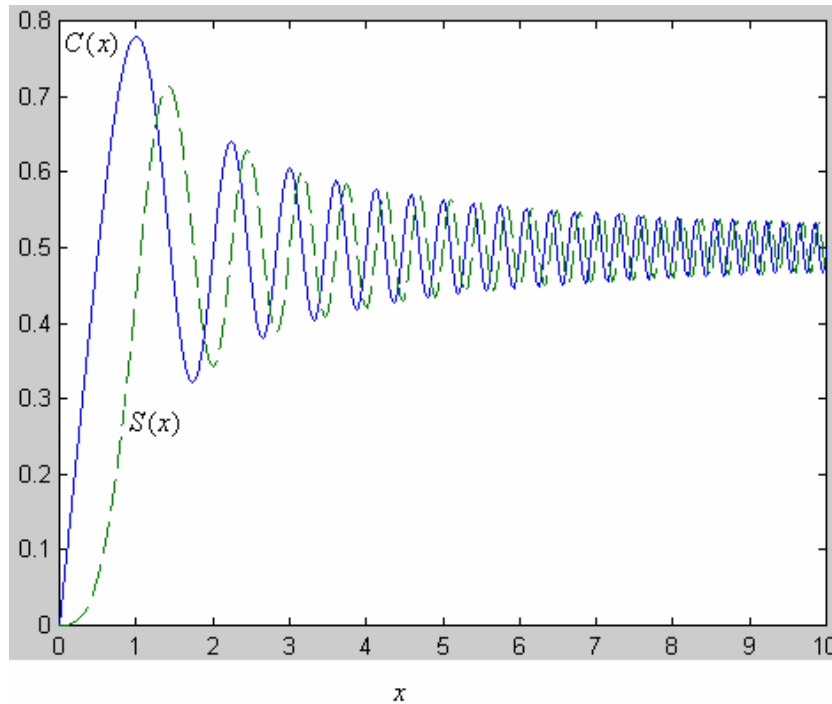


Figure 80. Matlab calculations and plot of Fresnel integral.

By using a change of variables, let $u_i = \sqrt{\frac{k}{\pi \cdot L}} \cdot y'_i, v_i = \sqrt{\frac{k}{\pi \cdot L}} \cdot x'_i \cos \theta,$

$$D = \frac{j}{2} \int_{-u_1}^{u_2} e^{-j\pi \frac{u^2}{2}} du \cdot \int_{-v_1}^{v_2} e^{-j\pi \frac{v^2}{2}} dv = \frac{j}{2} [F(u_2) - F(-u_1)] \cdot [F(v_2) - F(-v_1)] \quad (85)$$

For the 2-D calculation, set $y' = -\infty \sim \infty$ ($u_1, u_2 = -\infty \sim \infty$), and make $F(\infty) = \frac{1-j}{2}$.

Therefore the diffraction coefficient can be written as

$$D = \frac{F(v_1) + F(v_2)}{1-j}, \quad F(-x) = -F(x) \quad (86)$$

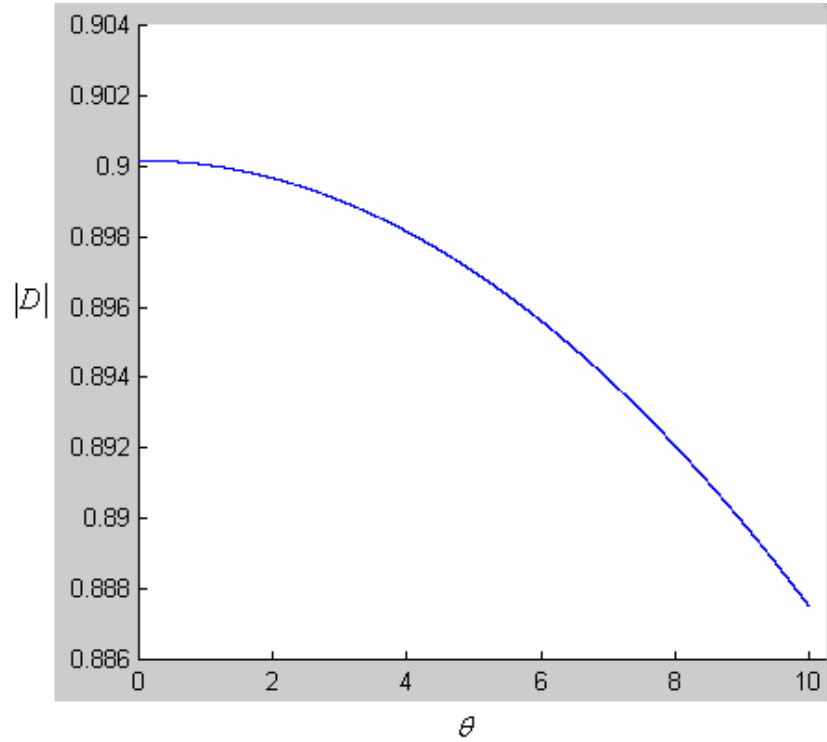


Figure 81. Matlab calculations and plot of $|D|$ versus θ . $r_1 = 5\mu m$, $r_2 = 3\mu m$, $\lambda = 0.633\mu m$, $x_1 = x_2 = 0.5\mu m$.

On the basis of the derivations from Equations 79 to 86, I derived the calculation for the transmission ratio of the deflected optical pulse to the spatial filter from the electro-optical deflector.

I multiply the phase term being cancelled in Equation 83 back, and define the transmission ratio as

$$T = \frac{E}{E_0} = \frac{j \cdot k}{4\pi \cdot r_1 \cdot r_2} [(\hat{n} \cdot \hat{r}_2) - (\hat{n} \cdot \hat{r}_1)] \cdot \int_S e^{-j \cdot k \cdot (R_1 + R_2)} dS' \quad (87)$$

By using the same derivation procedures already shown, I wrote the transmission ratio in the form of the Fresnel integral that features a modified factor:

$$T = \frac{L}{r_1 \cdot r_2} \cdot e^{-jk(r_1+r_2)} \cdot \frac{F(v_1) + F(v_2)}{1-j} \quad (88)$$

5.1.2 Edge diffraction

As illustrated in Fig. 79, the edge diffraction is the Fresnel-Kirchhoff diffraction of one side of the aperture only. The calculation sets v_1 or v_2 to ∞ , depending on the upper edge or the lower edge. The diffraction coefficient is therefore

$$D = \frac{1}{1-j} \cdot \left(F(v) + \frac{1-j}{2} \right) \quad (89)$$

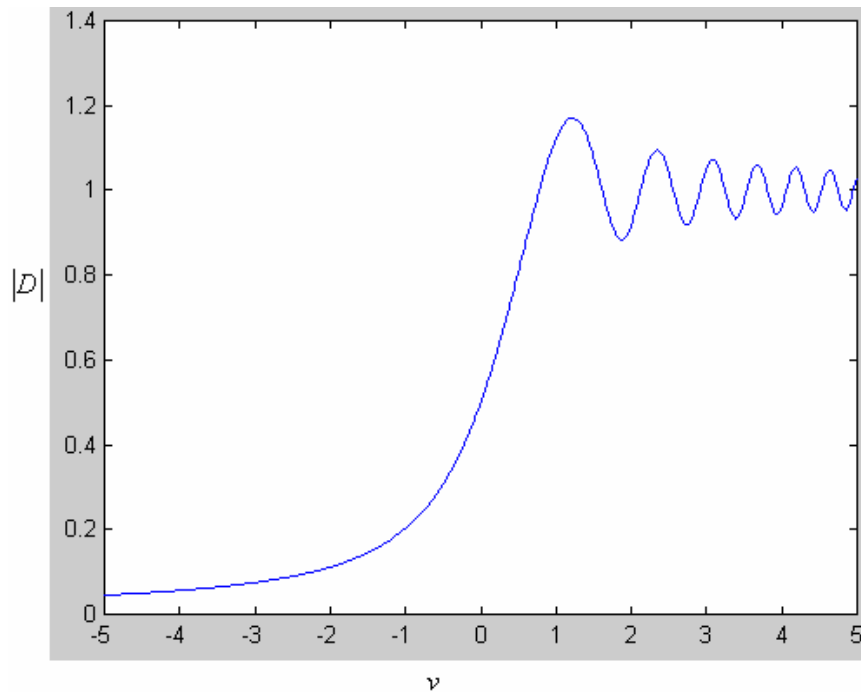


Figure 82. Matlab calculations and plot of $|D|$ versus v .

Figure 83 is an example of edge diffraction for the same case as in Fig. 81.

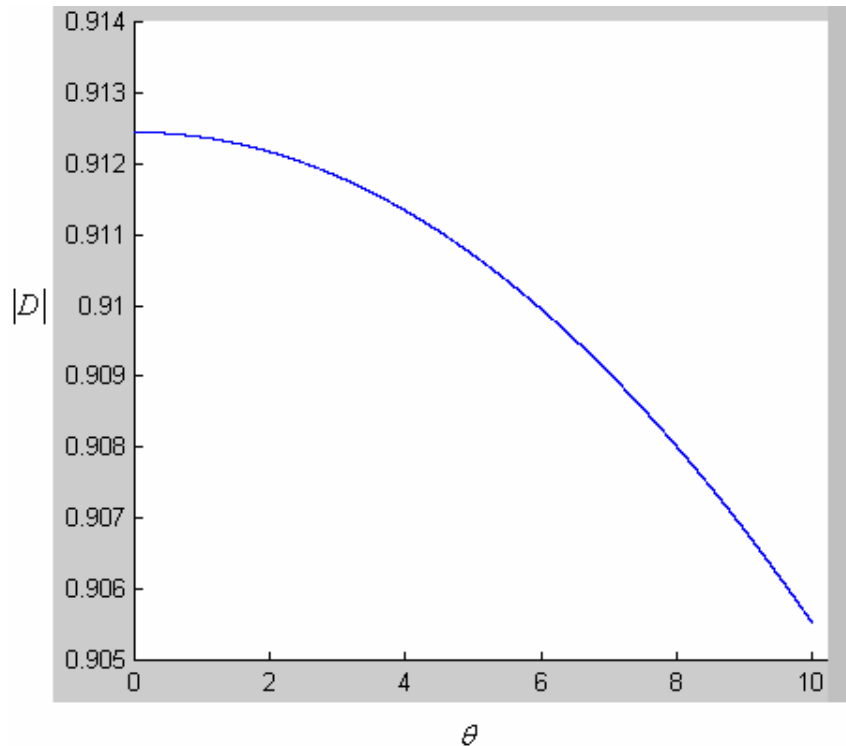


Figure 83. Matlab calculations and plot of $|D|$ versus θ . $r_1 = 5\mu m$, $r_2 = 3\mu m$, $\lambda = 0.633\mu m$, $x_1 = 0.5\mu m$.

I wrote the transmission ratio caused by the edge of the aperture as

$$T = \frac{L}{r_1 \cdot r_2} \cdot e^{-jk(r_1+r_2)} \cdot \frac{1}{1-j} \cdot \left(F(v) + \frac{1-j}{2} \right) \quad (90)$$

5.1.3 Cylindrical wave equation and wedge diffraction

As shown in Chapter 4.3, the cylindrical wave representation of the wedge structure can be applied to the edge structure of the spatial filter. In this section, the modal solution for the wedge structure will be transformed with Green's function relative to circuit theory.

In order to represent the total field in the form of unit amplitude incidence, I introduce Green's function for the final part of the derivation.

For example, a solution of the R-L circuit is

$$L \frac{di}{dt} + Ri = v(t) , \quad i(t) = \frac{V_0}{L} e^{-(R/L)(t-t')} \quad t \geq t' \quad (91)$$

Green's function for the solution is simply related as

$$G(t, t') = \frac{1}{L} e^{-(R/L)(t-t')} \quad t \geq t' \quad (92)$$

The next equation is continued from Equation 76 in Chapter 4.3, and is similar to Equation 92; Green's function is used to represent the total field [24] as

$$H_z^t = \frac{\omega \mathcal{I}_m}{4} G$$

$$E^t = \frac{1}{j\omega \varepsilon} \nabla \times H$$

$$G = \frac{1}{n} \sum_{m=0}^{\infty} \varepsilon_m J_{m/n}(\beta\rho) H_{m/n}^2(\beta\rho') \left[\cos \frac{m}{n}(\phi - \phi') + \cos \frac{m}{n}(\phi + \phi') \right], \quad \varepsilon_m = \begin{cases} 1 & m = 0 \\ 2 & m \neq 0 \end{cases} \quad (93)$$

For the case of $\beta\rho' \rightarrow \infty$, Equation 93 is simplified to be

$$G = \sqrt{\frac{2}{\pi\beta\rho'}} \cdot e^{-j(\beta\rho' - \pi/4)} F(\beta\rho) \quad (94)$$

$$F(\beta\rho) = \frac{1}{n} \sum_{m=0}^{\infty} \varepsilon_m J_{m/n}(\beta\rho) e^{j(m/n)(\pi/2)} \left[\cos \frac{m}{n}(\phi - \phi') + \cos \frac{m}{n}(\phi + \phi') \right],$$

J : Bessel function

Figures 85 and 86 are examples of the total field response of Green's function (G), which is just above. The parameters are

$$n = 1.37$$

$\alpha = 113.4^\circ$, wedge angle (the right-hand half of the spatial filter)

ϕ' : 60° , incident field

ϕ : observation_point angle, $0 \sim n \cdot 180$ degrees

ρ : λ , $\lambda = 0.633 \mu\text{m}$. ρ' : 1000λ and 10λ

β : wavenumber, $2\pi/\lambda$

Figure 84 is the plot of the Bessel function of the first kind ($J_0(x)$) and the Hankel function of the second kind ($H_2^2(x)$). The plot has characteristics that are similar to those of the Fresnel integral, which are shown in Fig. 80. Examples of the related oscillation appear in Figs. 85 to 88.

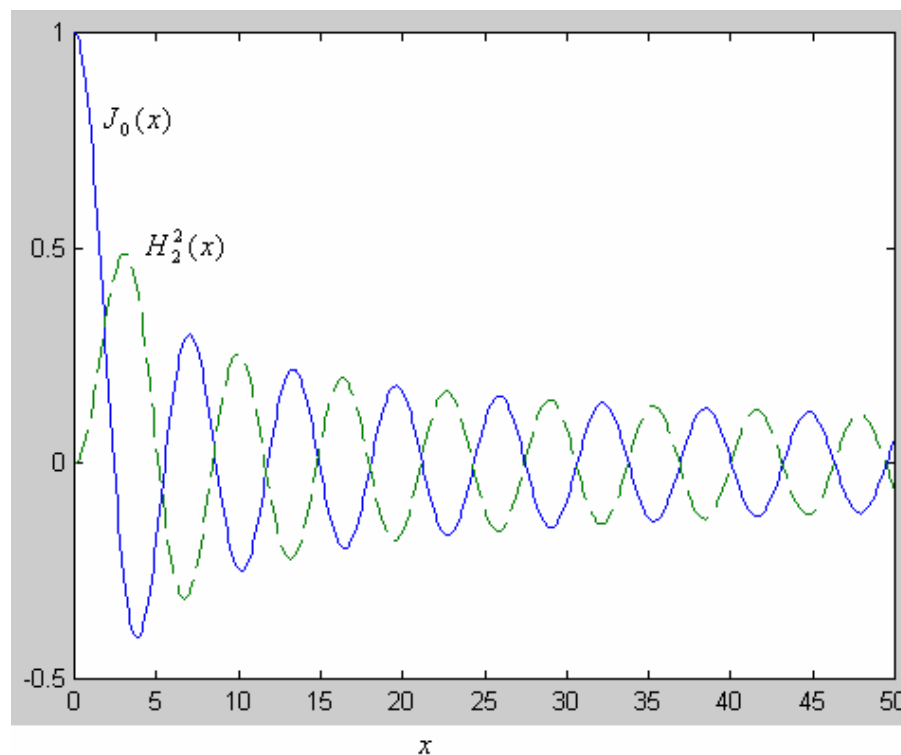


Figure 84. Matlab calculations and plot of Bessel and Hankel functions.

In Figures 86 and 88, the arrow line stands for the incident field; the bold line stands for the wedge.

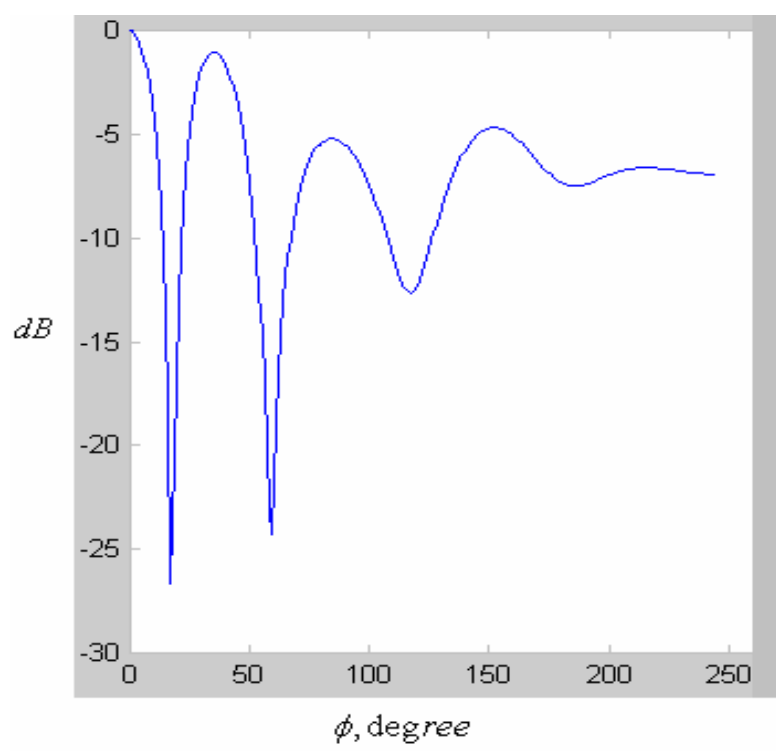


Figure 85. Matlab calculations and plot of $G(\rho' = 1000\lambda)$, Equation 94.

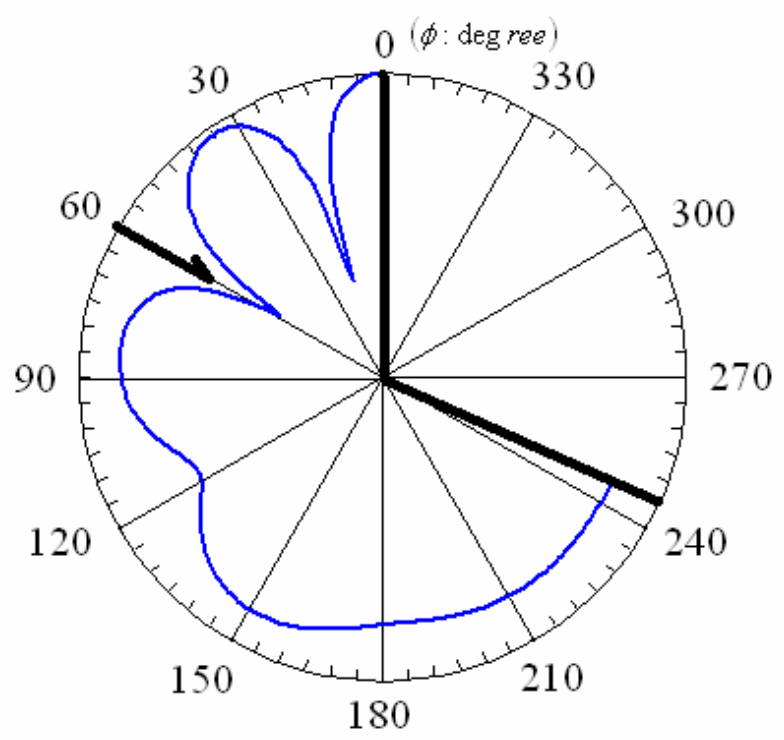


Figure 86. Radar plot of Figure 85.

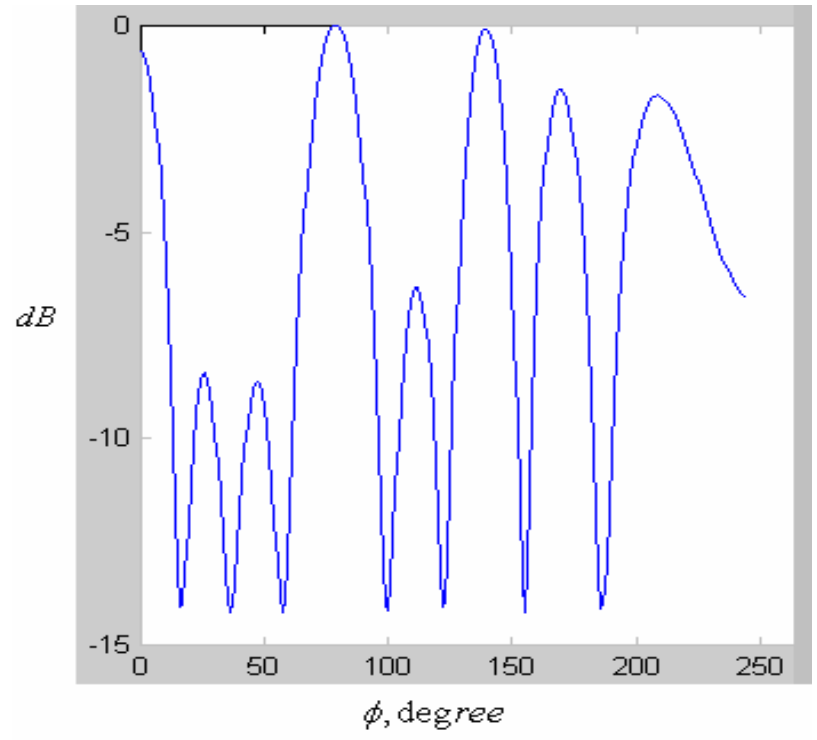


Figure 87. Matlab calculations and plot of $G(\rho' = 10\lambda)$, Equation 93.

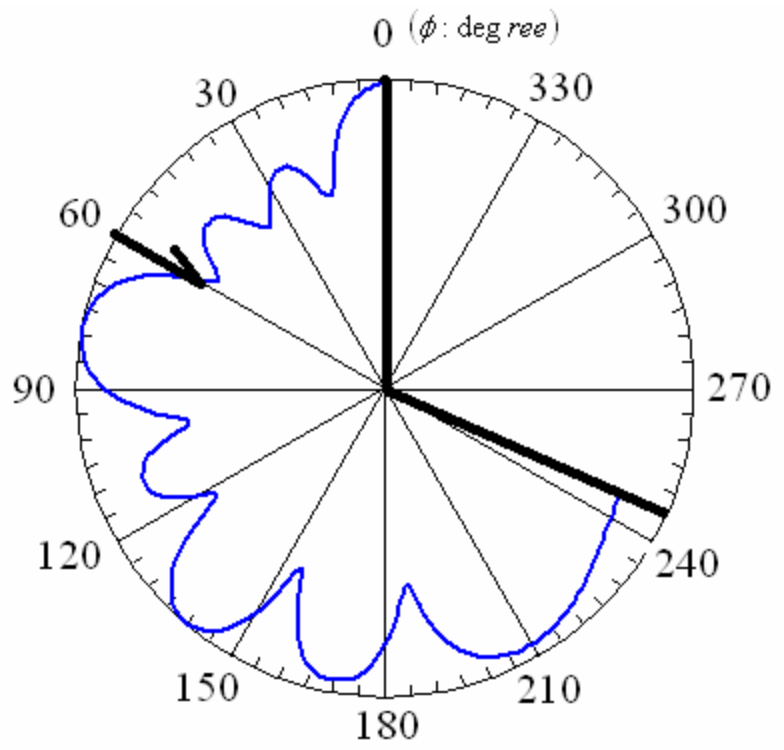


Figure 88. Radar plot of Figure 87.

5.1.4 Fresnel equations

As shown in Fig. 89, the wave passes the spatial filter and then strikes the entrance of the optical waveguide. Also, Figures 90 and 91 plot the transmission coefficient (t) and the reflection coefficient (r). Underlying the examples is the assumption that, in Equation 71, $n_2 = 1.5$ and $n_1 = 1$.

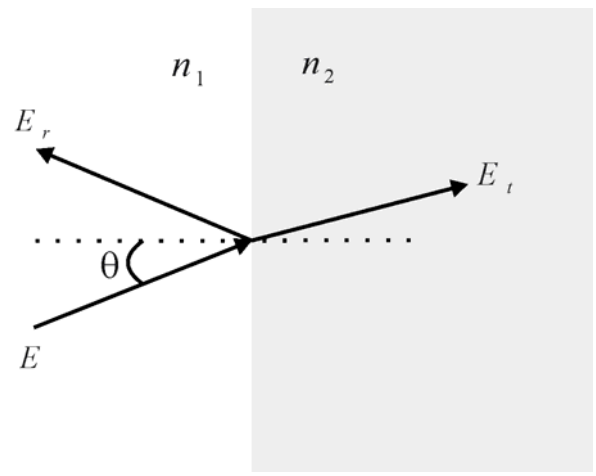


Figure 89. E_t : transmitted electric field, E_r : reflected electric field.

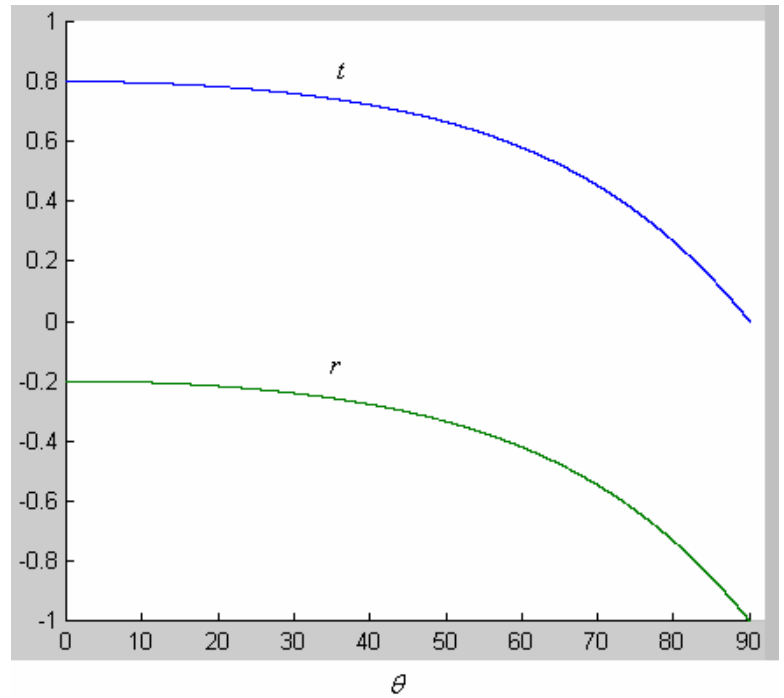


Figure 90. Matlab calculations and plot of TE mode.

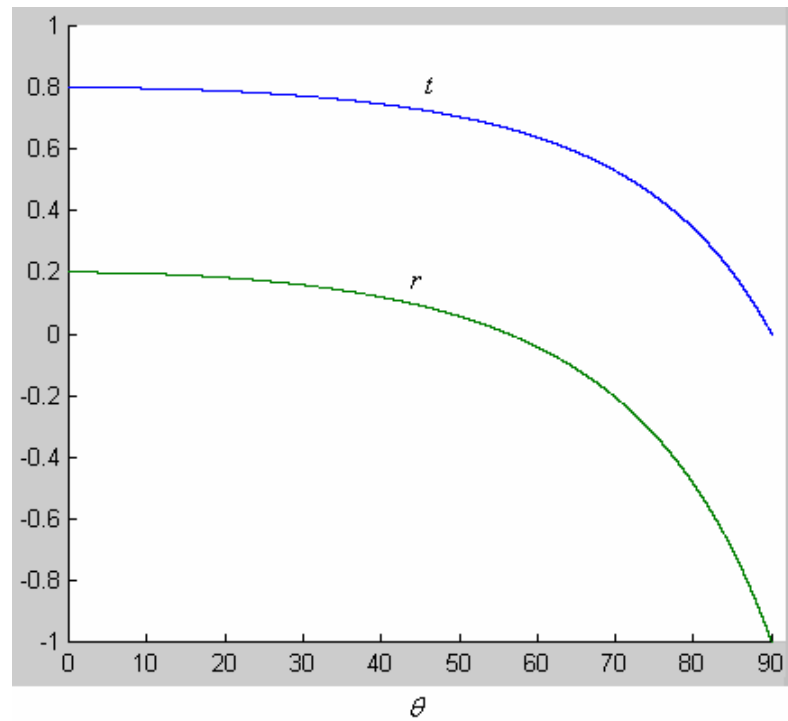


Figure 91. Matlab calculations and plot of TM mode.

5.1.5 Babinet's principle

The purpose of this section is to make use of Equations 86 and 89 in order to prove the special example as illustrated in Fig. 78.

I use Equations 86 and 89 to calculate the diffractions of these three regions in Fig. 78:

$$\text{Obstruction 1: } U_1 = \frac{F(v_1) + F(v_2)}{1 - j},$$

$$\text{Obstruction 2: } U_2 = \frac{F(\infty) - F(v_2) + F(-v_1) - F(-\infty)}{1 - j} = \frac{F(\infty) - F(v_2) - F(v_1) + F(\infty)}{1 - j}.$$

Therefore the total diffraction is

$$U_1 + U_2 = \frac{F(\infty) + F(\infty)}{1 - j} = 1, \quad F(\infty) = \frac{1 - j}{2}$$

The result simply establishes the accuracy of Fig. 78's description of the special case composed by the complement apertures, and I will make use of the concept in order to derive the total transmission ratio in Chapter 5.2.

5.2 Decompositions of the spatial filter and systematic integration of the calculations into transfer functions

This section describes a method for the decomposition of the spatial filter's structure. To this description, this section applies methods that already appeared in Chapter 5.2. Also, this section describes the related systematic integration, which includes adjustment factors that act according to the phase change.

In Chapter 4.3, I applied Babinet's principle to the calculation for the transmission ratio. My use of this principle is due to the fixed observation point as shown in Fig. 92. I define the optical source as comprising three parts: center, upper, and lower. I assume that the three parts are equal in amplitude and that no cross coupling exists.

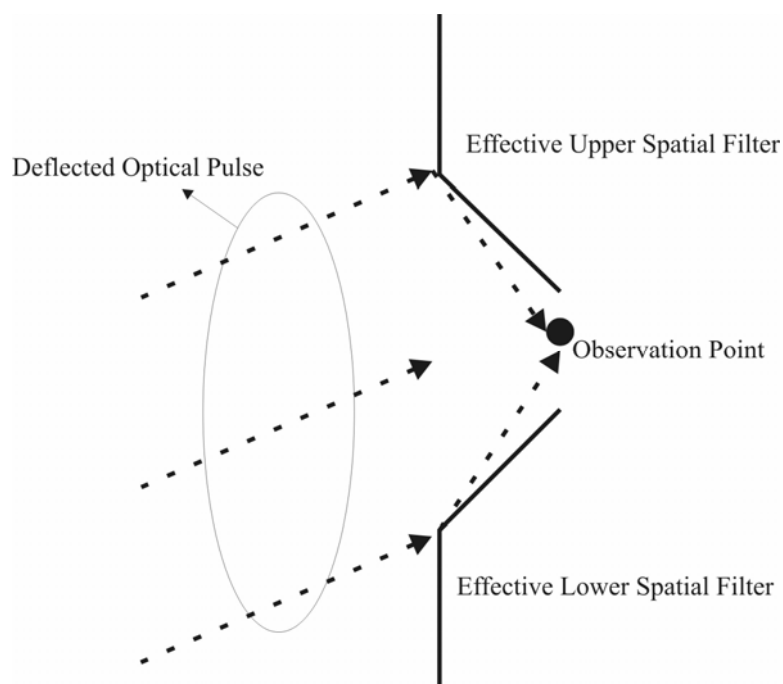


Figure 92. Illustration of both the spatial filter and the observation point

Figure 93 demonstrates the decomposition of the spatial filter's structure. I calculate the center wave by using the Fresnel-Kirchhoff integral for one side of the aperture edge. The wedge structure can be directly applied to the upper or lower edge of the spatial filter.

As shown in Fig. 93, the spatial filter undergoes two decompositions so that the resulting simplification enables the entire structure to fit the calculation of the edge and the wedge diffraction calculations.

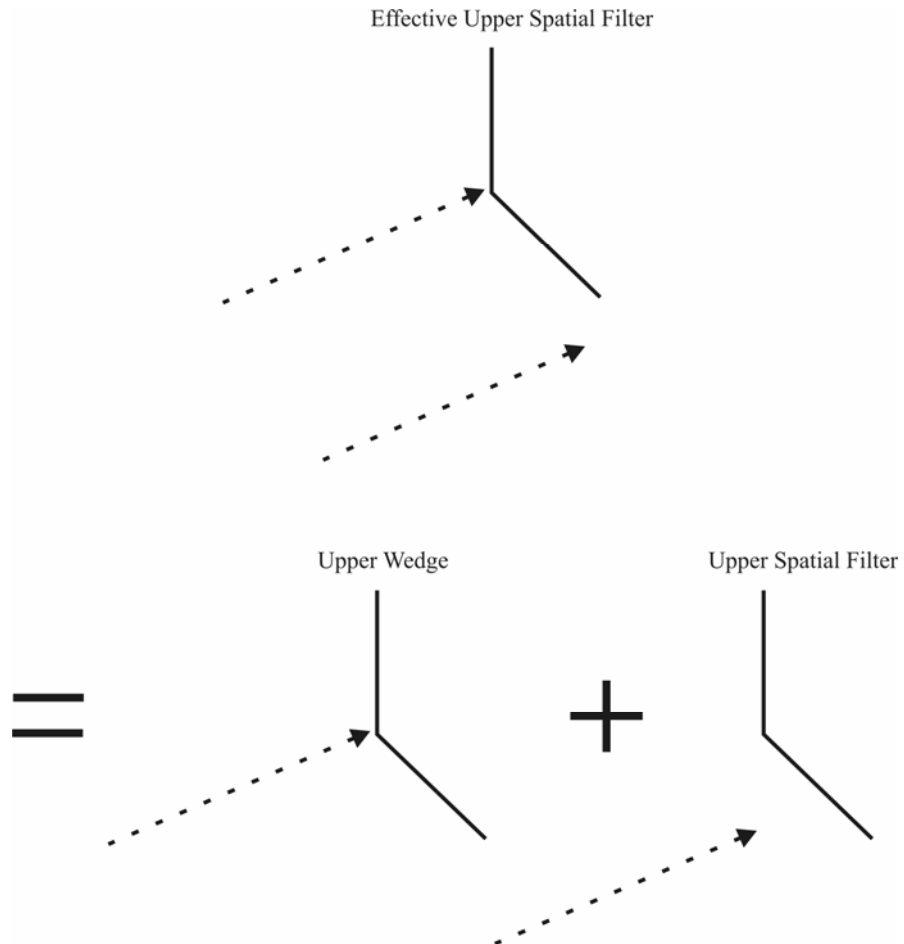


Figure 93. First decomposition of the spatial filter

In Equation 78, the total diffraction of different apertures (obstructions) can be written as

$$U_{total} = \sum_{i=1}^n U_i \quad , \quad i = 1, 2, 3, \dots \quad (95)$$

Equation 95 is transformed into the transmission ratio by my derivations in Equations 88 and 90, that is,

$$T_{total} = \sum_{i=1}^n T_i \quad , \quad T_i = \frac{L}{r_1 \cdot r_2} \cdot e^{-jk(r_1+r_2)} \cdot U_i \quad , \quad i = 1, 2, 3, \dots \quad (96)$$

$$U_{total} = \sum_{i=1}^n U_i = 1 \quad , \quad i = 1, 2, 3, \dots$$

$$\therefore \frac{L}{r_1 \cdot r_2} \cdot e^{-jk(r_1+r_2)} \cdot \sum_{i=1}^n U_i = \frac{L}{r_1 \cdot r_2} \cdot e^{-jk(r_1+r_2)} = \sum_{i=1}^n T_i \quad (97)$$

The normalization of the diffraction coefficient in Equation 85 also applies to Equation 97, therefore the normalized transmission ratio is also $\sum_{i=1}^n T_i = 1$. However the Matlab code implementation of Equation 97 is still written as

$$\sum_{i=1}^n \left(\frac{L}{r_1 \cdot r_2} \right) \cdot U_i = 1 \quad (98)$$

Also, as shown in Fig. 94, the total diffraction by the three apertures (A_1 , A_2 , $com(A_3)$) is $U_1 + U_2 + com(U_3) = 1$ because it is the case that $A_1 = 1 - (A_2 + com(A_3))$ in the cross-section view of the spatial filter (the concept of Babinet's principle). $com(\)$: complement aperture, and A_3 is transparent in Fig. 94.

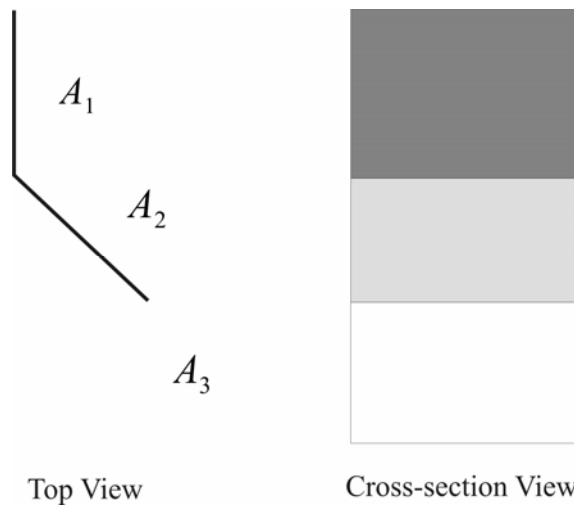


Figure 94. Top and cross-section views of the spatial filter

As illustrated in Fig. 94, I define $i = 1,2,3$. Therefore,

$$T_2 + T_3 = 1 - T_1 - \text{com}(T_3) = 1 - \frac{L}{r_1 \cdot r_2} \cdot (U_1 + \text{com}(U_3)),$$

$\text{com}(\)$: complement aperture(99)

After my derivation and my assumption of this principle in the conclusion of Equations 98 and 99, I decompose the upper edge of Fig. 93 into a simpler case, as shown in Fig. 95.

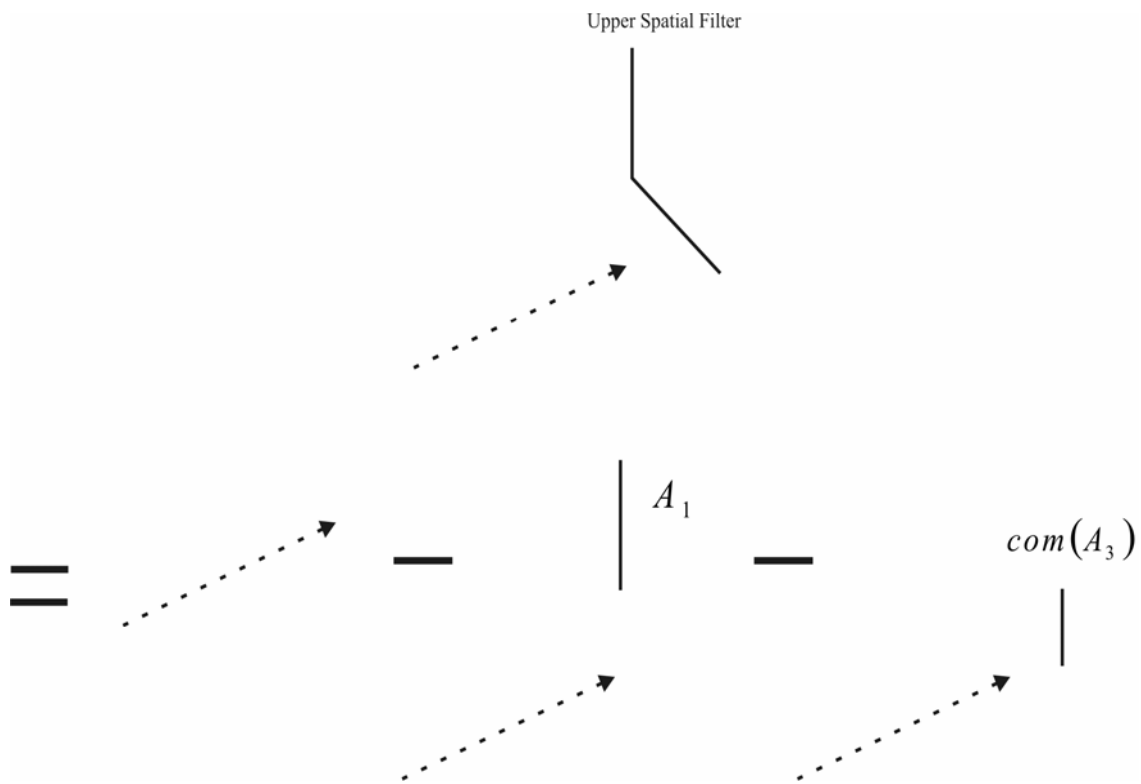


Figure 95. Second decomposition of the spatial filter

The calculation of the proposed method in Fig. 93 needs to have the phasor adjustment [45] because Babinet's principle is for one single optical source; there is no change to the observation point.

As illustrated in Fig. 96, the deflected optical source is propagated from the output of the electro-optical deflector, as illustrated in Fig. 26. The deflected pulse has an angle of θ .

$$E(\text{Reference}) + E(\text{Upper}) + E(\text{Lower}) = E_0 + E_0 \cdot e^{j\alpha} + E_0 \cdot e^{-j\alpha} \quad (100)$$

α : relative phase to the reference point, $\alpha = kd \cdot \cos\theta + \text{phase excitation}$. The excitation is 0 because there is only one single group of the optical source.

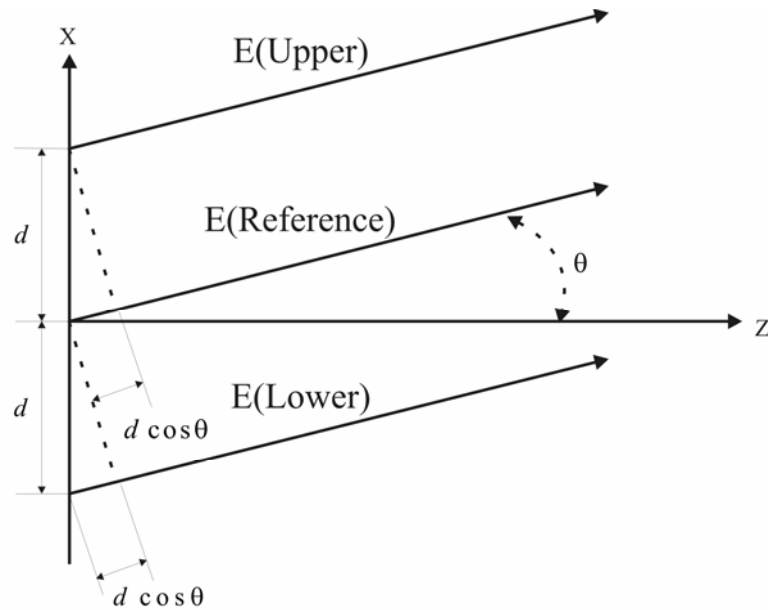


Figure 96. Spatial phase definition of the optical source

After the relative phase is adjusted, the calculation for the transmission ratio of the spatial filter is written as

$$T_{\text{system}} = \text{Waveguide transmission} \cdot (E_0 \cdot G_{\text{upper filter}} + E_0 \cdot G_{\text{lower filter}} + E_0 \cdot e^{j\alpha} \cdot G_{\text{upper wedge}} + E_0 \cdot e^{-j\alpha} \cdot G_{\text{lower wedge}}) \quad (101)$$

$G_{\text{upper filter}}$, $G_{\text{lower filter}}$: transmission ratio ($T_2 + \text{com}(T_3)$) defined in Equation 99,

$G_{upper\ wedge}$, $G_{lower\ wedge}$: Green's function defined in Equations 93 and 94.

The sum of the diffractions can also be written in the similar following form

$$U_{system} = U_{upper\ filter} + U_{lower\ filter} + e^{j\alpha} \cdot U_{upper\ wedge} + e^{-j\alpha} \cdot U_{lower\ wedge} \quad (102)$$

Referring to the conclusion described in Equation 101, Fig. 97 illustrates the systematic integration in Equation 101.

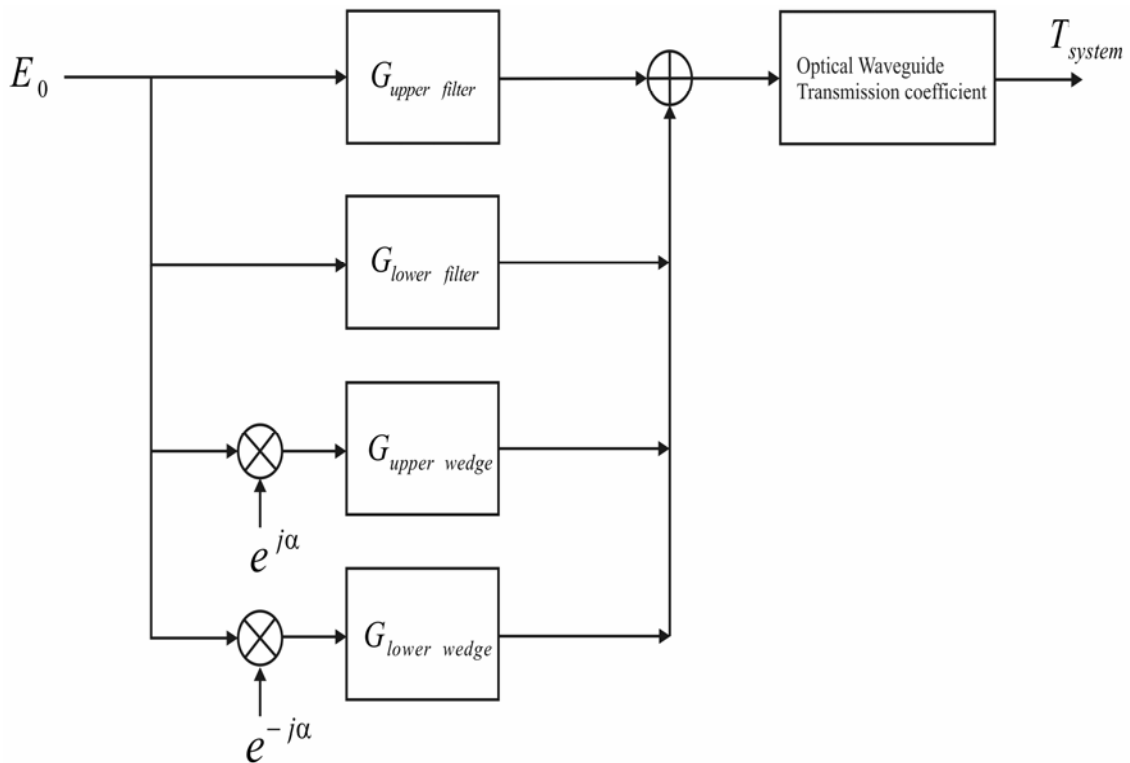


Figure 97. Systematic integration of the transmission calculation.

In the next section, I will calculate both the diffraction and the transmission ratio on the basis of the functions already defined, and investigate the total transmission ratio on the basis of the diagram in Fig. 93.

5.3.1 Basic setup of the electro-optical deflector and spatial filter array

Figure 98 illustrates the top view of Fig. 26 (3-dimensional illustration) in Chapter 1-3, and it is also the basic geometrical setup of both the electro-optical deflector [46] and the spatial optical pulse collection array.

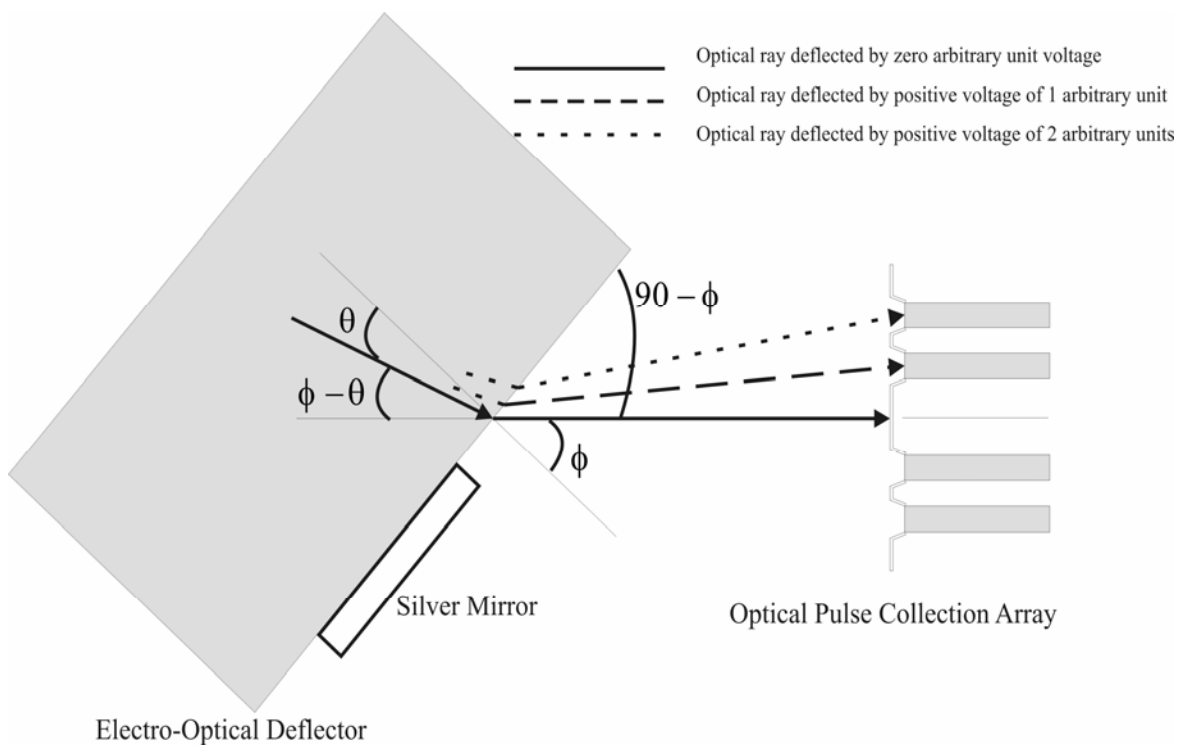


Figure 98. Electro-optical deflector and spatial optical pulse collection array

In this research, I apply the proposed methods and formulas to the system shown in Fig. 98 in order to evaluate the optical transmission ratio, including in particular diffracting structures. The appendix will cover this part of the electro-optical deflector because it is not the original focus of this research; however, the derived formulas of Equations 79 through 90 apply also to calculations of the transmission ratio at the output end of the deflector.

In order to align the zero-analog-voltage-induced optical pulse to the z-axis, the electro-optical deflector is tilted to a certain degree according to the calculations treated ahead.

First, it should be noted that the calculations of the tilting angle reflect the fact that zero-input electrical-analog voltage deflection is $\theta = 20^\circ$. The refractive index of the Lithium Tantalate ($LiTaO_3$) is 2.18 at the wavelength of $0.633\mu m$; therefore, the 20-degree incident optical ray will generate 48.21 degrees of deflection because of Snell's law

$$\sin \phi = n_{LiTaO_3} \sin \theta, n_{LiTaO_3} = 2.18, \theta = 20^\circ, \phi = 48.21^\circ$$

Therefore the tilting angle of the electro-optical deflector is calculated as

$$\theta = 20^\circ, \phi = 48.21^\circ, \phi - \theta = 28.21^\circ, 90^\circ - 48.21^\circ = 41.79^\circ$$

The optical pulse to be defined in the layout also has to be tilted by

$$\phi - \theta = 28.21^\circ$$

Also, as shown in Fig. 98, the deflection of the optical pulse is predicted in the assumption that $\Delta\theta = 1^\circ$ introduces $\Delta\phi \cong 3^\circ$ according to an arbitrary unit of analog voltage. The calculation makes use of the following content:

$$\sin \phi = n_{LiTaO_3} \sin \theta, n_{LiTaO_3} = 2.18, \theta = 20^\circ, \phi = 48.21^\circ.$$

$$\theta = 21^\circ, \phi = 51.37^\circ; \theta = 22^\circ, \phi = 54.75^\circ$$

Figure 99 illustrates the deflection based on the zero-input analog voltage.

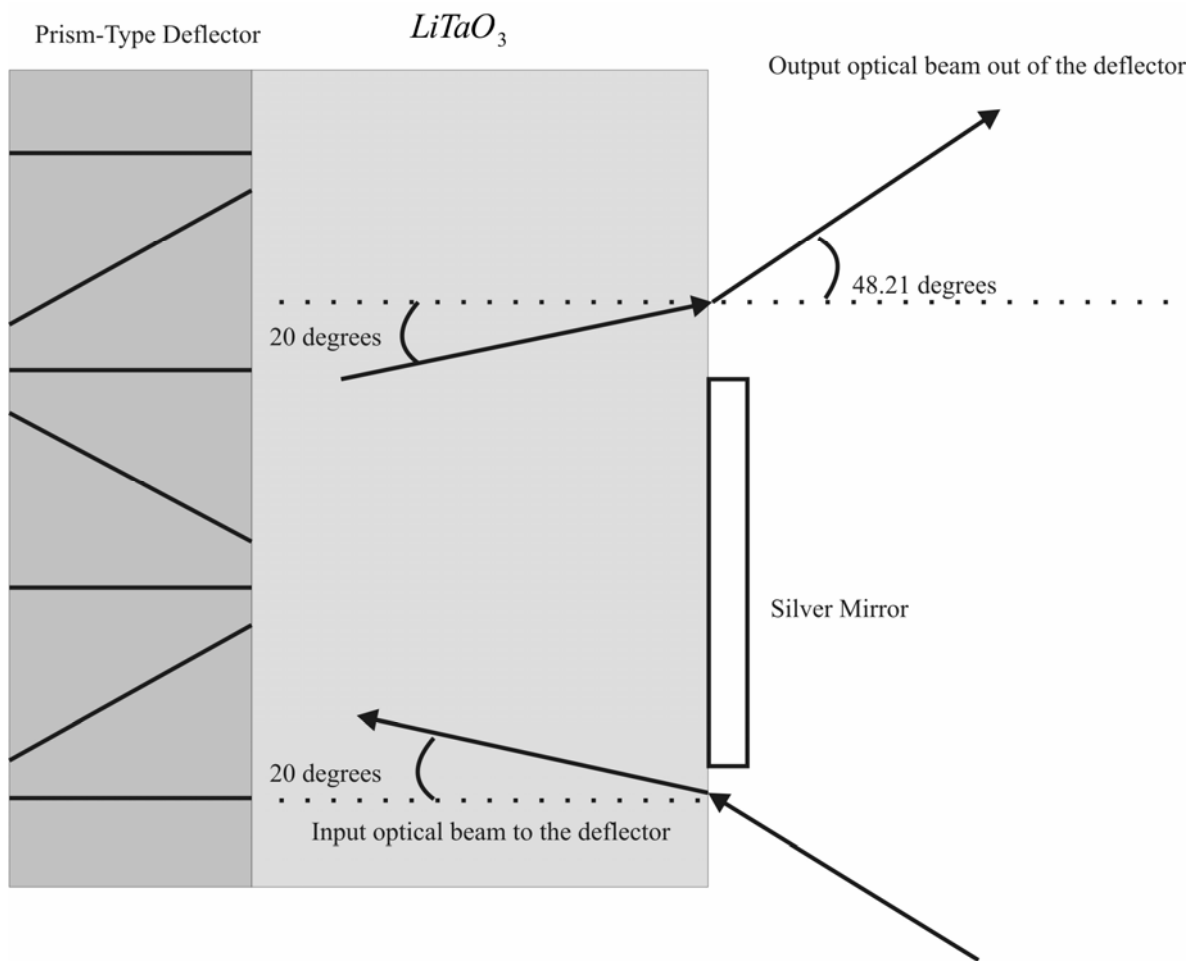


Figure 99. Electro-optical deflector

As shown in Fig. 100, the specifications of the optical pulse collection array tested in this research are

$$W1 = W2 = 2\mu m, W3 = 1\mu m, L1 = 4.5452\mu m, \theta = 1^\circ, 2^\circ, 3^\circ$$

Each single spatial filter of this array is uniformly-spaced.

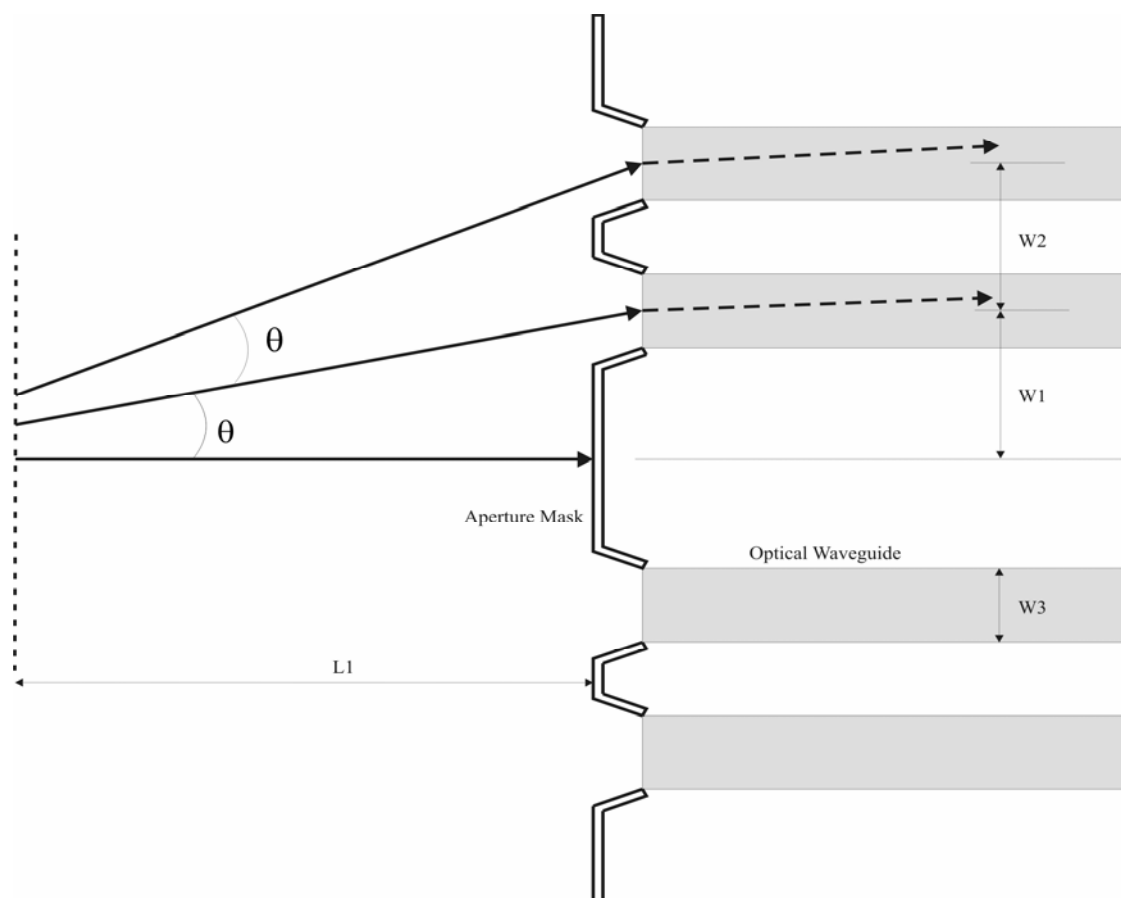


Figure 100. Spatial filter array specifications

5.3.2 Geometrical specifications of the spatial filter

Figure 101 is the θ scanning contour of the fixed r_1 and r_2 (as defined in Equation 86), but the contour is not compatible with the case I will analyze in Fig. 100. Therefore, I re-define the scanning contour along the lines illustrated in Fig. 102.

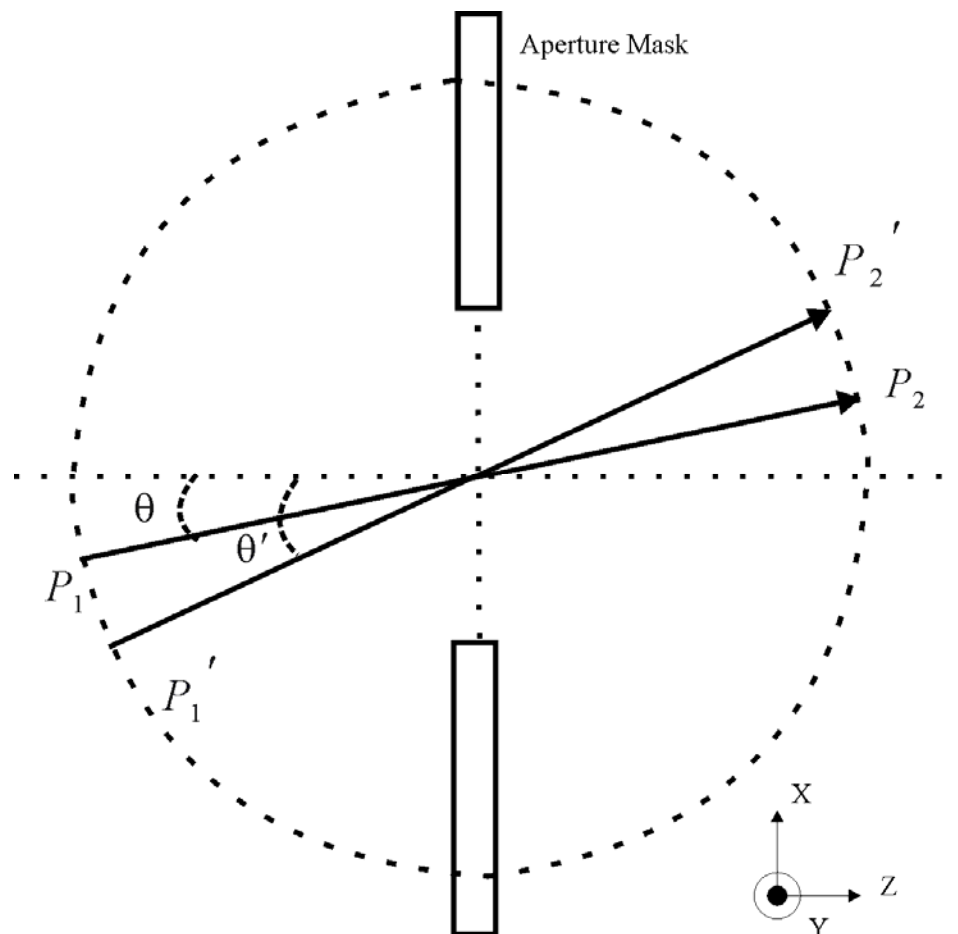


Figure 101. Circular scanning contour of θ

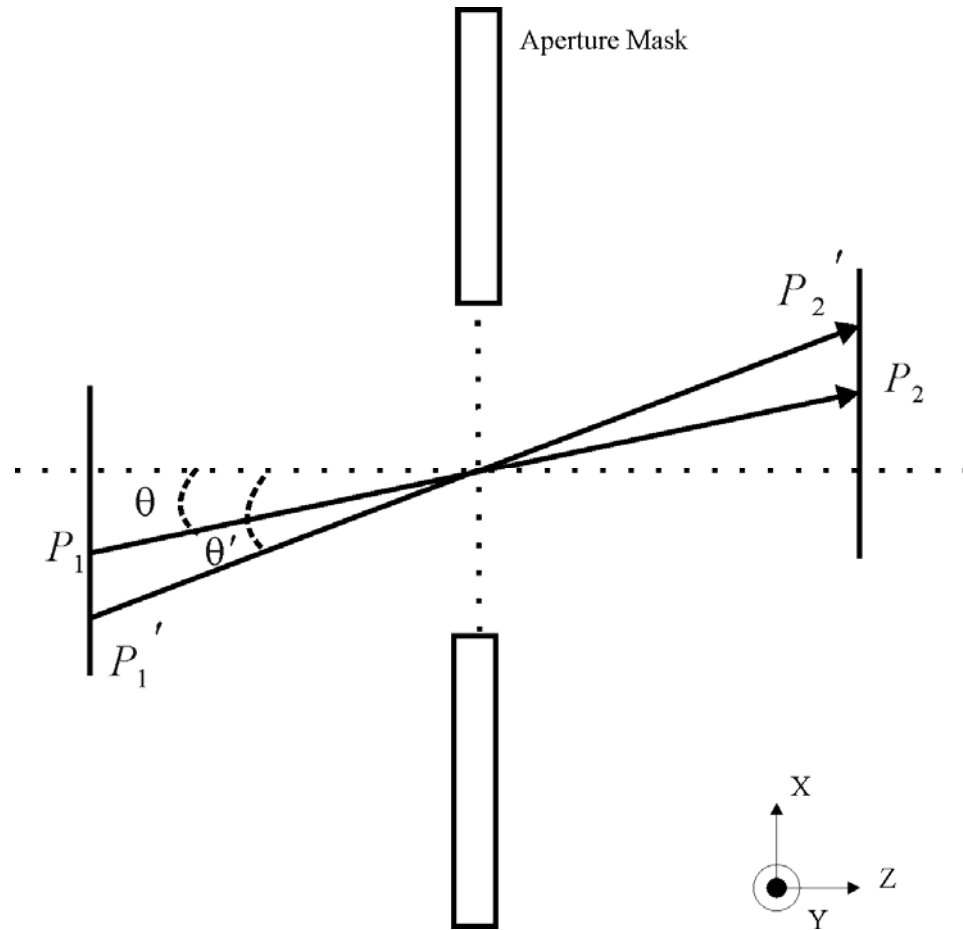


Figure 102. Expected linear scanning contour of θ

According to the scanning contour in Fig. 102, I define the geometrical specifications of the decomposed spatial filters of three parts and present simulation results by using the Matlab code.

Complete structure:

$$\text{TE mode, } r_1 = \frac{L1}{\cos \theta}, \quad r_2 = \frac{L2}{\cos \theta}, \quad ob1 = r_1 \cdot \sin \theta, \quad \Delta x = r_1 \cdot \sin \theta. \quad L1 = 4.5452 \mu\text{m},$$

$$L2 = 3 \mu\text{m}, \quad L3 = 5 \mu\text{m}, \quad \theta = 0 \sim 3^\circ, \quad ob1: \text{observation point 1}, \quad ob2: \text{observation point 2}.$$

Figure 103 illustrates the specifications for the complete structure.

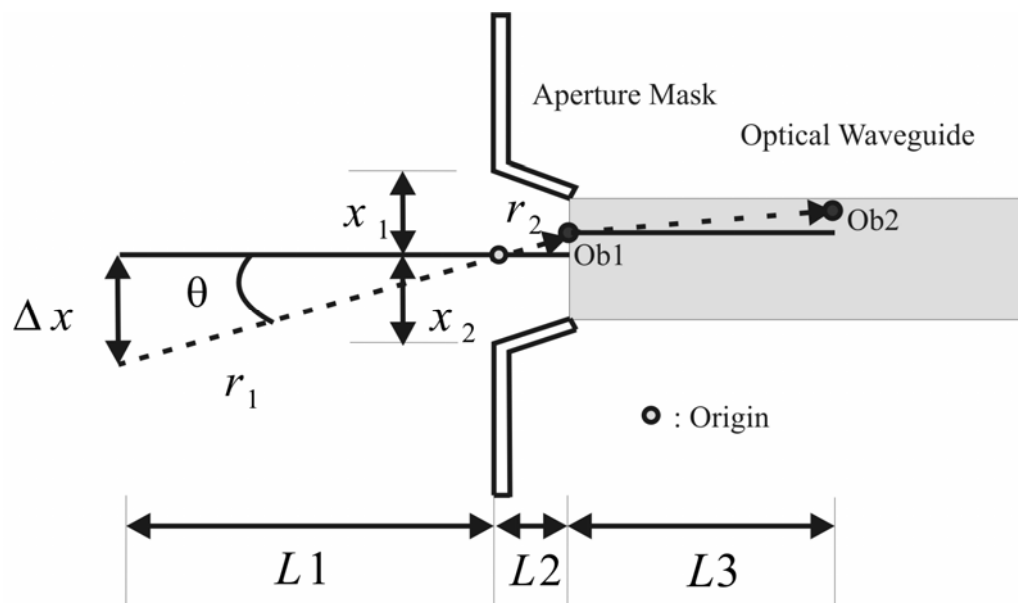


Figure 103. Complete specifications of spatial filter calculations.

Center structure:

The specifications for the center aperture are the same as the specifications for the complete structure, but there are no optical waveguide and observation point 2 in this structure. $L1 = 4.5452 \mu\text{m}$, $L2 = 3 \mu\text{m}$, $L3 = 5 \mu\text{m}$, $\theta = 0 \sim 3^\circ$, $x_1 = x_2 = 0.7266 \mu\text{m}$.

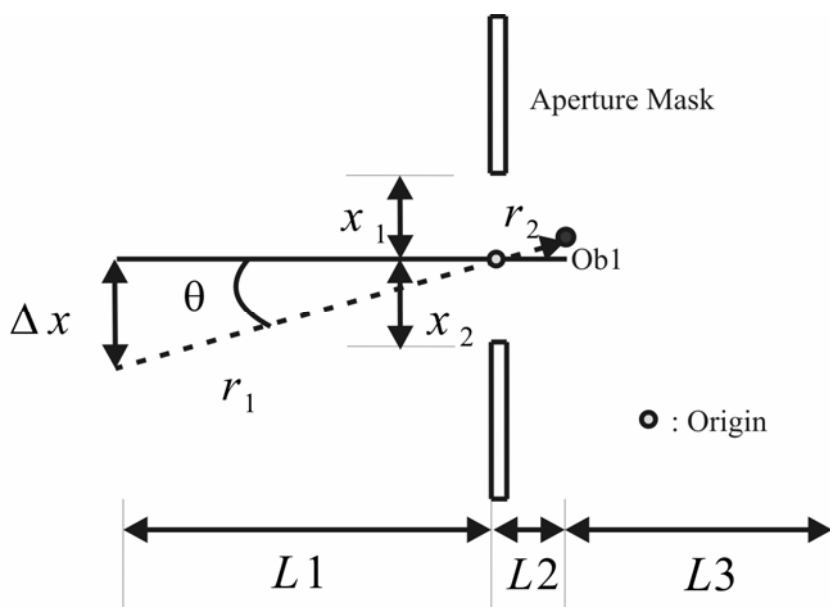


Figure 104. Geometrical specifications for the center wave calculation

Figure 105 is the code scanning result of Equation 88, and Fig. 106 is for Equation 90.

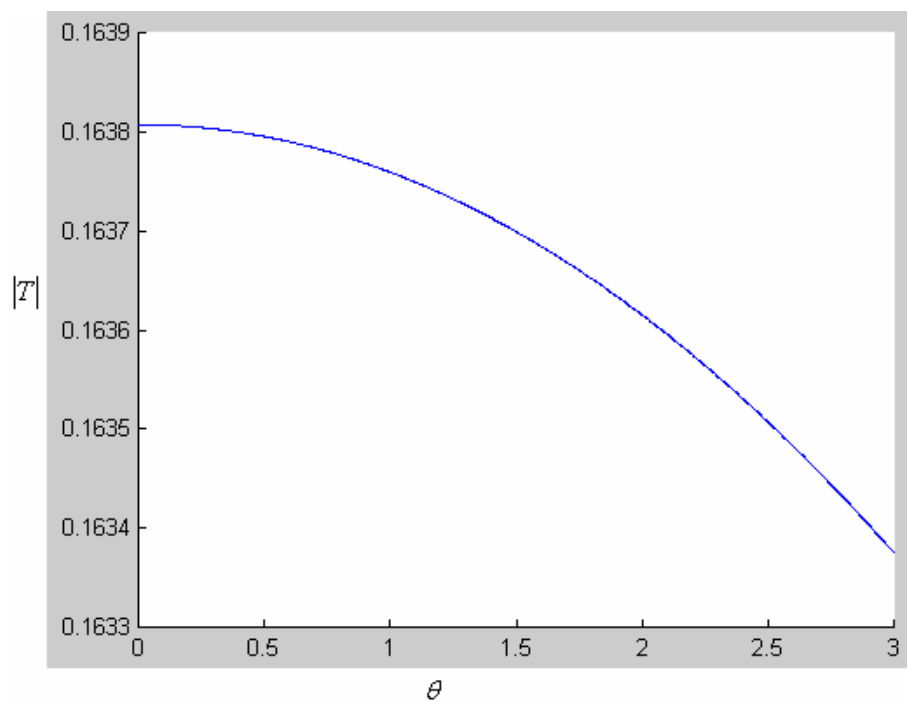


Figure 105. Matlab calculations and plot of $\theta = 0 \sim 3^\circ$ at observation point 1, Equation 88.

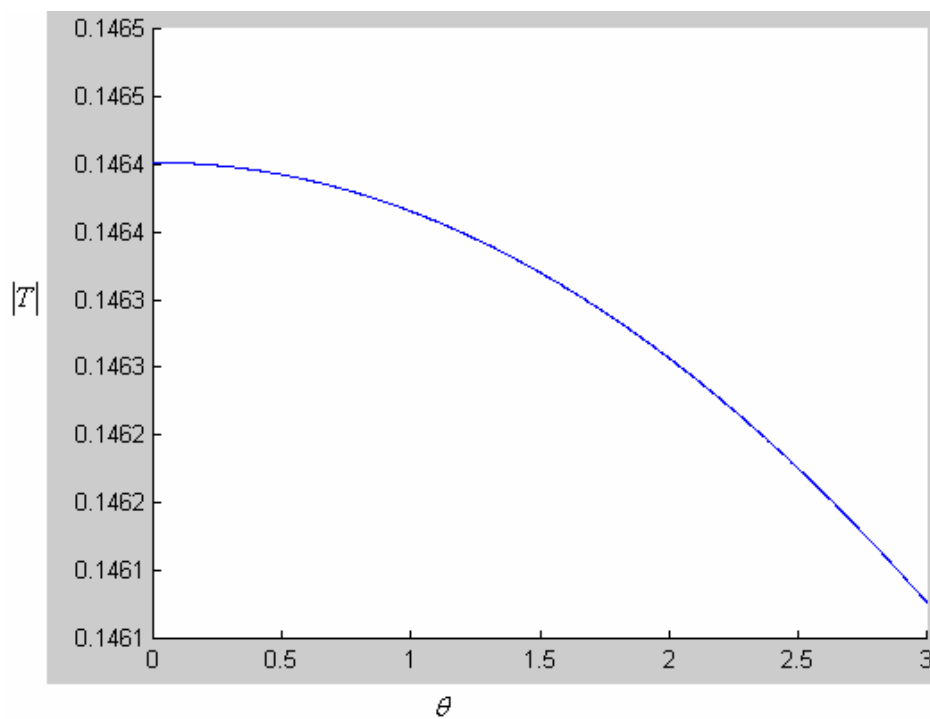


Figure 106. Matlab calculations and plot of $\theta = 0 \sim 3^\circ$ at observation point 1, Equation 90.

Upper:

$$\text{TE mode, } \phi' = 90^\circ + \theta, \rho' = \sqrt{L1^2 + (x_1 + \Delta x)^2}, \phi = 270^\circ - \tan^{-1}\left(\frac{x_1 - ob1}{L2}\right),$$

$$\rho = \sqrt{L2^2 + (x_1 - ob1)^2}, \theta = 0 \sim 3^\circ, L1 = 4.5452 \mu\text{m}, L2 = 3 \mu\text{m}, x_1 = 0.7266 \mu\text{m},$$

$\alpha = 4.32^\circ$. *ob1* : position of observation point 1.

Figure 107 illustrates each specification and the structure to be analyzed by the Matlab code.

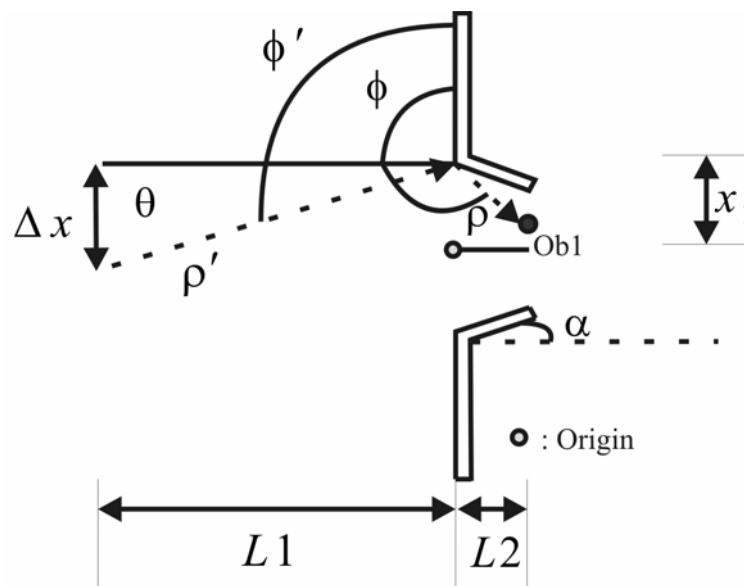


Figure 107. Geometrical specifications for the upper wedge calculation

Lower:

$$\text{TE mode, } \phi' = 90^\circ - \theta, \rho' = \sqrt{L1^2 + \Delta x^2}, \phi = 270^\circ - \tan^{-1}\left(\frac{x_2 + ob1}{L2}\right),$$

$$\rho = \sqrt{L2^2 + (x_2 + ob1)^2}, \theta = 0 \sim 3^\circ, L1 = 4.5452 \mu\text{m}, L2 = 3 \mu\text{m}, x_2 = 0.7266 \mu\text{m},$$

$\alpha = 4.32^\circ$. *ob1* : position of observation point 1

Figure 108 illustrates each specification and the structure to be analyzed according to the Matlab code.

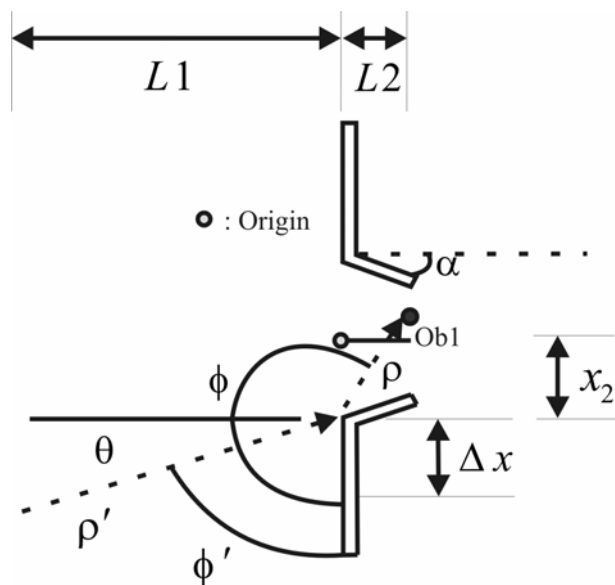


Figure 108. Geometrical specifications for the lower wedge calculation

Figure 109 is the code-scanning result of Equation 93 for the upper and lower wedges.

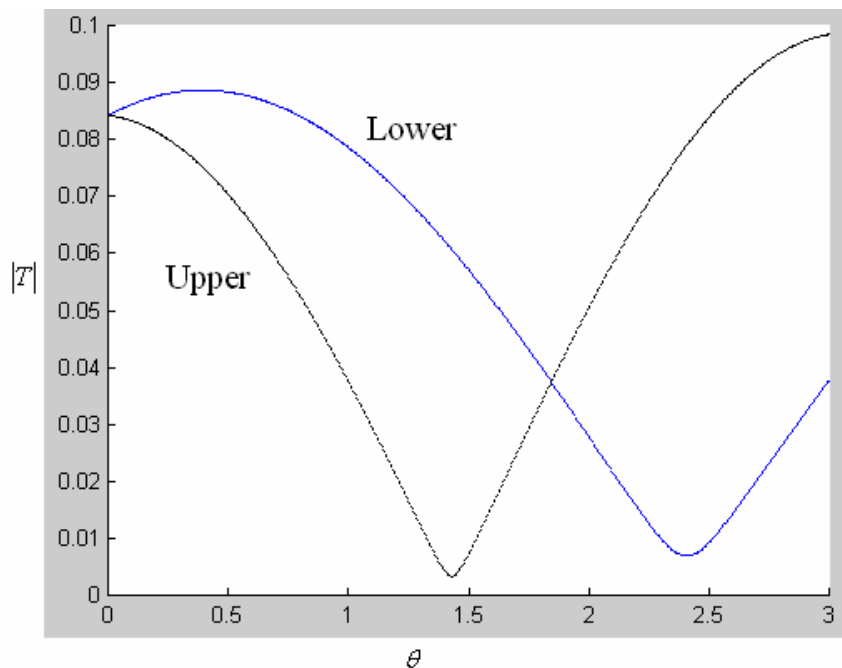


Figure 109. Matlab calculations and plot of $\theta = 0 \sim 3^\circ$ at observation point 1, Equation 93.

Figure 110 is the result for the sum of Equations 93 and 99 as illustrated in Fig. 93.

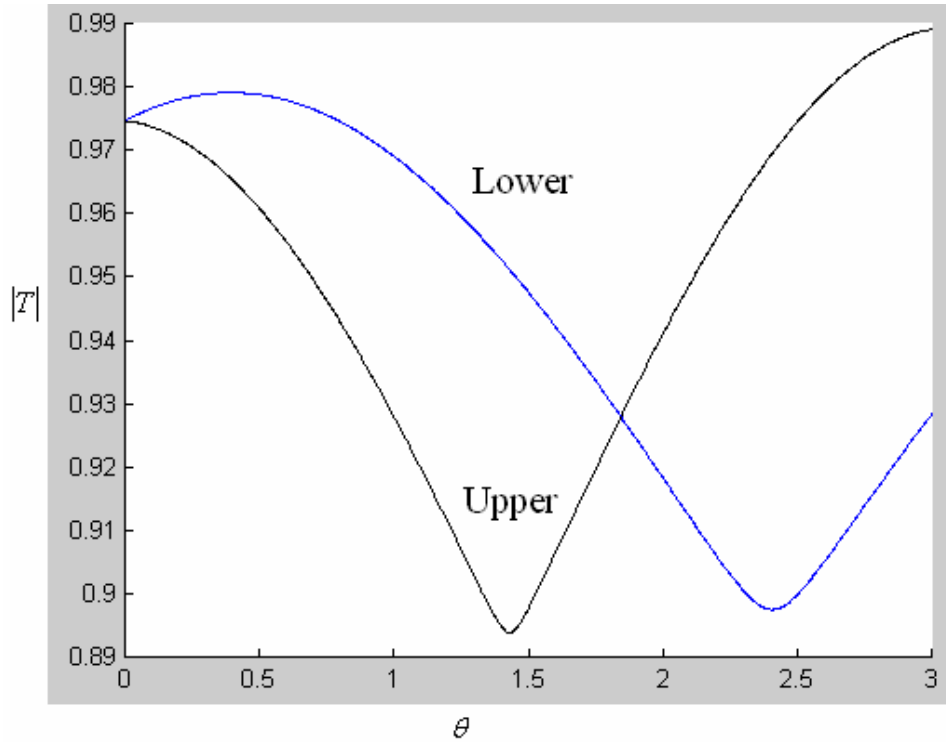


Figure 110. Matlab calculations and plot of $\theta = 0 \sim 3^\circ$ at observation point 1, the sum of Equations 93 and 99.

Because observation point 2 is related to the transmission between different mediums, I will present the results for the transmission at observation point 2 (as illustrated in Fig. 103) in the final section of this research.

5.3.3 Basic setup of the FDTD calculations

In this section, I will present results of the FDTD simulations in the range of $\theta = 0 \sim 3^\circ$. However the taken values of θ will be every 0.5° because of the much longer calculation time required for the FDTD simulations.

The specifications of the FDTD simulations are as follows:

TE mode, E_y : rectangular amplitude (as illustrated in Fig. 111), so that the amplitude is compatible with the basic assumption contained in Equation 79.

$\lambda : 0.633 \mu m$

Half width : $1.5 \mu m$

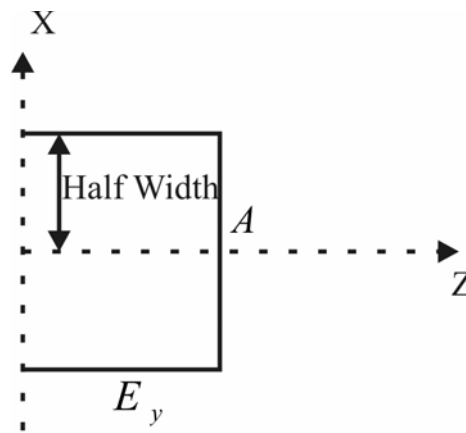


Figure 111. E_y of unit amplitude for the FDTD calculation.

Optical waveguide:

Silicon-on-insulator waveguide, $n = 3$, n : refractive index. I assume the refractive index of both the cladding and wafer to be 1.

Aperture mask:

For the material, Ag (silver) is chose in order to avoid optical penetration; therefore, there is no adjustment of the refractive index for the air and wafer (including cladding for the waveguide). Also, Ag is compatible with the silicon-on-insulator process. The definition of the Ag in question refers to the Drude model [47] in the FDTD commercial code. The Drude model of Ag is

$$\varepsilon_r(\omega) = \varepsilon_\infty + \frac{\omega_p^2}{i\Gamma\omega - \omega^2}, \quad \varepsilon_\infty: \text{permittivity at infinite frequency, 1.999.}$$

ω_p : plasma angular frequency, $1.34639 \cdot 10^{16}$ rad/s.

Γ : collision angular frequency, $9.61712 \cdot 10^{13}$ rad/s.

Figure 112 illustrates the simulation example of $\theta = 0^\circ, 1^\circ, 2^\circ$ but without the optical waveguide. The case is the same as that shown in Fig. 110.

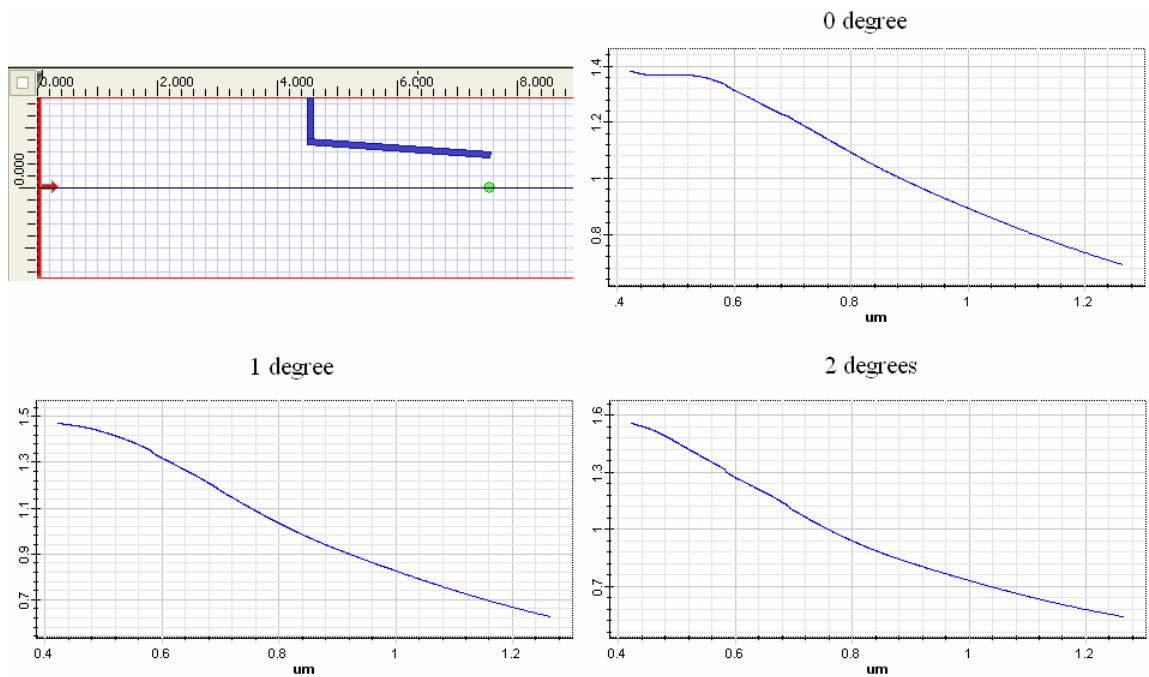


Figure 112. FDTD layout and transmission ratio in λ domain of upper spatial filter

The transmission ratios of $\lambda = 0.633\mu\text{m}$ are:

$$T(\theta = 0^\circ) = 1.28, T(\theta = 1^\circ) = 1.275, T(\theta = 2^\circ) = 1.22$$

Figure 113 illustrates the transmission ratio of the effective upper spatial filter plus the effective lower spatial filter. This transmission ratio is the one shown in Fig. 92.

The transmission ratios of $\lambda = 0.633\mu\text{m}$ are:

$$T(\theta = 0^\circ) = 2.331, T(\theta = 1^\circ) = 2.251, T(\theta = 2^\circ) = 1.945$$

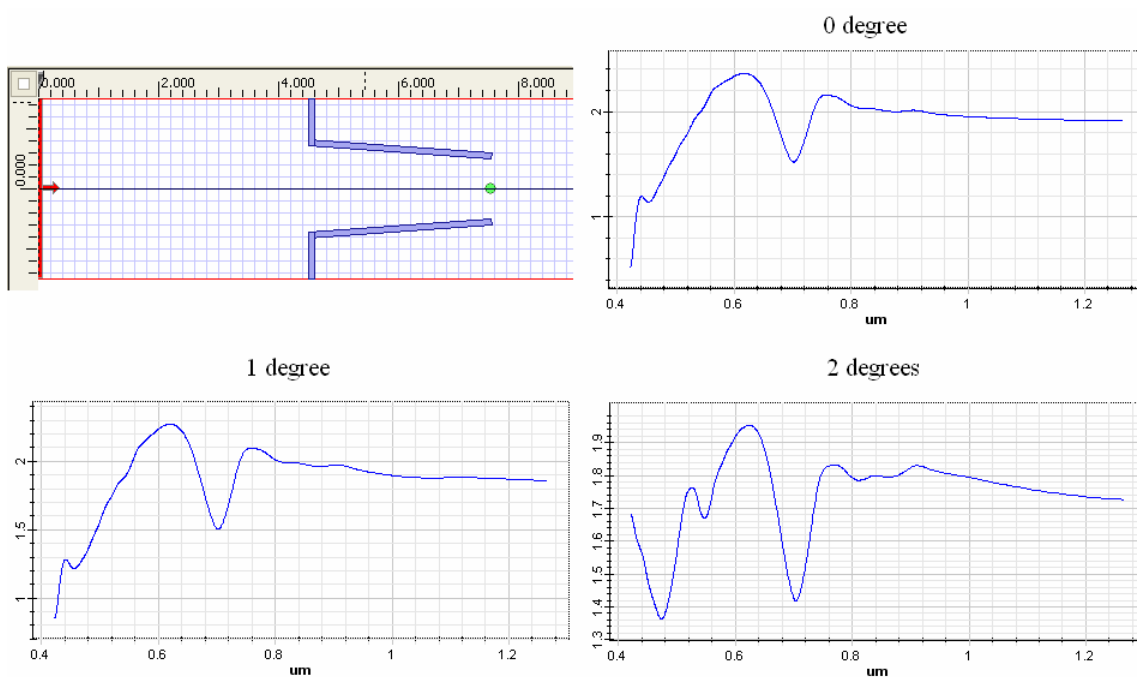


Figure 113. FDTD layout and transmission ratio in λ domain of upper and lower filters

As shown in the FDTD simulation results in the wavelength (λ) domain, E_y is not an ideal impulse located at $\lambda = 0.633\mu\text{m}$; therefore, the result at the observation point normalized to the input field will be higher than the results calculated according to the Matlab.

The transmission-ratio calculation according to the Matlab code rests on the assumption that a perfect impulse shape corresponds to the E_y of $\lambda = 0.633\mu m$.

Figure 114 illustrates the frequency response of the input field in the FDTD

$\lambda = 0.633\mu m$ is $f = 473.67THz$

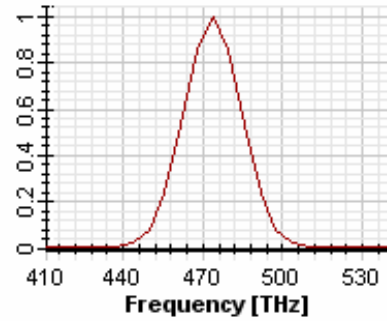


Figure 114. Frequency response of the input wave for the FDTD calculation

5.4 Comparisons, conclusions, and future works

Figure 115 is the comparison of $G_{upper\ filter} + e^{j\alpha} \cdot G_{upper\ wedge}$ in Equation 101 and Fig. 97.

The result shows that the FDTD also has the notch characteristics; however, it is not exactly at the point that the Matlab calculation predicts. Both the FDTD calculations and the Matlab calculations are based on observation point 1. The case is without optical waveguide, I arrange these simulations in order to avoid the reflection loss because of the optical waveguide.

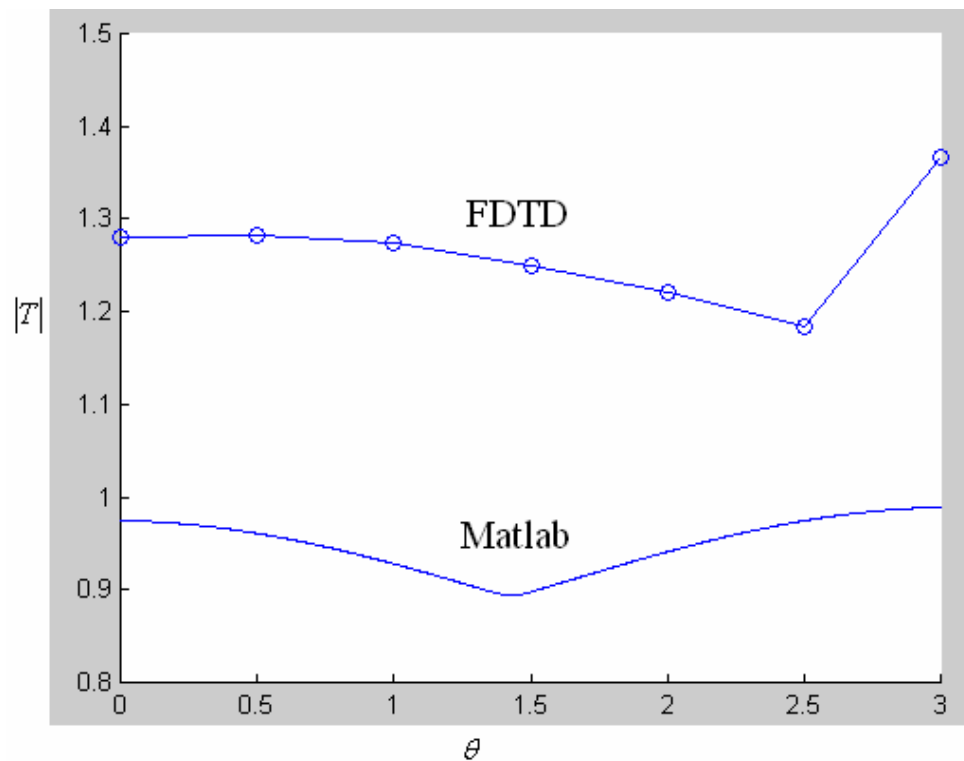


Figure 115. Matlab and FDTD calculations for Equation 101 and Fig. 97, observation point 1.

Figure 116 is a comparison of $G_{lower_filter} + e^{-j\alpha} \cdot G_{lower_wedge}$ in Equation 101 and Fig. 97.

The results from the Matlab calculations of $\theta = 0.5 \sim 1.5^\circ$ reveal a decrease of the transmission ratio and also reveal the beginnings of an increase at the region of $\theta = 2.5 \sim 3^\circ$.

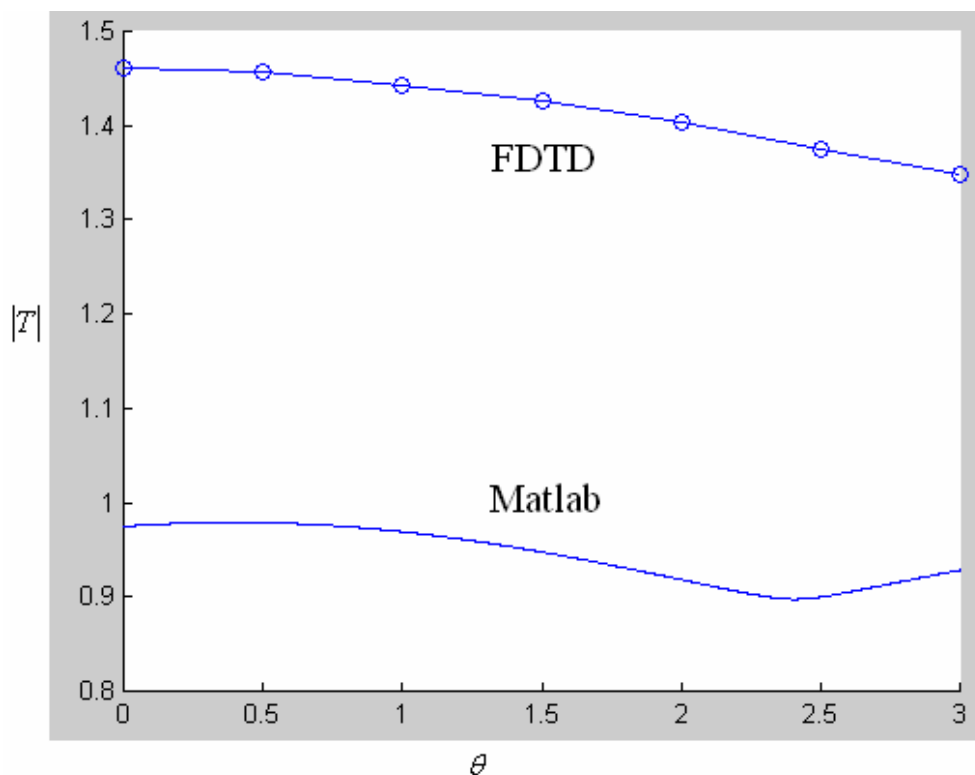


Figure 116. Matlab and FDTD calculations for Equation 101 and Fig. 97, observation point 1.

Figure 117 is the comparison of

$$T_{system} = Waveguide\ transmission \cdot (G_{upper\ filter} + G_{lower\ filter} + e^{j\alpha} \cdot G_{upper\ wedge} + e^{-j\alpha} \cdot G_{lower\ wedge})$$

in Equation 101 and Fig. 97. This comparison represents the results at observation point 2, which is the total transmission ratio of the complete spatial filter, as illustrated in Fig. 97. The calculation includes the transmission ratio of the optical waveguide under the TE mode, as shown in Fig. 118.

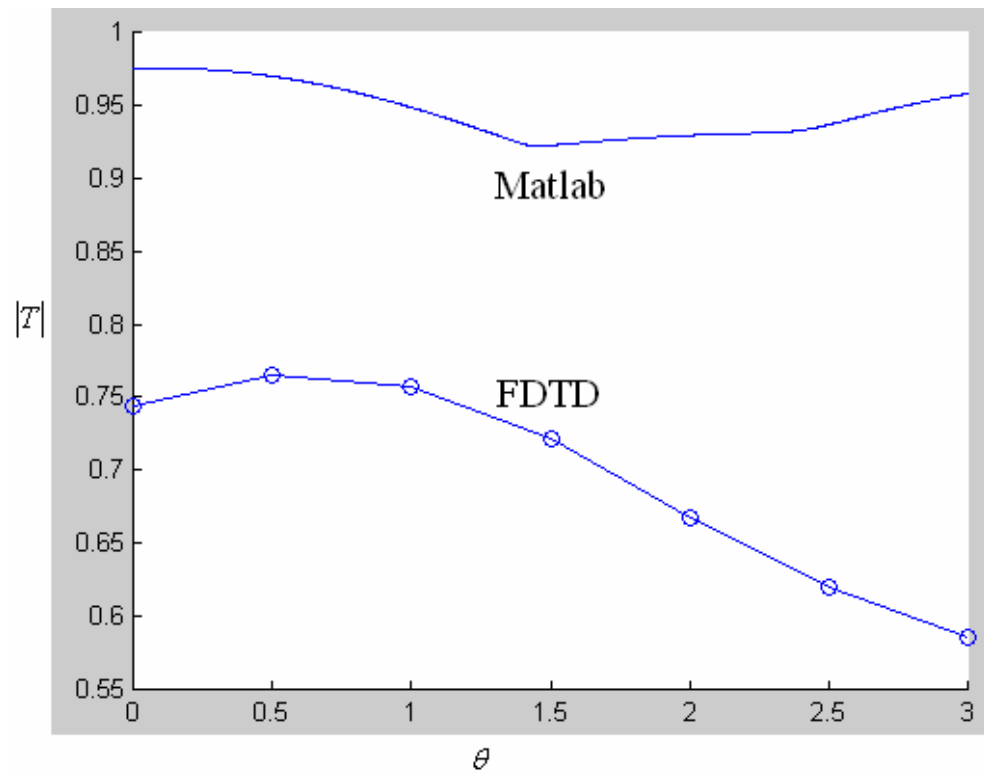


Figure 117. Matlab and FDTD calculations for Equation 101 and Fig. 97, observation point 2.

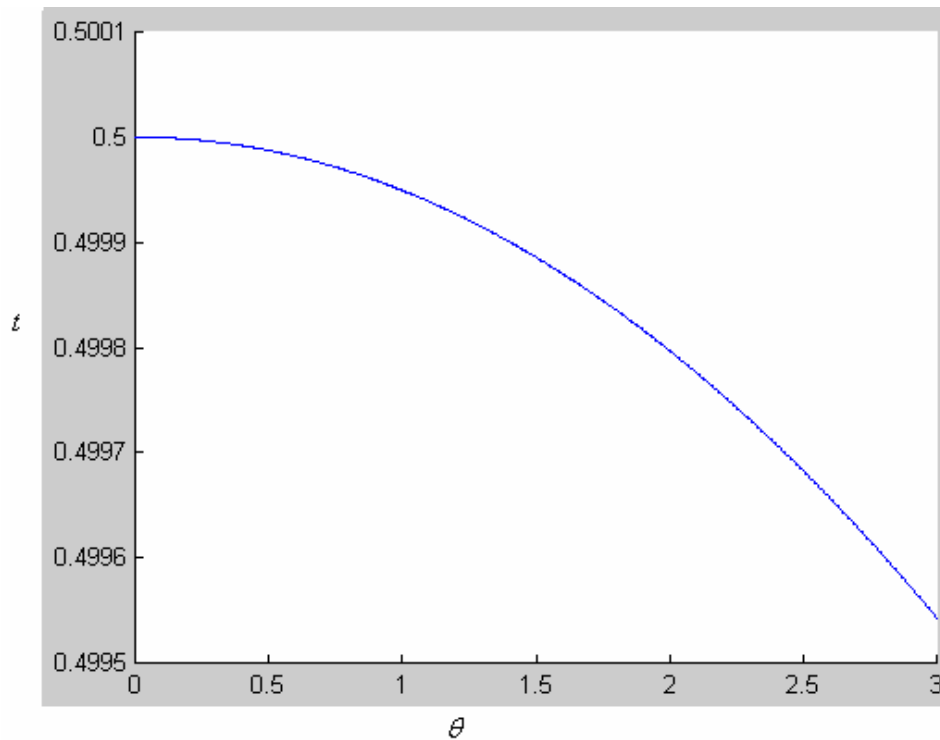


Figure 118. Matlab calculation of the optical waveguide transmission, TE mode of Equation 77.

Conclusions:

1. This research provides another calculation method for the optical pulse transmitted to the spatial filter array. The advantage of this modeling method is that it is faster than the FDTD method because the former method does not require complex calculations for other information. Also, as shown in the developed modeling method, the complete spatial filter can be implemented into one single transfer function.
2. The developed model can calculate the transmission ratio that corresponds to a spatial filter's different structural combinations.

3. As illustrated in Fig. 113, E_y is not a perfect monochromatic wave (single frequency) in the FDTD commercial code used in this research. The derivations and the developed model do not reflect the considerations regarding frequency (wavelength) swing caused by the reflection or propagation loss; therefore, the FDTD calculations' results at observation point 1 from will be higher than the Matlab calculations' results. However, the Matlab calculations' results at the observation point 2 (inside the optical waveguide) are higher than the FDTD calculations' results because optical waveguide loss is considered neither in the Matlab calculations nor in the developed model.
4. Only a small angle of the apex angle of the spatial filter is considered because the sum of the transmission ratio's principle is based on the cross-section view. Further considerations or changes in the calculations are required if the apex angle of the spatial filter is large.
5. The half width of E_y set in the FDTD is also a point in the transmission ratio calculation. The value of the half width that is set for this research is $1.5\mu m$, and the width of the optical pulse is wider than the entrance of the spatial filter. This difference is one of the reasons for the higher transmission ratio calculated by the FDTD code because E_y is not just located at one single wavelength ($0.633\mu m$).
6. The transmission ratio higher than 1 at observation point 2 from the Matlab calculation exhibits characteristics that are similar to those that correspond to the edge diffraction, and the wedge diffraction also contributes to the total transmission ratio.

7. It is possible to apply both the developed model and the calculations to the modeling of the multiple diffracting structures in wireless communication [48]. In the research concerning the multiple diffraction of wireless communication, wedge diffraction and transmission exist in the environments of complicated structures, a topic that is currently of great interest.

Research objectives accomplished:

1. Determine the design methods and existing fabrication processes for both of the spatial filter and collection optics. Silicon-on-insulator and separation implanted by the oxygen are the existing fabrication processes chosen.
2. Determine the analytical parameters and for the spatial filter and collection optics. The preliminary specifications of the spatial filter and collection optics are described in Chapter 4, and the finite-difference-time-domain method is used to calculate the transmission and crosstalk ratio of both devices.
3. Develop the analytical modeling method by applying the Fresnel-Kirchhoff diffraction, wedge diffraction, and Babinet's principle. The developed analytical model is calculated by using the Matlab software, and compared to the results by using the finite-difference-time-domain method.
4. Develop the diffraction and transmission calculation methods for the electro-optical deflector. The methods are based on the Fresnel-Kirchhoff diffraction and approximated by the numerical calculations.
5. Introduce the focusing device by using the surface plasmons.

For the future research:

1. The calculating and the modeling of complex structures, especially for the large half-apex angle of spatial filter.
2. Investigating the reflection and the waveguide propagation loss for the related calculations.
3. Developing alternative derivations and calculations (In appendix A, I present another derivation and Matlab calculation for the transmission ratio of the electro-optical deflector output. The calculations are similar to those contained in Equations 79 through 90, despite a change in the refractive index).
4. Reflection consideration for the electro-optical deflector and the spatial filter. Both of these devices are composed of different mediums.
5. Developing a mechanism that lowers the crosstalk effect. (In appendix B, I introduce the possible focusing unit [49] for spatial filter array in order to lower the crosstalk effect, as described in Chapter 4.)

Appendix A. Diffraction coefficients calculations of electro-optical deflector and surface plasmons

Figure A1 illustrates the diffracted electric field from P_1 to P_2 , and the electric field is the same as Equation 79

$$E = \frac{j \cdot k \cdot A}{4\pi \cdot r_1 \cdot r_2} [(\hat{n} \cdot \hat{r}_2) - (\hat{n} \cdot \hat{r}_1)] \cdot \int_S e^{-j \cdot k \cdot (R_1 + R_2)} dS', \quad A: \text{constant} \quad (\text{A.1})$$

The electric field propagates from P_1 to P_2 without the aperture

$$E_0 = A \cdot \frac{e^{-j \cdot k \cdot (r_1 + r_2)}}{r_1 + r_2} \quad (\text{A.2})$$

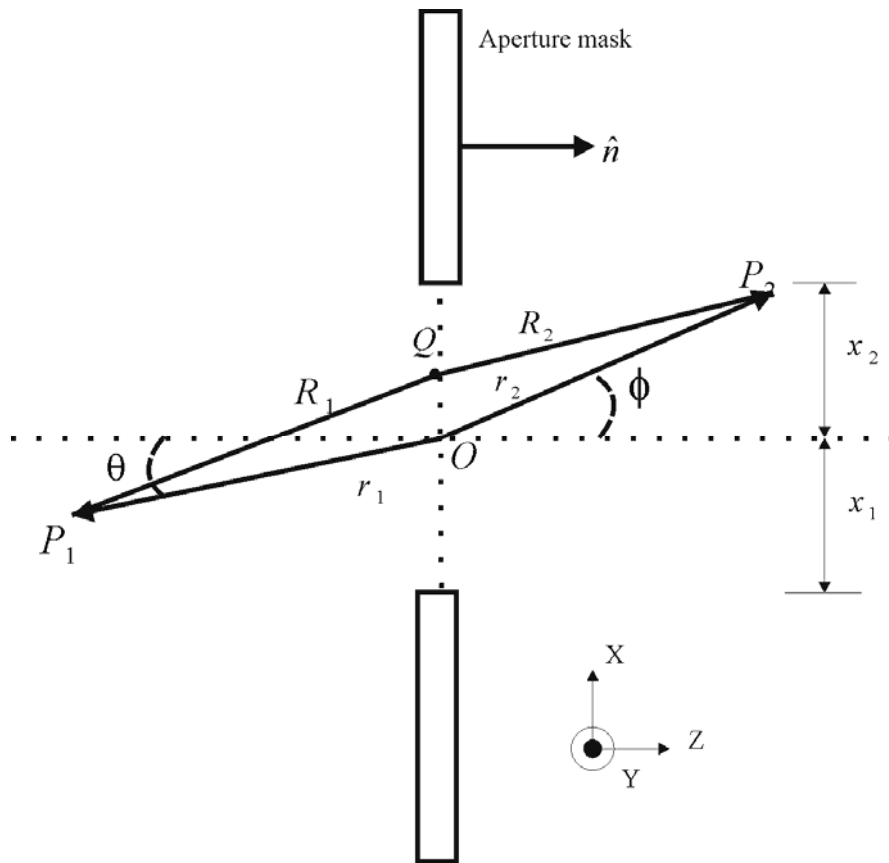


Figure A1. Kirchhoff-Fresnel Diffraction

The diffraction coefficient is defined as Equations A.1 divided by A.2

$$D = \frac{E}{E_0} = \frac{j \cdot k}{4\pi \cdot L} [(\hat{n} \cdot \hat{r}_2) - (\hat{n} \cdot \hat{r}_1)] \cdot \int_S e^{-j \cdot k \cdot (R_1 + R_2 - r_1 - r_2)} dS' \quad (\text{A.3})$$

$$R_1 = r_1 - \hat{r}_1 \cdot r' + \frac{1}{2r_1} \cdot [r' \cdot r' - (\hat{r}_1 \cdot r')^2], \quad R_2 = r_2 - \hat{r}_2 \cdot r' + \frac{1}{2r_2} \cdot [r' \cdot r' - (\hat{r}_2 \cdot r')^2]$$

L is defined as the focal length

$$\frac{1}{L} = \frac{1}{r_1} + \frac{1}{r_2} \quad (\text{A.4})$$

The coordinates system will be changed because of the different mediums as shown in Fig. A2

$$n_1 \cdot \sin \theta = n_2 \cdot \sin \phi, \quad n_2 = 1, \quad \therefore \sin \phi = n_1 \sin \theta$$

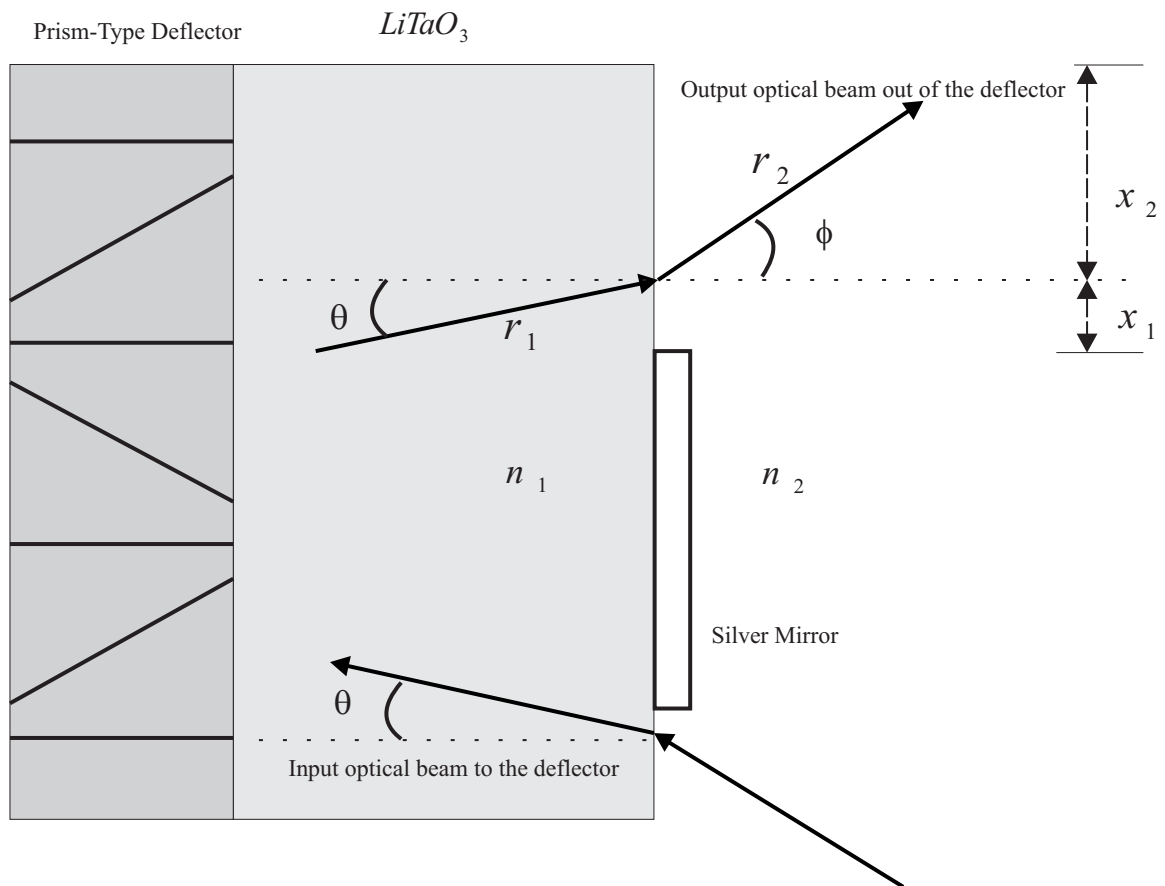


Figure A2. Illustration of Kirchhoff-Fresnel diffraction to be applied to the deflector

For the single medium

$$\sin \phi = \sin \theta, \quad \phi = \theta$$

The factors in the Equation A.3 are calculated as followings

$$\begin{aligned} \hat{r}_1 &= -\hat{z} \cos \theta - \hat{x} \sin \theta, \quad \hat{r}_2 = \hat{z} \cos \phi + \hat{x} \sin \phi = \hat{z} \cos \phi + \hat{x} \cdot n_1 \cdot \sin \theta, \quad r' = x' \cdot \hat{x} + y' \cdot \hat{y} \\ -(\hat{r}_1 + \hat{r}_2) \cdot r' &= -(-\hat{z} \cos \theta - \hat{x} \sin \theta + \hat{z} \cos \phi + \hat{x} \cdot n_1 \cdot \sin \theta) \cdot (x' \cdot \hat{x} + y' \cdot \hat{y}) \\ &= (1 - n_1) \cdot x' \sin \theta \end{aligned} \quad (\text{A.5})$$

For the case of $n_1 = 1$, Equation A.5 will be

$$-(\hat{r}_1 + \hat{r}_2) \cdot r' = -(-\hat{z} \cos \theta - \hat{x} \sin \theta + \hat{z} \cos \phi + \hat{x} \cdot 1 \cdot \sin \theta) \cdot (x' \cdot \hat{x} + y' \cdot \hat{y}) = 0$$

Continue the derivations for Equation A.3

$$\frac{(\hat{r}_1 \cdot r')^2}{r_1} = \frac{1}{r_1} [(-\hat{z} \cos \theta - \hat{x} \sin \theta) \cdot (x' \hat{x} + y' \hat{y})]^2 = \frac{1}{r_1} (x')^2 \sin^2 \theta \quad (\text{A.6})$$

$$\frac{(\hat{r}_2 \cdot r')^2}{r_2} = \frac{1}{r_2} [(\hat{z} \cos \phi + \hat{x} \cdot n_1 \cdot \sin \theta) \cdot (x' \hat{x} + y' \hat{y})]^2 = \frac{1}{r_2} (x')^2 \cdot n_1^2 \cdot \sin^2 \theta$$

Combine Equations A.5 and A.6, the factor of the exponential function in Equation A.3

becomes

$$\begin{aligned} \therefore R_1 + R_2 - r_1 - r_2 &= -(\hat{r}_1 + \hat{r}_2) \cdot r' + \frac{1}{2} \left[\left(\frac{1}{r_1} + \frac{1}{r_2} \right) \cdot r' \cdot r' - \frac{(\hat{r}_1 \cdot r')^2}{r_1} - \frac{(\hat{r}_2 \cdot r')^2}{r_2} \right] \\ &= (1 - n_1) \cdot x' \sin \theta + \frac{1}{2} \left\{ \frac{1}{L} [(x')^2 + (y')^2] - \frac{(x')^2}{r_1} \sin^2 \theta - \frac{n_1^2 \cdot (x')^2}{r_2} \sin^2 \theta \right\} \end{aligned} \quad (\text{A.7})$$

Assume $r_1 = r_2$, and the vectors $\hat{r}_1 \neq -\hat{r}_2$. The Equation A.7 is written as

$$\therefore R_1 + R_2 - r_1 - r_2 = (1 - n_1) \cdot x' \sin \theta + \frac{1}{2} \left\{ \frac{1}{L} [(x')^2 + (y')^2] - \frac{(x')^2}{r_2} \cdot (1 + n_1^2) \cdot \sin^2 \theta \right\} \quad (\text{A.8})$$

For 2-dimensional calculation, consider x term only. Equation A.8 is written as

$$\therefore R_1 + R_2 - r_1 - r_2 = (1 - n_1) \cdot x' \sin \theta + \frac{1}{2L} (x')^2 - \frac{(1 + n_1^2)}{4L} \cdot (x')^2 \cdot \sin^2 \theta \quad (\text{A.9})$$

From Equation A.5, we have

$$\hat{n} = \hat{z}, \quad \hat{n} \cdot \hat{r}_2 = \hat{z} \cdot (\hat{z} \cos \phi + \hat{x} \sin \phi) = \cos \phi, \quad \hat{n} \cdot \hat{r}_1 = \hat{z} \cdot (-\hat{z} \cos \theta - \hat{x} \sin \theta) = -\cos \theta$$

There is another change of coordinates system on the basis of different mediums

$$\cos \phi = \cos[\sin^{-1}(n_1 \sin \theta)]$$

Therefore the diffraction coefficient of Equation A.3 can be written as

$$D = \frac{jk(\cos \phi + \cos \theta)}{4\pi L} \int_{-x_1}^{x_2} \int_{-y_1}^{y_2} e^{-jk(\frac{y'^2}{2L} + \alpha)} dx dy \quad (\text{A.10})$$

$$\alpha = R_1 + R_2 - r_1 - r_2 = (1 - n_1) \cdot x' \sin \theta + \frac{1}{2L} (x')^2 - \frac{(1 + n_1^2)}{4L} \cdot (x')^2 \cdot \sin^2 \theta,$$

$$\cos \phi = \cos[\sin^{-1}(n_1 \sin \theta)]$$

In the 2-dimensional calculation, let $y' = -\infty \sim \infty$,

$$\int_{-y_1}^{y_2} e^{-jk\frac{y'^2}{2F}} dy = [F(y_2) - F(-y_1)] = [F(y_2) + F(y_1)] = \frac{1-j}{2} + \frac{1-j}{2} = 1-j$$

$$F(y) = C(y) - iS(y) = \int_0^y e^{-j(\pi/2)u^2} du, \quad u = \sqrt{\frac{k}{\pi F}} \cdot y', \quad F(\infty) = \frac{1-j}{2}$$

If the case is $r_1 \neq r_2$ and $\hat{r}_1 \neq -\hat{r}_2$, Equation A.10 can be written as

$$D = \frac{jk(\cos \phi + \cos \theta)}{4\pi L} \cdot (1-j) \cdot \int_{-x_1}^{x_2} e^{-jk\alpha} dx \quad (\text{A.11})$$

$$\alpha = (1 - n_1) \cdot x' \sin \theta + \frac{1}{2} \left\{ \frac{1}{L} [(x')^2] - \frac{(x')^2}{r_1} \sin^2 \theta - \frac{n_1^2 \cdot (x')^2}{r_2} \sin^2 \theta \right\},$$

$$\cos \phi = \cos[\sin^{-1}(n_1 \sin \theta)]$$

The results derived in Equations A.10 and A.11 cannot be simplified as the closed form by using the Fresnel integrals, and the closed form is already shown in Chapter 5.

Therefore the Riemann Sum [50] of numerical method is used

$$\int_a^b f(x)dx = \frac{b-a}{n} \sum_{m=0}^{n-1} f(x_m) \quad (\text{A.12})$$

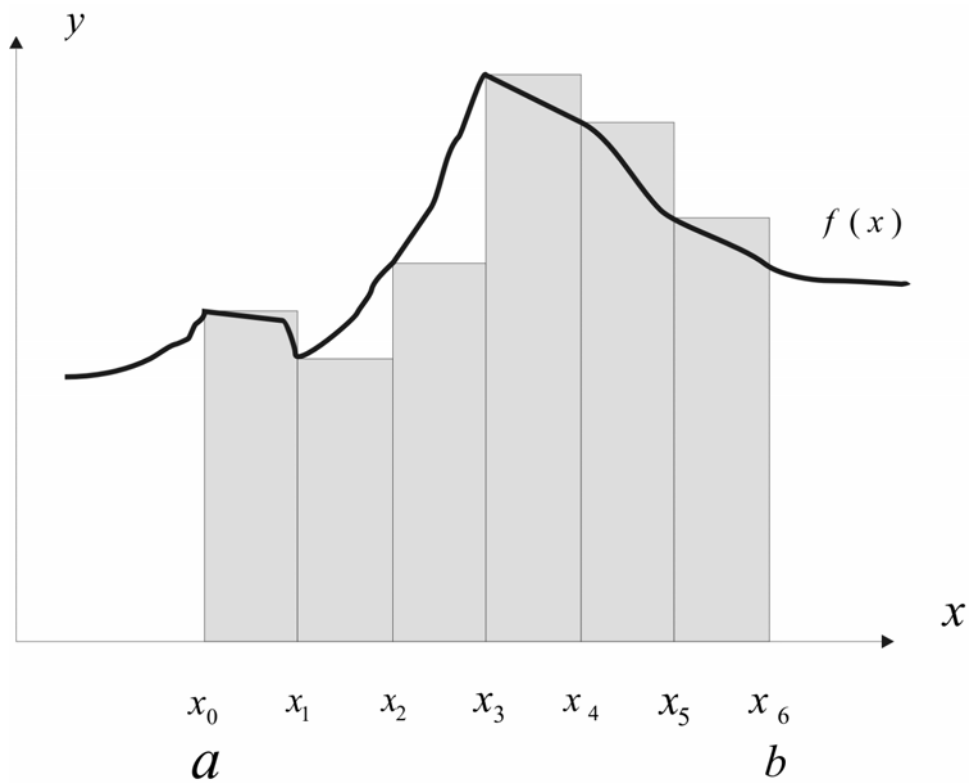


Figure A3. Riemann sum method to calculate the integral of $f(x)$

Also, there are no ∞ and $-\infty$ defined in Matlab code. Therefore the calculation sets a large value of the upper opening: $x_2 \gg x_1$.

The oscillation of the results has the same characteristics as the Fresnel integrals described in Chapter 5. Figures A4 and A5 follow the circular scanning contour as illustrated in Fig. 101.

The specifications of the calculations are

$$r_1 = 10 \mu m, r_2 = 20 \mu m, x_1 = 3 \mu m, x_2 = 10 \mu m, n_1 = 1, n_2 = 1$$

$$n_1 = 1, n_2 = 1: \text{refractive index of air, } \lambda = 0.633 \mu m.$$

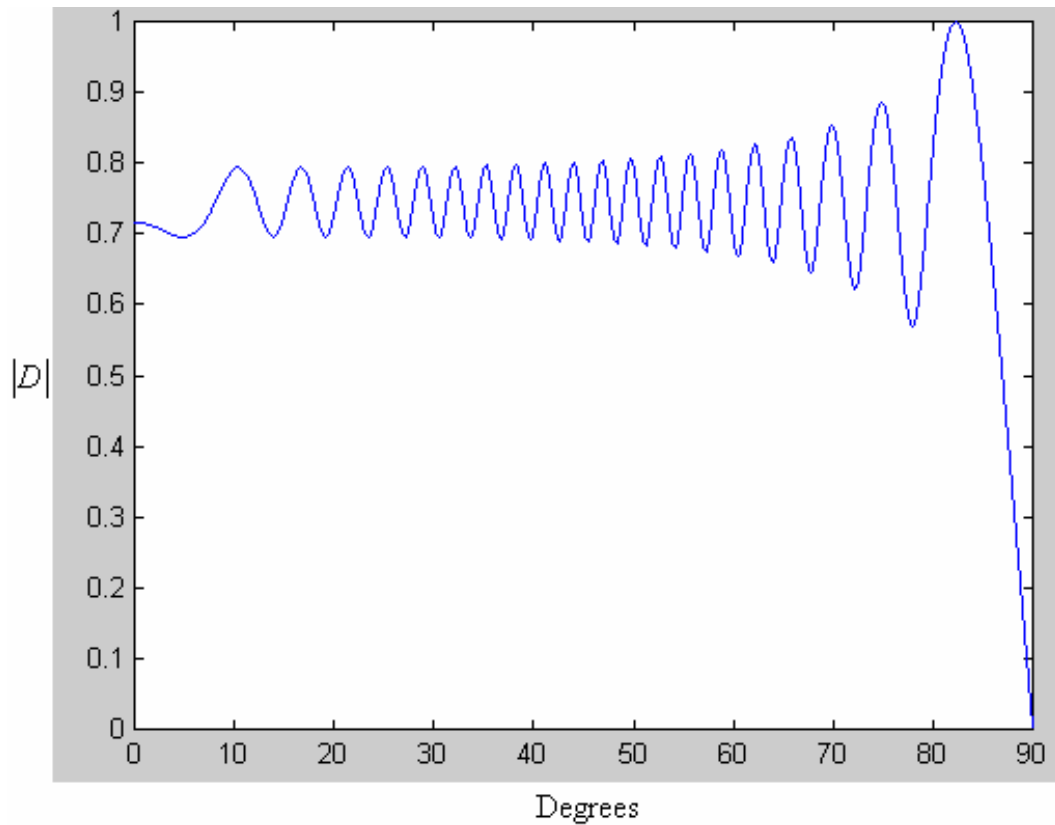


Figure A4. Calculation results of the edited Matlab code for the case of $n_1 = 1, n_2 = 1$.

Figure A5 is the case of deflection angle of $\theta = 18^\circ \sim 22^\circ$ as illustrated in Fig. A2. The case assumes 1-degree deflection per analog arbitrary unit voltage, and the reference axis of zero voltage deflection is 20 degrees. The specifications of the calculations are

$$r_1 = 10 \mu\text{m}, r_2 = 20 \mu\text{m}, x_1 = 3 \mu\text{m}, x_2 = 10 \mu\text{m}, n_1 = 2.18, n_2 = 1$$

$n_1 = 2.18$: refractive index of LiTaO_3 , $n_2 = 1$: refractive index of air, $\lambda = 0.633 \mu\text{m}$.

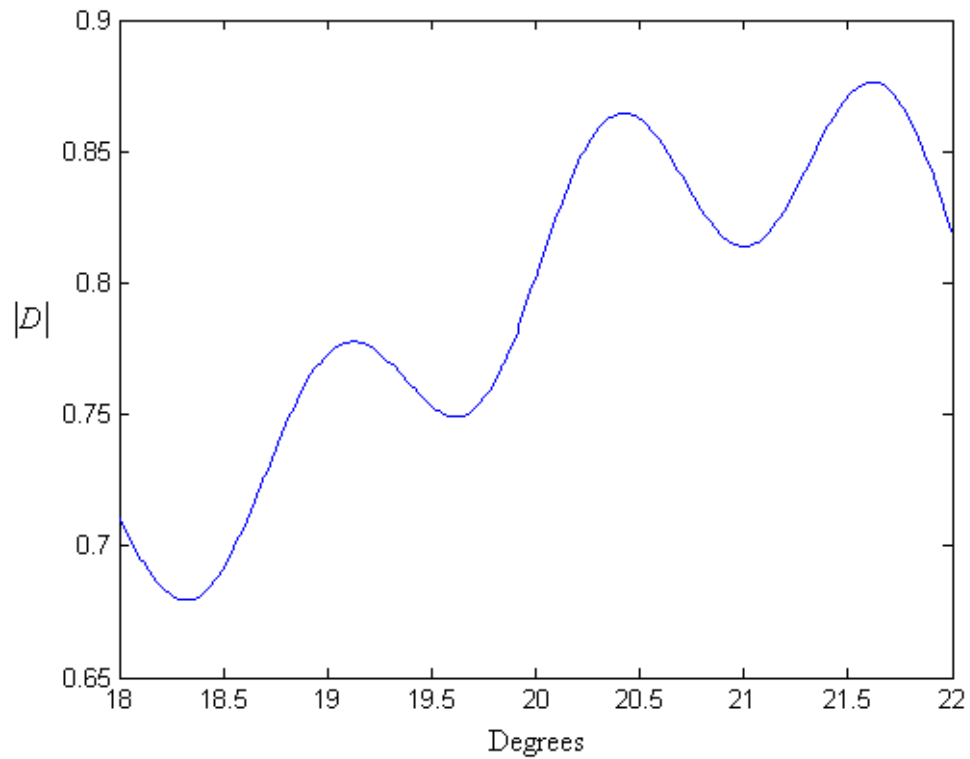


Figure A5. Diffraction coefficient of 18~22 degrees for the deflector

As the simulation results in Chapter 4.2, the crosstalk effect will limit the performance of the spatial filter array. One of the possible solutions to this problem is a focusing unit for the spatial filter array. In this appendix, an example of the focusing unit will be shown.

Figure A6 illustrates an array of the nano holes deposited on the SiO_2 substrate. This device is often used in the field called “surface plasmons [51]”. As shown in Fig. A6, surface plasmons are used in the focusing unit. The simulation example in Fig. 9 (b) shows the pulse width of $5\mu m$ is focused to be $2\mu m$. The device of surface plasmons is a potential area to be investigated, and most applications are aimed to enhance the nano-scale optical transmission [52].

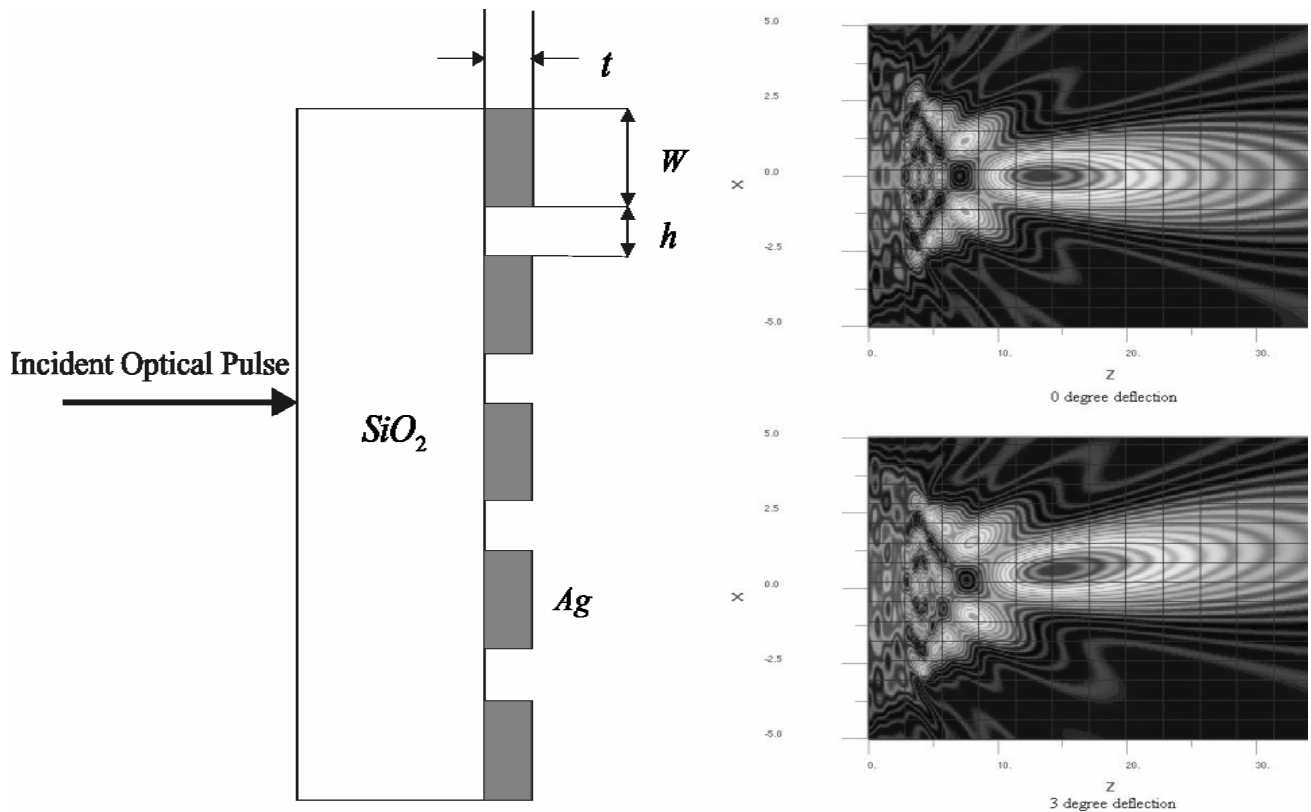


Figure A6. Surface Plasmons design and FDTD simulation of $\theta = 0^\circ, 3^\circ$. $W = 400nm, h = 80nm, t = 20nm$

Appendix B. Diffraction coefficients calculations of tilted aperture

In this section, I derive another representation of the diffraction coefficient for the tilted structure that is illustrated in Fig. A7. The derivations also start from the diffracted electric field that is already described at previous section and Equation 79:

$$D = \frac{E}{E(P_2 \sim P_1)} = \frac{j \cdot k}{4\pi \cdot L} [(\hat{n} \cdot \hat{r}_2) - (\hat{n} \cdot \hat{r}_1)] \cdot \int_S e^{-j \cdot k \cdot (R_1 + R_2 - r_1 - r_2)} dS'$$

There is a change of the variable $\hat{n}_{new} \cdot \hat{r}_2$, the new direction vector because of change of the half apex angle as illustrated in Fig. 57.

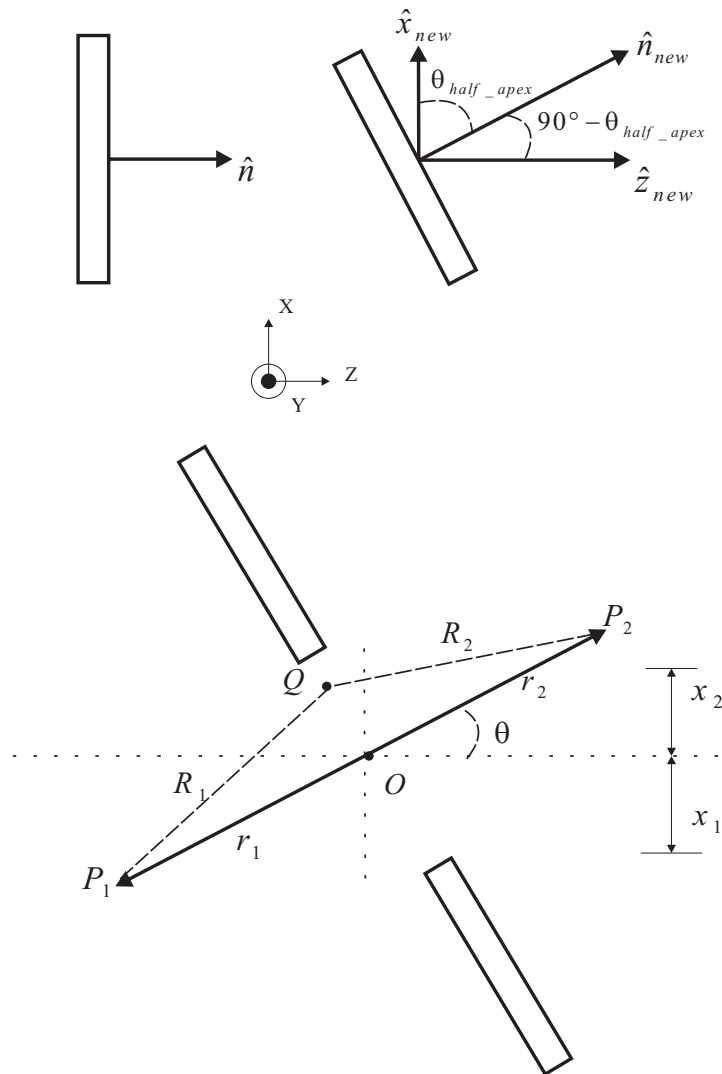


Figure A7. Kirchhoff-Fresnel diffraction of tilted structure

Therefore

$$\begin{aligned}\hat{n}_{new} \cdot \hat{r}_2 &= [\hat{x} \cos \theta_{half_apex} + \hat{z} \cos(90^\circ - \theta_{half_apex})] \cdot [\hat{z} \cos \theta + \hat{x} \sin \theta] \\ &= \cos \theta \cdot \sin \theta_{half_apex} + \sin \theta \cdot \cos \theta_{half_apex} \\ &= \sin(\theta_{half_apex} + \theta)\end{aligned}$$

$$\begin{aligned}\hat{n}_{new} \cdot \hat{r}_1 &= [\hat{x} \cos \theta_{half_apex} + \hat{z} \cos(90^\circ - \theta_{half_apex})] \cdot [-\hat{z} \cos \theta - \hat{x} \sin \theta] \\ &= -\cos \theta \cdot \sin \theta_{half_apex} - \sin \theta \cdot \cos \theta_{half_apex} \\ &= -\sin(\theta_{half_apex} + \theta)\end{aligned}$$

For two special cases

$$\theta_{half_apex} = 0^\circ \Rightarrow \hat{n}_{new} \cdot \hat{r}_2 = \sin \theta,$$

$$\theta_{half_apex} = 90^\circ \Rightarrow \hat{n}_{new} \cdot \hat{r}_2 = \sin(90^\circ + \theta) = \cos \theta,$$

$$\theta_{half_apex} = 90^\circ \text{ is the original case, that is, } \hat{n} \cdot \hat{r}_2 = \cos \theta.$$

By combining the results in Equations 83 and $\hat{n}_{new} \cdot \hat{r}_2$ that was just derived, the new diffraction coefficient D_{new} to be calculated in this appendix is

$$D_{new} = \frac{j \cdot k \cdot \sin(\theta_{half_apex} + \theta)}{2\pi \cdot L} \cdot \int_{-x_1}^{x_2} \int_{-y_1}^{y_2} e^{-jk[(x')^2 \cos^2 \theta + (y')^2]} /_{2L} dy' dx' \quad (\text{A.13})$$

For y' term

$$\int_{-y_1}^{y_2} e^{-jk(y')^2} /_{2L} dy' = \sqrt{\frac{\pi \cdot L}{k}} \cdot \int_{-u_1}^{u_2} e^{-j\frac{\pi}{2}u^2} du, \quad u = \sqrt{\frac{k}{\pi \cdot L}} \cdot y'.$$

By using the Fresnel integral, $F(x) = C(x) - j \cdot S(x) = \int_0^x e^{-j\frac{\pi}{2}x^2} dx$, the y' term becomes

$$\sqrt{\frac{\pi \cdot L}{k}} \cdot \int_{-u_1}^{u_2} e^{-j\frac{\pi}{2}u^2} du = \sqrt{\frac{\pi \cdot L}{k}} \cdot [F(u_2) - F(-u_1)] = \sqrt{\frac{\pi \cdot L}{k}} \cdot [F(u_2) + F(u_1)].$$

For 2-dimensional calculations, let $u_2 = \infty$ and $u_1 = \infty$. Therefore

$$\sqrt{\frac{\pi \cdot L}{k}} \cdot [F(u_2) + F(u_1)] = \sqrt{\frac{\pi \cdot L}{k}} \cdot (1 - j).$$

For x' term

$$\int_{-x_1}^{x_2} e^{-jk[(x')^2 \cos^2 \theta] / 2L} dx' = \sqrt{\frac{\pi \cdot L}{k}} \cdot \frac{1}{\cos \theta} \cdot \int_{-v_1}^{v_2} e^{-j\frac{\pi}{2}v^2} dv, \quad v = \sqrt{\frac{k}{\pi \cdot L}} \cdot x' \cdot \cos \theta.$$

By using the Fresnel integral, $F(x) = C(x) - j \cdot S(x) = \int_0^x e^{-j\frac{\pi}{2}x^2} dx$, the x' term becomes

$$\sqrt{\frac{\pi \cdot L}{k}} \cdot \frac{1}{\cos \theta} \cdot \int_{-v_1}^{v_2} e^{-j\frac{\pi}{2}v^2} dv = \sqrt{\frac{\pi \cdot L}{k}} \cdot \frac{1}{\cos \theta} \cdot [F(v_2) - F(-v_1)] = \sqrt{\frac{\pi \cdot L}{k}} \cdot \frac{1}{\cos \theta} \cdot [F(v_2) + F(v_1)]$$

The diffraction coefficient D_{new} can be written as

$$\begin{aligned} D_{new} &= \frac{j \cdot k \cdot \sin(\theta_{half_apex} + \theta)}{2\pi \cdot L} \cdot \int_{-x_1}^{x_2} \int_{-y_1}^{y_2} e^{-jk[(x')^2 \cos^2 \theta + (y')^2] / 2L} dy' dx' \\ &= \frac{j \cdot k \cdot \sin(\theta_{half_apex} + \theta)}{2\pi \cdot L} \cdot \sqrt{\frac{\pi \cdot L}{k}} \cdot (1 - j) \cdot \sqrt{\frac{\pi \cdot L}{k}} \cdot \frac{1}{\cos \theta} \cdot [F(v_2) + F(v_1)] \quad (\text{A.13}) \\ &= \frac{1}{1 - j} \cdot \frac{\sin(\theta_{half_apex} + \theta)}{\cos \theta} \cdot [F(v_2) + F(v_1)] \end{aligned}$$

For the case of $\theta_{half_apex} = 90^\circ \Rightarrow \sin(90^\circ + \theta) = \cos \theta$, we can have

$$D_{new} = D = \frac{1}{1 - j} \cdot [F(v_2) + F(v_1)].$$

The specifications of the calculations for Equation A13 by using Matlab are

$$r_1 = 4.5452 \mu m, r_2 = 3 \mu m, x_1 = 0.7266 \mu m, x_2 = 0.7266 \mu m, \theta_{half_apex} = 4.32^\circ,$$

$$\lambda = 0.633 \mu m.$$

For the results plot in Fig. A8, the scanning variables Degrees is $\theta = 0 \sim 3^\circ$, and the scanning contour is the same as Fig. 102 (linear contour).

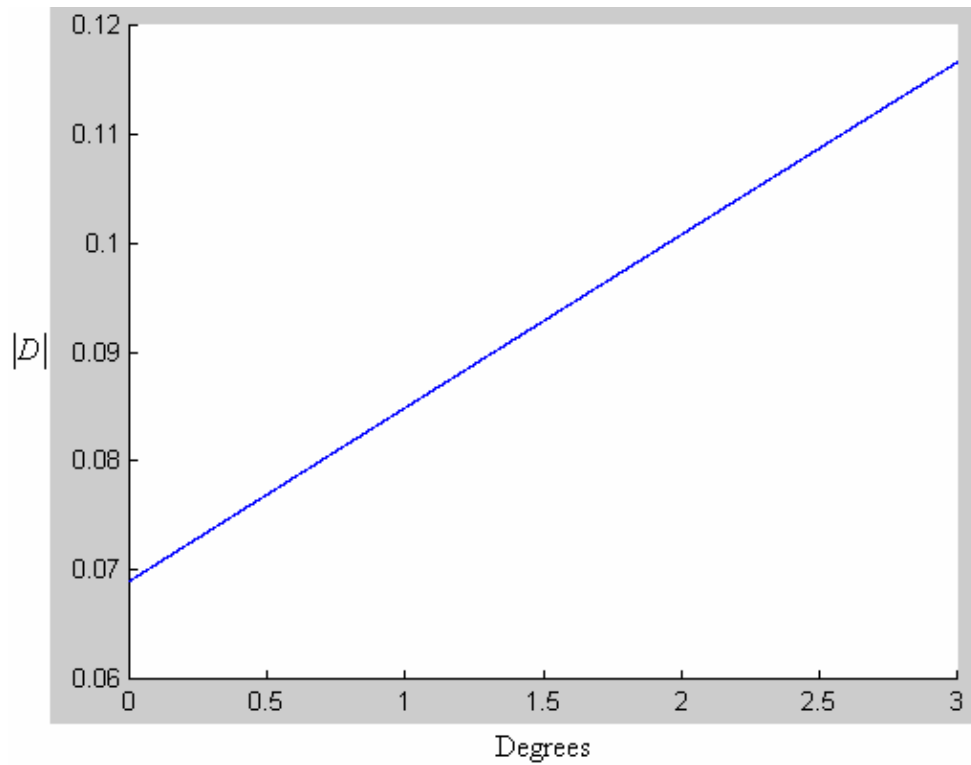


Figure A8. Calculations of Equation A13.

REFERENCES LIST

- [1] B. Sklar, *Digital Communications*. Prentice-Hall, 1988.
- [2] William L. Bahn, Engineering Modeling and Methods in C. Available at:
<http://web.uccs.edu/wbahn/ECE1021/2004FAL/HOMEWORK/hwB.htm>
- [3] J. G. Proakis and D. Manolakis, *Digital Signal Processing: Principles, Algorithms and Applications*. Prentice-Hall, 1996.
- [4] 10-bit Digital Temperature Sensor and 8-Channel ADC, Analog Devices Inc., MA, USA.
- [5] P. Vancorenland, P. Coppejans, W. D. Cock, P. Leroux, and M. Steyaert, "Optimization of a Fully Integrated Low Power CMOS GPS Receiver," *IEEE/ACM International Conference on Computer Aided Design*, pp. 10-14, Nov. 2002.
- [6] E. Spence, "Low Cost, Low Power Devices for HDSL Applications," Analog Devices Inc., MA, USA.
- [7] 14-bit 250Ksps PulSAR ADC, Analog Devices Inc., MA, USA, 2004.
- [8] T. Renkoski, W. R. Yang, J. Gahl, and W. C. Nunnally, "Integrated EOADC with spatial filter," in *Proc. 7th Joint Conference on Information Sciences (JCIS 2003)*, pp. 1410-1413, 2003.
- [9] Y. Tsunoda and J. W. Goodman, "Combined Optical AD Conversion and Page Composition for Holographic Memory Applications," *Applied Optics*, Vol. 16, No. 10, pp. 2607-2609, Oct. 1977.
- [10] C. T. Chen, *System and Signal Analysis*, Saunders Pub., 2nd edition, 1989.

- [11] Application Note 1870, Maxim semiconductor, January 31, 2003. Available at: www.maxim-ic.com/an1870.
- [12] E. Siragusa and I. Galton, "A Digitally Enhanced 1.8-V 15-bit 40-Msamp/s CMOS Pipelined ADC," *IEEE Journal of Solid-State Circuits*, Vol. 39, No. 12, pp. 2126-2138, Dec. 2004.
- [13] M. Choe, B. Song, and K. Bacrania, "An 8-bit 100-Msamples/s CMOS Pipelined Folding ADC," *IEEE Journal of Solid-State Circuits*, Vol. 36, No. 2, pp. 184-194, Feb. 2004.
- [14] G. Leger, E. J. Peralias, A. Rueda, and J. L. Huertas, "Impact of Random Channel Mismatch on the SNR and SFDR of Time-Interleaved ADCs," *IEEE Transactions on Circuits and Systems-I: Regular Papers*, Vol. 51, No. 1, pp. 140-150, Jan. 2004.
- [15] Frequency Domain Measurement Fundamentals, National Instruments. Available at: <http://zone.ni.com/devzone/conceptd.nsf/webmain/>
- [16] R. H. Walden, "Analog-to-Digital Converter Survey and Analysis," *IEEE Journal on Selected Areas in Communication*, Vol. 17, No. 4, pp. 539-550, April 1999.
- [17] B. L. Shoop, *Photonic Analog-to-Digital Conversion*. Springer, 2001.
- [18] Application Note 2094, Maxim semiconductor, June 02, 2003. Available at: www.maxim-ic.com/an2094.
- [19] Application Note 810, Maxim semiconductor, October 02, 2001. Available at: www.maxim-ic.com/an810.
- [20] P. Rabiei and A. F. J. Levi, "Analysis of Hybrid Optoelectronic WDM ADC," *IEEE Journal of Lightwave Tech.*, Vol. 18, No. 9, pp. 1264-1270, Sept. 2000.

- [21] S. Oda and A. Maruta, "A Novel Quantization Scheme by Slicing Supercontinuum Spectrum for All-Optical Analog-to-Digital Conversion," *IEEE Photonics Tech. Letters*, Vol. 17, No. 2, pp. 465-467, Feb. 2005.
- [22] G. R. Fowles, *Introduction to Modern Optics*. 2nd Edition, Dover Inc., 1989.
- [23] K. Okamoto, *Fundamentals of Optical Waveguides*, Academic Press, 2000.
- [24] C. A. Balanis, *Advanced Engineering Electromagnetics*. Wiley, 1989.
- [25] F. L. Pedrotti, S. J. Leno S. Pedrotti, *Introduction to Optics*. 2nd Edition, Prentice Hall, 1993.
- [26] A. Sakai, T. Fukazawa, and T. Baba, "Low Loss Ultra-Small Branches in a Silicon Photonic Wire Waveguide," *IEICE Trans. Electro.*, Vol. E85-C, No. 4, pp. 1033-1038, April 2002.
- [27] Matlab Version 7.0.4, Mathworks Inc..
- [28] B. Jalali, S. Yegnanarayanan, T. Yoon, T. Yoshimoto, I. Rendina, F. Coppinger, "Advances in silicon-on-insulator optoelectronics," *Selected Topics in IEEE Quantum Electronics*, Vol. 4, No. 6, pp. 938-947, Nov./Dec. 1998.
- [29] K. S. Yee, "Numerical Solution of Initial Boundary Value Problems Involving Maxwell's Equations in Isotropic Media," *IEEE Transactions on Antennas and Propagation*, Vol. AP-14, No. 3, pp. 302-307, May 1996.
- [30] OptiFDTD User's Reference Version 4.9, Optiwave Inc..
- [31] M. Ohtsu, K. Kobayashi, T. Kawazoe, S. Sangu and T. Yatsui, "Nanophotonics: Design, fabrication and operation of nanometric devices using optical near fields," *IEEE Journal of Selected Topics in Quantum Electronics*, Vol. 8, No. 4, pp. 839-862, July/August 2002.

- [32] K. Hirota, T. D. Milster, Y. Zhang and J. K. Erwin, "Design of a Near-Field Probe for Optical Recording Using 3-Dimensional Finite Difference Time Domain Method," *Jpn. J. Appl. Phys.* Vol. 39, Part 1, No. 2B, pp. 973-975, Feb. 2000.
- [33] M. B. Lee, T. Yatsui, T. Kouroggi, M. Tsutsui, K. Atoda, N. Ohtsu, M, "Fabrication of Si planar apertured array for high speed near-field optical storage and readout," *Lasers and Electro-Optics, 1997. CLEO/Pacific Rim, Pacific Rim Conference*, pp. 14-18 July 1997.
- [34] M. B. Lee, "Near-Field Optical Recording Using a Micromachined Silicon Aperture Probe," *Jpn. J. Appl. Phys.* Vol. 43, No. 9A/B, pp. L1156-L1158, 2004.
- [35] T. Mizuno, T. Kitoh, M. Itoh, T. Saida, T. Shibata, and Y. Hibino, "Optical Spotsizer Converter Using Narrow Laterally Tapered Waveguide for Planar Lightwave Circuits," *IEEE Journal of Lightwave Tech.*, Vol. 22, No. 3, pp. 833-839, March 2004.
- [36] R. A. Soref, E. Cortesi, F. Namavar, and L. Friedman, "Vertically integrated silicon-on-insulator waveguides," *IEEE Photonics Tech. Letters*, Vol. 3, No. 1, pp.22-24, Jan. 1991.
- [37] K. Yamada, T. Tsuchizawa, T. Watanabe, J. Takahashi, E. Tamechika, M. Takahashi, S. Uchiyama, H. Fukuda, T. Shoji, S. Itabashi, and H. Morita, "Microphotonic Devices Based on Silicon Wire Waveguiding System," *IEICE Trans. Electro.*, Vol. E87-C, No. 3, pp. 351-358, March 2004.
- [38] G. Ronald Hadley, "Design of tapered wave guides for improved output coupling," *IEEE Photonics Tech. Letters*, Vol. 5, No. 9, pp. 1068-1070, Sept. 1993.

- [39] H. Takahashi, K. Okamoto, and Y. Homeric, "Integrated-optic 1×128 power splitter with multifunnel waveguide," *IEEE Photonics Tech. Letters*, Vol. 5, No. 1, pp. 58-60, Jan. 1993.
- [40] M. Born and E. Wolf, *Principles of Optics*. 7th edition, Cambridge University Press, 1999
- [41] D. Marcuse, *Light Transmission Optics*. Van Nostrand Reinhold, 1982.
- [42] Tom D. Milster, "New way to describe diffraction from optical disks," *Applied Optics*, Vol. 37, No. 29, pp. 6878-6883, Oct. 1998.
- [43] S. J. Orfanidis, *Electromagnetic Waves & Antennas*. Available at: www.ece.rutgers.edu/~orfanidi/ewa
- [44] K. Lizuka, *Engineering Optics*. Springer-Verlag, 1985.
- [45] C. A. Balanis, *Antenna Theory Analysis and Design*. 3rd edition, Wiley Inc., 2005.
- [46] T. E. Renkoski, *Study of a High Frequency Electro-Optic Beam Deflector Utilizing Reflection-Based Velocity Matching*. Master Thesis, University of Missouri-Columbia, July 2004.
- [47] R. Zhang, P. Catrysse and S. Dods, "Finite-difference-time-domain method guides optical design of metallic nanostructures," available at: www.optiwave.com
- [48] H. Wang and T. S. Rappaport, "A parametric formulation of the UTD diffraction coefficient for real-time propagation prediction modeling," *IEEE Antenna and Wireless Propagation Letters*, Vol.4, pp. 253-257, 2005.
- [49] L. Solomon, F. Grillot, A. V. Zayates, and F. Fornel, "Near-Field Distribution of Optical Transmission of Periodic Subwavelength Holes in a Metal Film," *Physical Review Letters*, Vol. 86, No. 6, pp. 1110-1113, Feb. 2001.

- [50] C. Adam, J. Hass, and A. Thompson, *How to Ace Calculus: The Streetwise Guide*. W. H. Freeman, July 1998.
- [51] H. F. Ghaemi, T. Thio, D. E. Grupp, T. W. Ebbesen, and H. J. Lezec, "Surface Plasmons Enhance Optical Transmission Through Subwavelength Holes," *Physical Review B*, Vol. 58, No. 11, pp. 6779-6782, Sept. 1998.
- [52] J. Hashizume and F. Koyama, "Plasmon-Enhanced of Optical Near-Field of Metal Nanoaperture Surface-Emitting Laser," *Applied Physics Letters*, Vol. 84, No. 17, pp. 3226-3228, April 2004.

VITA

Wen-Ren Yang was born November 18, 1976, in Taichung, Taiwan. He received the following degrees: the B.E. in Electrical Engineering from National Yun-Lin Polytechnic Institute (currently National Formosa University) in 1996; the B.S. in Electrical Engineering from National Taiwan Institute of Technology (currently National Taiwan University of Science & Technology) in 1998.

After the mandatory service in Taiwan Army during 1998~2000, he attended the University of Missouri-Columbia and received the following degrees: the M.S. in Electrical Engineering from the University of Missouri-Columbia in 2002; the Ph.D. in Electrical Engineering from the University of Missouri-Columbia in 2005.